Magnetic Resonance Imaging as a Non-invasive Tool to Investigate Pulmonary and Renal Fibrosis in Small Rodents

Method and Readout Validation, Animal Model Optimization, and Substance Testing

Inauguraldissertation
zur
Erlangung der Würde eines Doktors der Philosophie
vorgelegt der
Philosophisch-Naturwissenschaftlichen Fakultät
der Universität Basel

von

Christine Egger
aus Aarwangen BE

Basel, 2015

Genehmigt von der Philosophisch-Naturwissenschaftlichen Fakultät
auf Antrag von

Prof. Dr. Joachim Seelig
Prof. Dr. Markus von Kienlin
Dr. Nicolau Beckmann

Basel, den 18.06.2013

Prof. Dr. Jörg Schibler
(Dekan)

Table of Contents

1) List of Abbreviations

2D	Two- dimensional
3D	Three-dimensional
BLM	Bleomycin
BMP-7	Bone morphogenic protein-7
BUD	Budesonide
CCD	Charge-coupled device
CD3	Cluster of differentiation 3
Col1α1	Collagen type I, alpha 1
Col1α2	Collagen type I, alpha 2
Col3α1	Collagen type Ill, alpha 1
CompA	Compound A
COPD	Chronic obstructive pulmonary disease
CT	Cycle threshold
CTGF	Connective tissue growth factor
DCE	Dynamic contrast enhanced
DMSO	Dimethyl sulfoxide
ECM	Extracellular matrix
EGF	Epidermal growth factor
F4/80	EGF-like module containing mucin-like, hormone receptor-like sequence 1
FAP	Fibroblast Activation Protein
FOV	Field of view
GE	Gradient echo
GFR	Glomerular filtration rate
H&E	Hematoxylin and eosin
HA	Hyaluronic acid
HGF	Hepatocyte growth factor
HPLC/MS	High performance liquid chromatography/mass spectrometry
HPRT	Hypoxanthine-guanine phosphoribosyltransferase
HYAL	Hyaluronidase

IBA-1	Ionized calcium-binding adapter molecule 1
IN	Intra-nasal
i.p.	Intra-Peritoneal
IPF	Idiopathic pulmonary fibrosis
IT	Intra-tracheal
i.v.	Intra-venous
LAR	Long acting release
MCP	Monocyte chemotactic protein
MIP	Macrophage inflammatory protein
MMP12	Matrix metalloproteinase 12
MRI	Magnetic resonance imaging
NIRF	Near infra-red fluorescence imaging
OA	Oropharyngeal aspiration
PAS	Periodic acid-Schiff
PBS	Phosphate buffered saline
p.o.	Per os
qRT-PCR	quantitative real-time polymerase chain reaction
RF	Radio frequency
RF	Renal fibrosis
ROI	Region of interest
SD	Sprague Dawley
SE	Spin echo
sem	standard error of the means
SNR	Signal-to-noise ratio
SPIO	Superparamagnetic iron oxide
sstr	Somatostatin receptor
T	Tesla
TE	Echo time
TGF-β	Transforming growth factor- β
TIMP	Tissue inhibitor of metalloproteinases
TR	Repetition time

TWR	Tracer washout rate
U	Units
UIP	Usual interstitial pneumonia
UTE	Ultrashort echo time

2) Abstract

Pulmonary fibrosis, an end result of various types of lung damage including interstitial pneumonia and respiratory bronchiolitis [1-3], is a lethal disease characterized by fibroblast proliferation and extracellular matrix (ECM) remodeling. About 20% of the cases are of unknown cause and are thus termed idiopathic pulmonary fibrosis (IPF). A comparable pathology can be observed in fibrotic kidneys. Chronic kidney diseases, as diabetic nephropathy, hypertensive nephropathy, or chronic glomerulonephritis, lead in most cases to renal fibrosis, a disease characterized by infiltration of inflammatory cells, fibroblast activation, glomerulosclerosis and tubulointerstitial fibrosis (for reviews see [4,5])

The work in this thesis concentrates on the validation of magnetic resonance imaging (MRI) as a non-invasive tool to follow longitudinally anatomical and functional changes related to lung and kidney injury induced in the corresponding small rodent models of fibrosis. Bleomycin, instilled into the lungs of mice or rats has been used to induce pulmonary fibrosis. Intra-venous injection of adriamycin induced nephropathy in rats.

The bleomycin model was optimized introducing the oropharyngeal aspiration route for the antibiotic. Ultrashort echo time MRI was validated for the detection of lung lesions and tissue deposition in the pulmonary fibrosis model in rats and mice, while contrast enhanced gradient-echo MRI was validated to detect nephropathy and macrophage infiltration in the rat adriamycin model of renal fibrosis. In addition, two reference substances regarding the treatment of pulmonary fibrosis were found.

In summary, the studies discussed in this thesis deliver contributions to three pillars of preclinical pharmaceutical research: the availability of appropriate animal models, the availability of readouts or parameters that quantitatively reflect disease evolution in those models, and the availability of reference compounds, known to interfere with the disease development.

3) Introduction

3.1) Pulmonary and renal fibrosis – Overview and animal models

Idiopathic pulmonary fibrosis

In an official statement of the American Thoracic Society idiopathic pulmonary fibrosis (IPF) is defined as a "specific form of chronic, progressive, fibrosing interstitial pneumonia of unknown cause, occurring primarily in older adults, and limited to the lungs" [6]. For diagnosis of IPF the histopathological criteria of usual interstitial pneumonia (UIP) must be present, which include marked fibrosis/architectural distortion, with or without honeycombing in a predominantly subpleural/paraseptal distribution, presence of patchy involvement of lung parenchyma by fibrosis, presence of fibroblast foci, and absence of features against a diagnosis of UIP suggesting an alternate diagnosis (hyaline membranes, organizing pneumonia, granulomas, among others) [6-9]. Incidence and prevalence of IPF have only been studied in a few countries and were around 10 cases per 100'000 [8,10-16]. Whether they are influenced by geographic, ethnic, cultural, or racial factors is unknown.

Pulmonary fibrosis in general, an end result of various types of lung damage including interstitial pneumonia and respiratory bronchiolitis [1-3] or with unknown cause (IPF), is a lethal disease characterized by fibroblast proliferation and extracellular matrix (ECM) remodeling. A patchy alveolar wall fibrosis develops in patients with chronic obstructive pulmonary disease (COPD) whereas in chronic asthmatics, a fibrotic response occurs

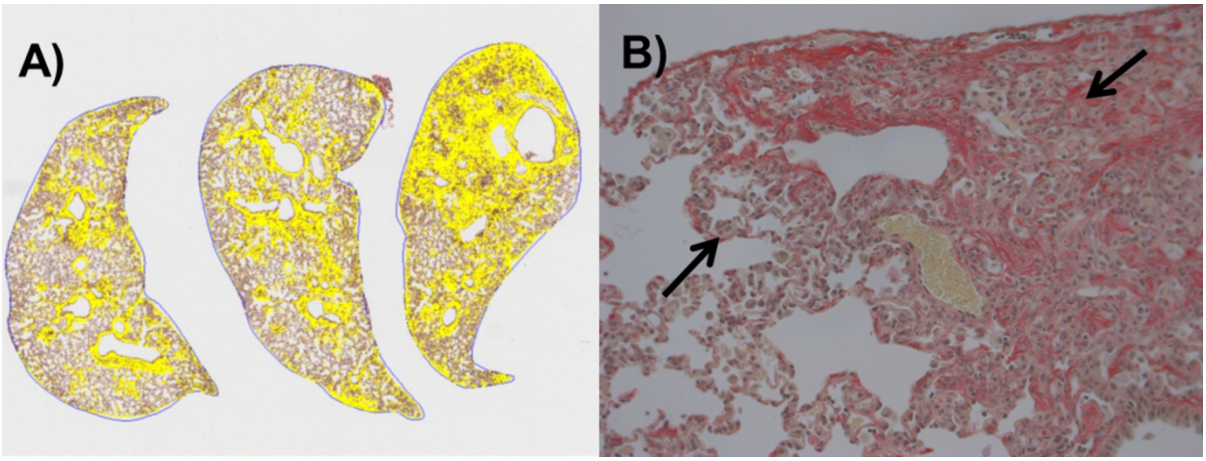

Figure 1: Lung fibrosis in small rodents A) Collagen staining on a left mouse lung lobe. Yellow areas represent collagen. B) Tissue remodeling in a fibrotic rat lung. Arrows point to thickened walls and tissue deposition. Fibrosis was induced by bleomycin.

predominantly in the lamina reticularis, leading to thickening of the basement membrane [17,18]. In both cases the ongoing inflammation-repair cycle leads to permanent structural changes in the airway wall (remodeling) of which fibrosis is a major constituent [19,20]. Up to 50% of the pulmonary fibrosis cases are defined as IPF [21]. Although the pathway of remodeling during the fibrosis development is not yet completely understood, so far it is known that the lung structure is altered by the infiltration of inflammatory cells, thickening of the alveolar walls and deposition of collagen (Figure 1), elastin, and proteoglycans [22-27]. These changes in lung structure lead to an impairment of lung function. Increased lung tissue resistance and elastance, as well as decreased compliance have been shown in humans [2,15] and in small rodent pulmonary fibrosis models [23-25,28-31].

Bleomycin model for pulmonary fibrosis

To date no effective treatment for pulmonary fibrosis is available. For the development of drugs against pulmonary fibrosis, the pharmaceutical research is dependent on animal models which are representative of the human disease.

Bleomycin is an antibiotic with activity against gram-negative bacteria [32] that possesses chemotherapeutic properties and is highly efficient in some types of carcinomas. In spite of these therapeutic characteristics, bleomycin may produce a dose-dependent pulmonary fibrosis in a significant portion of patients [21]. Therefore, single [33-35] or multiple [36] instillation of bleomycin is commonly used to induce experimental pulmonary fibrosis in small rodents. The intra-tracheal (IT) route of administration has been used to deliver bleomycin into the lungs of rats and mice [27,36-38]. Additionally, the intra-nasal (IN) route has also been adopted in mice. Application of the antibiotic causes an acute inflammatory reaction and fibrotic changes that resemble human fibrotic lung disease both histologically and physiologically [22,39]. The availability of this animal model of pulmonary fibrosis provides the opportunity to investigate novel pharmacological approaches aiming to treat this crippling disease.

Renal Fibrosis

Chronic kidney diseases, as diabetic nephropathy, hypertensive nephropathy, or chronic glomerulonephritis, lead in most cases to renal fibrosis, a disease characterized by infiltration of inflammatory cells, fibroblast activation, glomerulosclerosis and tubulointerstitial fibrosis (Figure 2; for reviews see [4,5]). The pathology of renal fibrosis shows several parallels to pulmonary fibrosis. In both cases deposition of ECM proteins leads to scarring of the organ, destruction of parenchyma, and a loss of organ function. The end-result of renal fibrosis is in most cases organ failure, which requires dialysis or organ transplantation [4,5]. A treatment against renal fibrosis is of high interest, but the development of anti-fibrotic drugs, as against renal fibrosis, is challenging. In the past years, research focused a.o. on targeting transforming growth factor- β (TGF-β), hepatocyte growth factor (HGF), and bone morphogenic protein-7 (BMF-7) [40-44], but to date no drug against renal fibrosis is available. The lack of treatment and the limitation of diagnosis to biopsies (as for pulmonary fibrosis) mean heavy burden for the patients. As mentioned before, pharmaceutical research is dependent on animal models and *in vivo* readouts. In this work, the adriamycin model in rats has been used.

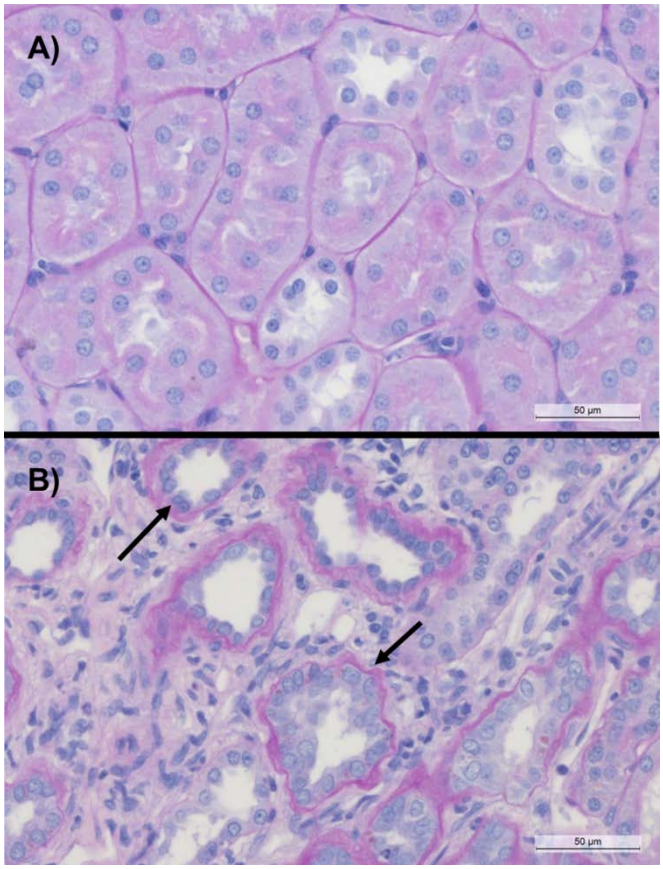

Figure 2: Periodic acid-Schiff (PAS) staining of renal sections at 400x magnification. A) Healthy kidney without abnormalities. B) Arrows point to sclerotic tubuli in a fibrotic kidney. Renal fibrosis was induced by i.v. injection of adriamycin.

Adriamycin induced nephropathy

Adriamycin (doxorubicin, Pfizer) is licensed for the treatment of different cancers, such as breast, lung, and ovarian cancer. The medication works by binding to DNA in cells, altering the shape of the DNA and killing the cells. While adriamycin can kill healthy and cancerous cells, it has a greater effect on cancerous cells because they multiply more rapidly. Adriamycin is a well-

known inducer of renal injury in rodents, which mirrors that seen in human chronic kidney disease due to primary focal segmental glomerulosclerosis [45-47]. Adriamycin-induced nephropathy has enabled a greater understanding of the processes underlying the progression of chronic proteinuric renal disease [48,49]. The model is characterized by podocyte injury followed by glomerulosclerosis, tubulointerstitial inflammation and fibrosis (Figure 2).

3.2) Magnetic Resonance Imaging – Basic Principles and Sequences

Magnetic Resonance Imaging (MRI) is a technique, mainly developed between 1970 and 1980 by Paul Lauterbur and Peter Mansfield, which is able to visualize *in vivo* atomic nuclei, after their magnetization and induction of precession by radio frequency (RF) pulses, due to their differences in relaxation after the RF pulse.

Basic Principles

When a sample is placed in a constant magnetic field [for this work either a 4.7 or a 7.0 Tesla (T) Biospec spectrometer (Bruker Medical Systems, Ettlingen, Germany) has been used], some of the atomic nuclei (mainly protons) owning a magnetic moment (due to spin) align with the magnetic field (Figure 3). This is the equilibrium situation. When an RF pulse is applied at the Larmor

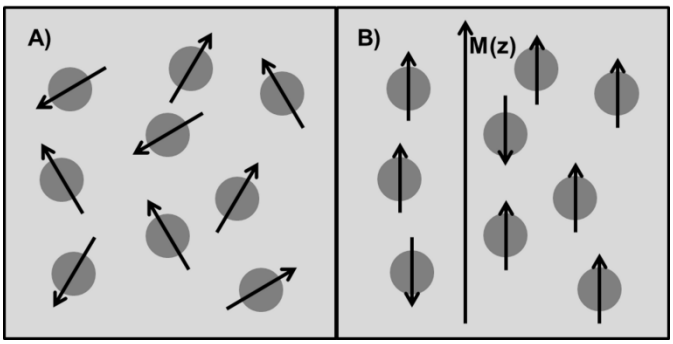

Figure 3: Schematic view of natural orientation of protons/spins (A) and their alignment with a magnetic field M(Z) in z-direction (B).

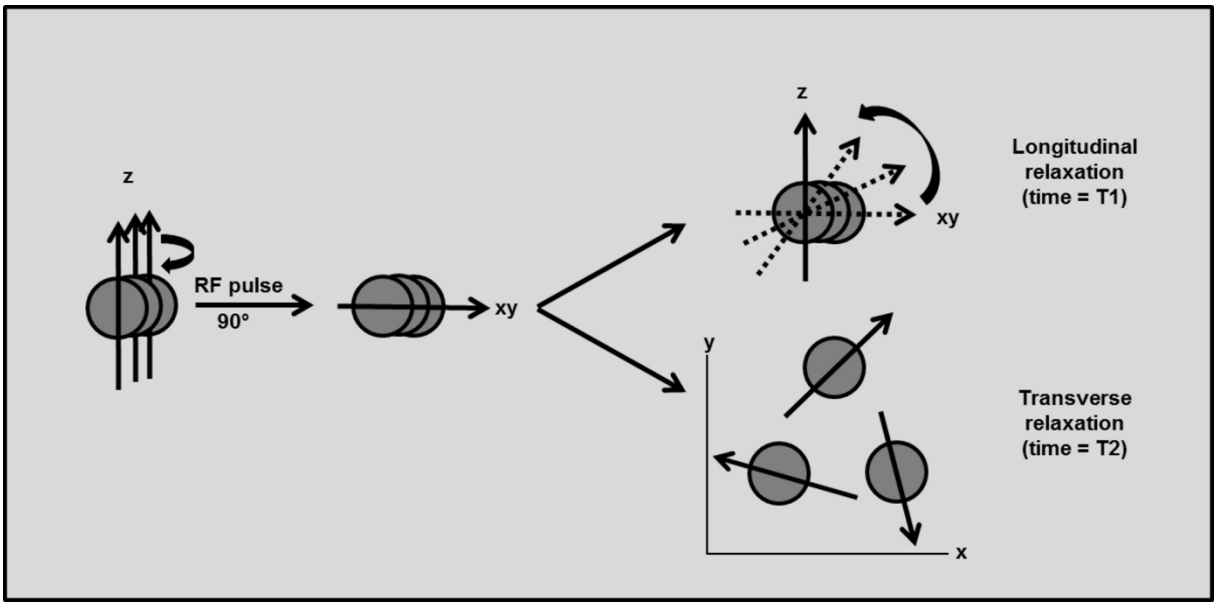

Figure 4: Schematic view of the induction of precession by a 90° RF pulse followed by the longitudinal and transverse spin relaxation. The time needed for longitudinal and transverse relaxation is called T1 and T2, respectively.

frequency during approximately 1 ms or a fraction thereof, nuclei absorb the energy from the RF and are driven out of the equilibrium. They try to recover the alignment with the static magnetic field after the pulse has ended. The RF pulse can be applied with any angle and the following relaxation of the spin is dependent on its interaction with other spins (spin-spin relaxation characterized by the transverse relaxation time, T2) and its environment (spin-lattice relaxation characterized by the longitudinal relaxation time, T1) (Figure 4). A certain time after the RF pulse (Echo time, TE), the radio frequency signal of the spins, induced by their precession, is detected by a receiver coil. In the simplest MR experiment, only one RF pulse is applied. If the experiment is repeated, for instance in order to improve the signal-to-noise ratio (SNR) of the acquisition, then the interval between the RF pulses is called repetition time (TR).

Since the Larmor frequency of a spin is directly proportional to the local magnetic field, B_0, spatial information can be obtained by superimposing a gradient magnetic field onto the static magnetic field during data acquisition (only during a few ms). When a gradient is applied, then the resonance frequencies of the nuclei vary linearly along the direction of the applied gradient. By applying a gradient e.g. along the z direction simultaneously with a frequency selective RF pulse, a slice can be selected perpendicularly to the z direction. Spatial codification of the signals from the spins on the slice is then obtained by applying successively gradients that are perpendicular to each other and also to the slice gradient, e.g. along the x and y directions. These are called respectively the phase encoding and the readout gradients.

With changing parameters as TE, TR, or flip angle of the RF pulse, the influence of tissues' T1 and T2 on the contrast of the acquired image may be shifted. With a rather short TR and TE, so called T1-weighed images are acquired, since only tissues with short T1 achieve longitudinal relaxation and deliver a strong signal with the next excitation. Using a long TE and TR, tissues with short T2 achieve transversal relaxation and lose their signal, while tissue with long T2 appear bright on the image, which is called T2-weighted. If a long TR and short TE is chosen, the contrast is not built by differences in T1 or T2 but only by the amount of spins that deliver a signal and the image is proton-weighted. Due to constant inhomogeneity of the magnetic field, as for instance induced by tissue-air-interfaces, T2 of the involved tissues can be further reduced and is then called T2*. A good example for a tissue with T2*-effect is the lung -one of the organs in focus in the present thesis - where the interface between air and alveolar tissue

causes a very short T2*[50], which poses challenges when imaging the lung tissue (parenchyma).

Spin echo sequence

A 90° slice selective RF pulse is used for spin echo (SE) sequences, after which spins are dephasing with T2*. After half of TE, a second pulse with 180° is applied, let the spins switch their order and rephase after another half TE (Figure 5), which induces an echo. The advantage of this sequence is the elimination of T2*-effects due to the 180°-pulse, which enables the acquisition of T2-weighed images. The weak point is the long acquisition time, caused by the time-consuming second pulse, which makes the sequence susceptible to motion induced artifacts. This is particularly the case in the chest and abdominal region, since breathing of the animal may cause strong movement artifacts. Other approaches like gradient-echo and ultrashort TE (UTE) sequences are more useful for lung imaging.

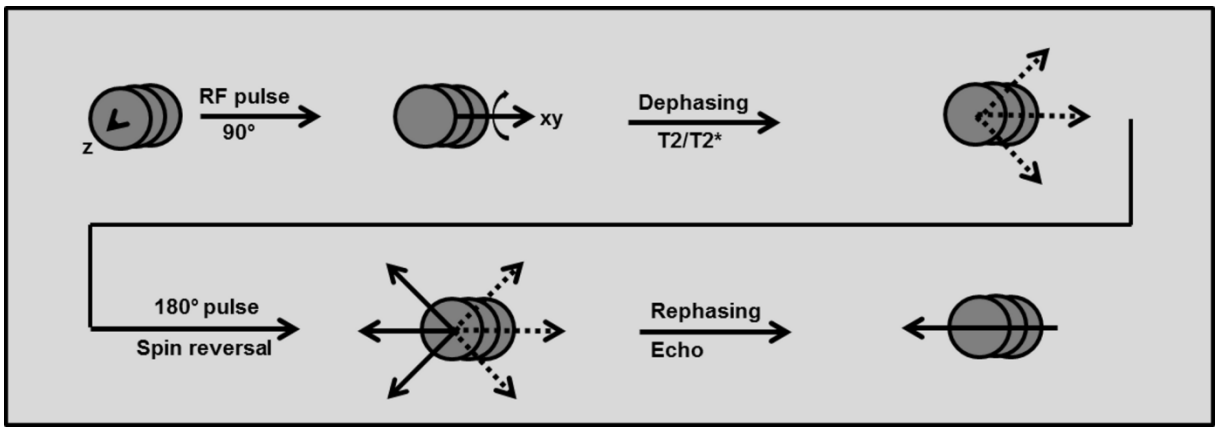

Figure 5: Schematic view of echo induction of a spin echo sequence: A second 180° RF pulse causes rephasing of the spins.

Ultra short echo time (UTE)

In 1991 Bergin et al. described a sequence for the detection of lung parenchyma, aimed to reduce inconsistencies caused by motion of the scanned body [51-54]. The described projection reconstruction method enabled TE of less than 300 μs and visualization of lung parenchyma in spite of its very short T2*[51,52]. Such two-dimensional (2D) ultrashort echo time (UTE) sequences have been used for most of the studies described below and performed

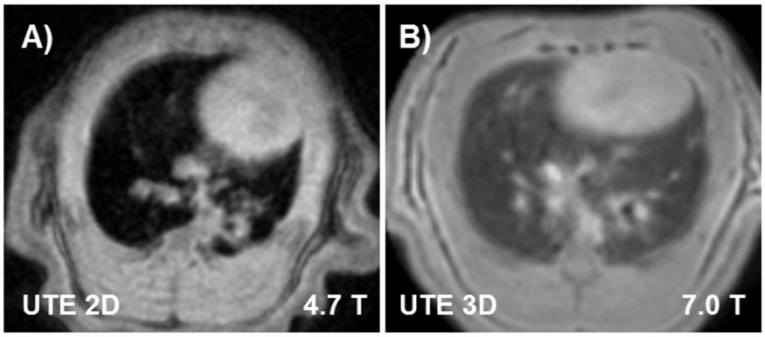

Figure 6: 2D and 3D UTE-MRI at 4.7 T and 7.0 T, respectively. Three-dimensional acquisition facilitates imaging of lung parenchyma.

at 4.7 T (Figure 6A). With TE's of the order of 600 µs signals induced by bleomycin could be readily detected and quantified. When moving to 7 T, because of even shorter T2* values, we realized that shorter TE's would be necessary in order to be able to detect signals in the lung. Three-dimensional (3D) UTE sequences, where another phase-encoding gradient in z-direction was applied to detect signal of the whole field of view (FOV), increased the detectable signal at 7.0 T, as TE's of the order of 20 µs were feasible (Figure 6B).

Gradient echo sequence

Compared to SE sequences, no 180° pulse is needed to induce an echo for signal detection in gradient echo (GE) sequences. After excitation by the RF pulse and slice and phase encoding, follows the frequency-encoding process in two steps: the frequency-encoding gradient (x) is applied first with negative polarity to induce dephasing and again with positive polarity to induce rephasing and consequently an echo (Figure 7). In this case, one speaks of gradient-recalled echo formation. Compared to spin-echo, much shorter TR's are possible and the

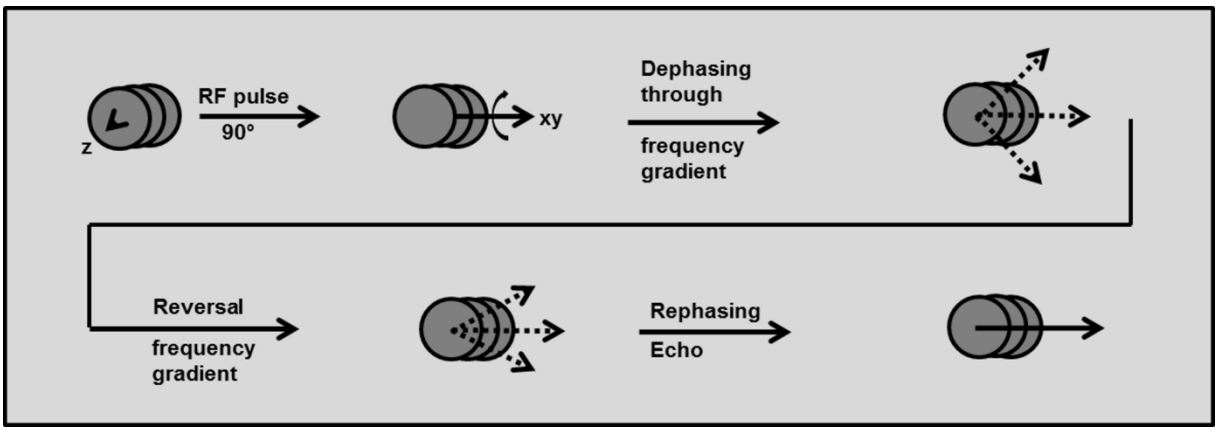

Figure 7: Gradient echo: Dephasing and Rephasing are induced by a frequency gradient with negative and positive polarity, respectively.

acquisition time can be reduced. Thus, GE sequences are less influenced by motion artifacts and are the sequence of choice when short acquisition times are needed. There are a few examples discussed in this work, where short acquisition times were needed and GE sequences have been applied. An imaging session with respiratory-triggered UTE MRI could last for more than an hour and would not allow an acceptable throughput and perfusion measurements of the kidney require the acquisition of images with a sub-second time resolution. For both cases GE sequences have been applied (For example see Figure 8).

Contrast enhancement

In some cases, especially for functional studies, the natural contrast of tissues and fluids is not sufficient and has to be enhanced by so called contrast agents. For instance, the investigation of kidney perfusion and renal clearance, discussed in Chapter 6.1 ("Adriamycin-Induced Nephropathy in Rats: Functional and Cellular Effects Characterized by MRI") of this work, was

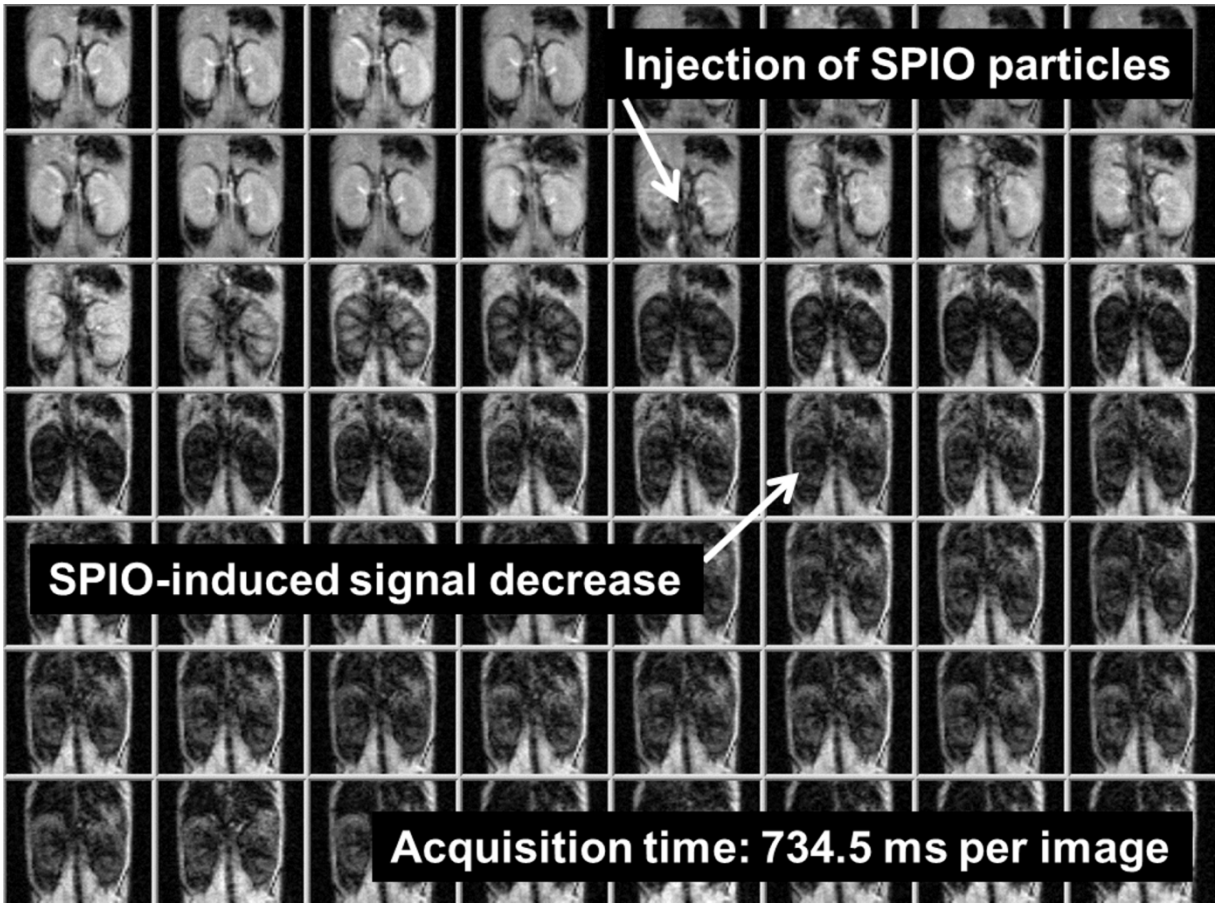

Figure 8: GE-MRI : Signal decrease in blood vessels and kidney induced by SPIO particles. GE sequence allows a short acquisition time. Perfusion information can be derived from the relative signal change induced by the first passage of SPIO through the vascular system of the kidney.

possible due to the use of Endorem and Dotarem, respectively. The intravascular contrast agent, Endorem, contains superparamagnetic iron oxide (SPIO) nanoparticles with superparamagnetic properties that change the local magnetic field and thus impacts T1/T2*. A decrease of MRI-signal induced by SPIO particles to investigate kidney perfusion in mice is shown in Figure 8. The extravascular extracellular contrast agent, Dotarem (gadoteric acid, Gd-DOTA), has paramagnetic properties and decreases the T1 of protons.

3.3) MRI in pharmaceutical research

Use of MRI in preclinical research

Drug design and development is a time and resource consuming process. To reduce time effort and costs, substances and their *in vivo* effects have to be characterized as early as possible. MRI with its noninvasive character and its high spatial resolution offers the opportunity to gain anatomical and physiological information *in vivo*, which makes it an important tool for pharmaceutical research. Already during the early target identification and validation phase (Figure 9) MRI can for instance be used to identify the phenotype of genetically modified mice [55-58]. In later preclinical phases, during *in vivo* pharmacodynamic and safety studies in animal models, MRI delivers important information on anatomical or physiological changes induced by compound treatment [59]. In these phases, especially for animal model testing, MRI is most often used [57].

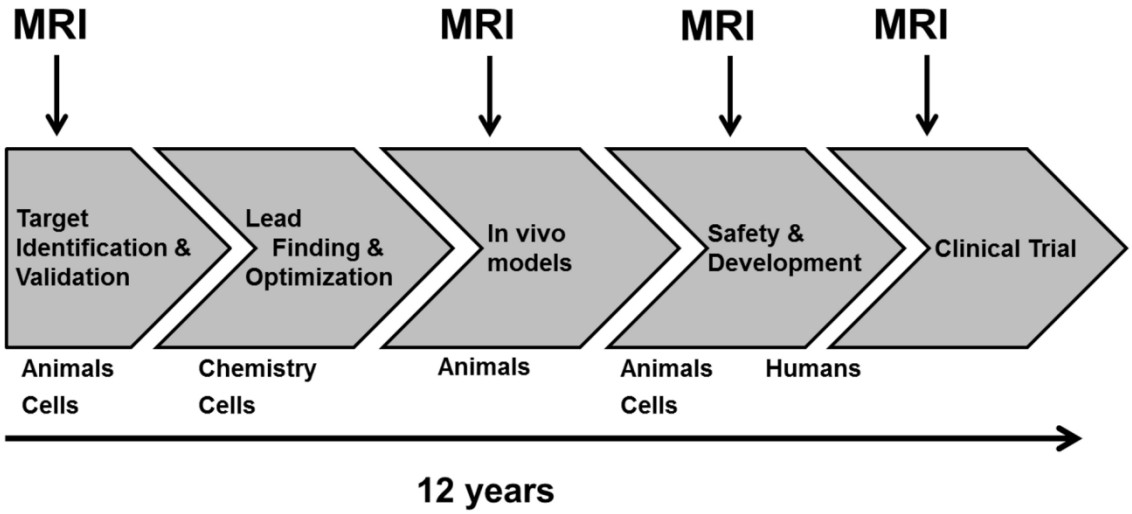

Figure 9: Schematic view of the drug development process. MRI plays an important role in four out of five steps of drug discovery: Phenotyping of genetically modified mice during target identification and validation, substance testing in animal disease models, monitoring of side effects during the safety and development phase, as well as during clinical trials in humans.

MRI and 3R

In 1959 Russel and Burch introduced the 3R concept (Reduction, Refinement and Replacement) regarding humane treatment of laboratory animals [60]. The goal of scientists should be to minimize the number of animals (Reduction) in experiments, to reduce their suffering and pain (Refinement), and to support the substitution of animals whenever possible (Replacement). MRI turned out to have a high impact on the realization of the 3R-concept.

Reduction

The non-invasive character of MRI allows time course studies and delivers information for several time points with a lower number of animals than needed in terminal readouts. Since each animal can be used as its own control for MRI analyzes, either the statistical significance can be increased or less animals have to be used to reach certain significance. Further, imaging may facilitate go/no-go-decisions during drug development [57,61] and therewith avoid further unnecessary studies.

Refinement

Imaging enables a non-invasive recording of morphological and functional data which means a strong refinement, compared to invasive readouts as for instance biopsies. Since MRI allows monitoring a disease model over time, it facilitates the definition of a humane study termination date and reasonable study-abortion criteria, which prevents the animals from unnecessary pain and suffering. As mentioned before, MRI may increase the statistical significance of a study. Therefore, an animal model with a mild disease-course can often be chosen.

Replacement

The use of Imaging in clinical trials supports early go/no-go decisions in phase I/II [57,62,63]. The optimization of the clinical phase may replace an animal experiment, which is at least indirectly supported by imaging techniques as MRI.

3.4) Thesis outline

Three components are of fundamental importance in the context of preclinical pharmacological research *in vivo* aiming to develop new therapies (Figure 10): *(i)* the availability of appropriate animal models; *(ii)* the availability of readouts or parameters that quantitatively reflect disease evolution in those models; and *(iii)* the availability of reference compounds, known to interfere with the disease development. Preclinical research in the context of fibrosis is particularly challenging due to the lack of reference substances. Moreover, being a chronic condition, the search for therapies would highly benefit from the availability of non-invasive readouts.

The work in this thesis concentrates on the validation of MRI as a non-invasive tool to follow longitudinally anatomical and functional changes related to lung and kidney injury induced in the corresponding small rodent models of fibrosis. Repetitive measurements open new avenues in testing compounds as the responses at several time points during the course of injury development and treatment can be compared. Specifically, studies at the chronic phase, when fibrosis is already established, become amenable. In an iterative process, it is shown how imaging can contribute to further optimization and refinement of the animal models. The studies presented in this thesis thus focus on three pillars: Method and readout validation, animal model optimization, and substance testing.

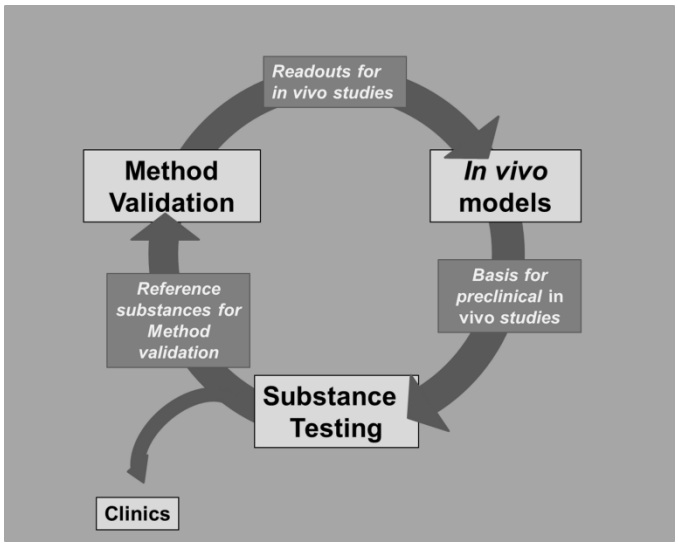

Figure 10: Schematic view of important components for pharmaceutical research and drug development in preclinical phase (*in vivo*).

4) MRI as a readout for pulmonary fibrosis in mice and rats

Manuscript (Published):

4.1) "Administration of Bleomycin via the Oropharyngeal Aspiration Route Leads to Sustained Lung Fibrosis in Mice and Rats as Quantified by UTE-MRI and Histology"

Christine Egger[1,4], Catherine Cannet[1], Christelle Gérard[1], Elizabeth Jarman[2], Gabor Jarai[2], Agnès Feige[3], Thomas Suply[3], Arthur Micard[1], Andrew Dunbar[1], Bruno Tigani[1], Nicolau Beckmann[1,#]

Novartis Institutes for BioMedical Research, [1]Global Imaging Group, CH-4056 Basel, Switzerland, [2]Respiratory Diseases Department, Horsham RH12 5A, UK, [3]Developmental and Molecular Pathways Department, CH-4056 Basel, Switzerland; and [4]University of Basel, Biocenter, CH-4056 Basel, Switzerland.

Introduction

Pulmonary fibrosis, characterized by fibroblast proliferation and extracellular matrix remodeling, is the end result of various types of lung damage including interstitial pneumonia and respiratory bronchiolitis [1-3]. A patchy alveolar wall fibrosis develops in patients with chronic obstructive pulmonary disease (COPD) whereas in chronic asthmatics, a fibrotic response occurs predominantly in the lamina reticularis, leading to thickening of the basement membrane [17,18]. In both cases the ongoing inflammation-repair cycle leads to permanent structural changes in the airway wall (remodeling) of which fibrosis is a major constituent [19,20]. However, up to 50% of the cases of pulmonary fibrosis are defined as idiopathic pulmonary fibrosis (IPF) [21].

Bleomycin is an antibiotic with activity against gram-negative bacteria [32] that possesses chemotherapeutic properties and is highly efficient in some types of carcinomas. In spite of these therapeutic characteristics, bleomycin may produce a dose-dependent pulmonary fibrosis in a significant portion of patients [21]. Therefore, single [33-35] or multiple [36] instillation of bleomycin is commonly used to induce experimental pulmonary fibrosis in small rodents. Application of the antibiotic causes an acute inflammatory reaction and fibrotic changes that resemble human fibrotic lung disease both histologically and physiologically [22,39]. The availability of this animal model of pulmonary fibrosis provides the opportunity to investigate novel pharmacological approaches aiming to treat this crippling disease.

The intra-tracheal (IT) route of administration has been used to deliver bleomycin into the lungs of rats and mice [27,36-38]. Additionally, the intra-nasal (IN) route has also been adopted in mice. Arguments for favoring the IN administration protocol in this species are the method's simplicity and speed, and that it does not injure the trachea. A major disadvantage of the IN administration route is the inhomogeneous distribution of the liquid in the respiratory tract, which is dependent on different parameters as the volume of instilled fluid and the depth of anesthesia [64].

An alternative technique called oropharyngeal aspiration (OA) has been developed to administer substances into the lungs of mice. One of the first applications of this method can be found in a study by Foster et al., who used OA for the instillation of ^{99m}TC-labelled sulfur colloid to measure mucociliary function in mice by scintigraphy [65]. Rao et al. used the

technique to administer fluorescent amine-modified polystyrene latex beads and beryllium oxide particles into the mouse lung. They found the technique to be simple and reproducible and the exposures of the lung to be highly correlated to the administered doses of substrates [66]. A comparison of IT to OA administration was performed by Lakatos et al. in a mouse model of silicosis [67]. Mice treated with crystalline silica administered via the OA route developed fibrosis with a more homogenous distribution all over the lung and with less variability. The OA method has also been used in other studies as for instance a mouse model of chemical-induced asthma [68] or a murine model of diacetyl toxicity [69].

Recently we reported the use of MRI to non-invasively follow the course of lung injury induced by repeated IN administration of bleomycin to mice [70], or of single or repeated IT bleomycin administration to rats [27]. In the present work this model of lung fibrosis has been further refined by adopting the OA administration route for bleomycin. The responses in the lungs detected *in vivo* by MRI have been compared to histology, hydroxyproline determination and quantitative real-time polymerase chain reaction (qRT-PCR) analyses.

Material and Methods

Ethics Statement

Experiments were carried out with the approval of the Veterinary Authority of the City of Basel (license number BS-1989).

Animals

Seven- to 9-week-old C57BL/6 (n=35) or BALB/c (n=37) male mice or Sprague Dawley (SD) rats (n=10) (Elevage Janvier, Saint Berthevin, France) were used throughout the study. Animals were kept at an ambient temperature of 22 ± 2°C under a 12 h normal phase light-dark cycle and fed NAFAG® pellets (Nahr- und Futtermittel AG, Gossau, Switzerland). Drinking water and food were freely available.

Intra-nasal administration of bleomycin or saline

Mice were lightly anesthetized with 2.0% isoflurane (Abbott, Cham, Switzerland) delivered in a box and bleomycin hydrochloride (Teva, Basel, Switzerland), 0.25 mg/kg in 25 µl of saline (0.9%) or vehicle (25 µl of saline (0.9%)) was administered IN with a micropipette (12.5 µl per nostril). Animals were allowed to recover immediately afterwards. This procedure was performed six times consecutively, once daily. Bleomycin solution was prepared before the first administration and then stored, in aliquots, at 4°C for administration at the further time points. A similar administration protocol has been shown earlier to induce substantial and sustained pulmonary fibrosis in mice [70]. The bleomycin solution kept at 4°C was stable over 6 days as verified by high performance liquid chromatography/mass spectrometry (HPLC/MS) analyses (Figure 11), a result that is consistent with earlier studies demonstrating that bleomycin in solution at room temperature is stable for more than two weeks [71].

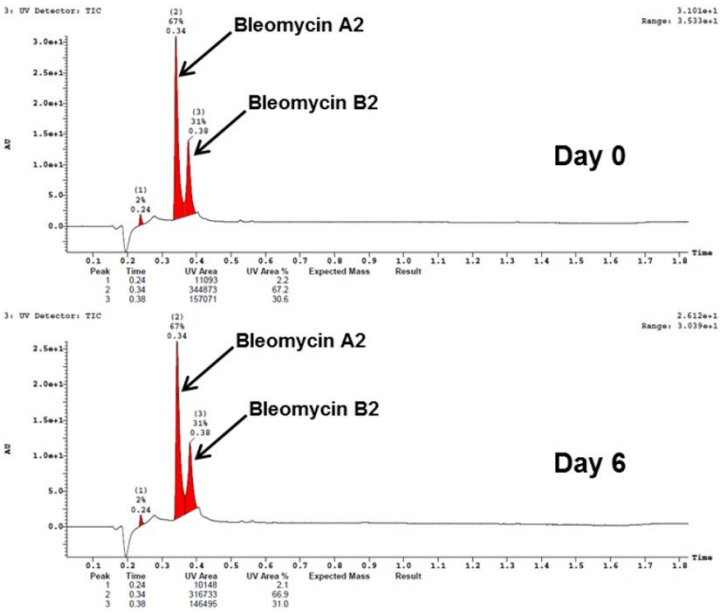

Figure 11: HPLC/MS spectra of bleomycin (0.075mg/mL) freshly prepared and after six days at 4°C acquired on an xxx instrument (xxx). An acquity HSS T3 1.8 µm 2.1x50mm column was used at 60°C; eluent A (water + 0.05% formic acid + 3.75 mM ammonium acetate) and eluent B (acetonitrile + 0.04% formic acid) were used with a gradient of 5 to 98% B in 1.4 min and 1.0 mL/min flow. Bleomycin A2: C55H84N17O21S3+ with a mass of 1415.56 g/mol; bleomycin B2: C55H84N20O21S2 with a mass of 1425.52 g/mol.

Oropharyngeal aspiration of bleomycin or saline in mice

Animals were lightly anesthetized with 2% isoflurane delivered in a box and bleomycin hydrochloride (0.1 or 0.25 mg/kg for C57BL/6 mice; 0.5 or 1 mg/kg for BALB/c mice) in 40 µl of saline (0.9%) or vehicle (40 µl of saline (0.9%)) was administered via OA using a micropipette. OA was performed as described by de Vooght et al. [68]. Mice were fixed on a surgery board, the tongue was pulled out with a forceps, and the liquid was placed onto the

distal part of the oropharynx while the nose was gently closed. As for the IN administration protocol, the procedure was performed six times consecutively, once daily.

Oropharyngeal aspiration of bleomycin in rats

Animals were lightly anesthetized with 3.5% isoflurane delivered in a box and bleomycin hydrochloride, 2mg/kg in 100 µl of saline (0.9%) was administered via OA with a micropipette using a similar procedure as described above for mice.

Magnetic resonance imaging (MRI)

During MRI signal acquisitions, animals were placed in supine position in a cradle made of Plexiglas. Body temperature was kept at 37±1°C using warm air. Following a short period of introduction in a box, anesthesia was maintained with 1.5% isoflurane for mice and 2% for rats in a mixture of O_2/N_2O (1:2), administered via a nose cone. All measurements were performed on spontaneously breathing animals; neither cardiac nor respiratory triggering was applied. As demonstrated earlier [70,72], averaging over several respiratory cycles suppressed artifacts caused by movements of the chest and the heart without the necessity of triggering the data acquisition. Measurements were carried out with a Biospec 47/40 spectrometer (Bruker Medical Systems, Ettlingen, Germany) operating at 4.7 T and equipped with an actively shielded gradient system capable of generating a gradient of 200 mT/m. The operational software of the scanner was Paravision (Bruker).

An ultra-short echo time (UTE) sequence [73-75] with the following parameters was applied for the detection of bleomycin-induced lung injury in mice: repetition time 20.0 ms, echo time 529 µs, 604 projections, 2 averages, band width 200 kHz, flip angle of the excitation pulse 25°, matrix size 192x192, slice thickness 1.4 mm and FOV 3.0 x 3.0 cm^2. The total acquisition time was of 4.0 min for 10 consecutive axial slices covering the entire lung. In an initial assessment, different numbers of averages were tested: 1 average (2-min-acquisition-time), 2 averages (4-min-acquisition-time), 4 averages (8-min-acquisition-time), and 8 averages (16-min-acquisition-time). It was found that the acquisition with 2 averages was appropriate and then used throughout the study. A birdcage resonator of 32 mm diameter was used for excitation and detection. For rats an UTE sequence with the following parameters was used: repetition time 8.0 ms, echo time 528 µs, 604 projections, 5 averages, band width 200 kHz, flip angle of

the excitation pulse 25°, matrix size 192x192, slice thickness 2.0 mm and FOV 6.0 x 6.0 cm^2. The total acquisition time was of 7.25 min for 18 consecutive transverse slices covering the entire lung. A birdcage resonator of 70 mm diameter was used for excitation and detection.

MR image analysis

At a given time point, the area of bleomycin-induced lesions was quantified on each image from the dataset covering the whole lung, using a semi-automatic segmentation procedure implemented in the IDL (Interactive Data Language Research Systems, Boulder, Colorado, USA) environment on a Linux system. Images were first low-pass-filtered with a Gaussian profile filter and then transformed into a set of four grey level classes using adaptive Lloyd-Max histogram quantitation. The highest class in the transformed images was extracted interactively by a region grower, whose border was drawn manually on each slice to control the growing and limit it to areas within the lung (Figure 12). For each image, the area thus segmented by region growing corresponded to high intensity signals in the lung. The total volume of high intensity signals was then calculated by adding the areas obtained for each image from the dataset, and multiplying the summed value by the slice thickness. Segmentation parameters were the same for all analyzed images.

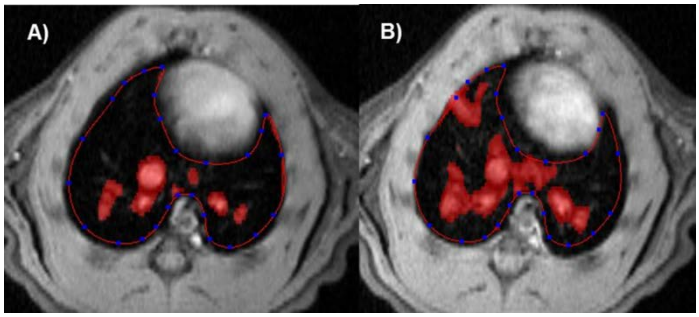

Figure 12: Details of segmentation procedure. For each slice, a border is drawn manually to limit the segmentation of high intensity signals to the lung. Images correspond to a rat at A) baseline and B) day 7 after OA of bleomycin (2 mg/kg).

Post-mortem analyses

Animals were sacrificed with an overdose of thiopental (Pentothal®, Abbott; 250 mg/kg intra-peritoneal (i.p.), 0.2 ml) immediately after an MRI acquisition. The trachea was immediately ligated to avoid collapse of the lung. Following the organ's removal, the left lobe was used for histological analyses, while the right lobes were employed for hydroxyproline and qRT-PCR analyses.

Histology

Histological analysis was performed as described in more detail earlier [72]. Lung lobes were immersed in 10% neutral buffered formalin for 24 h. Following fixation, lungs were trimmed, and three transverse sections approximately 0.8 mm thick were cut through the left lung (superior, median, and caudal parts) to include the main bronchi as well as the pulmonary alveoli. Sections were then dehydrated through increasing graded series of ethylic alcohol and embedded in one block of paraffin wax. Three serial histological slices (3 µm) were obtained from each section and stained with picrosirius red for the identification of collagen fibers and newly synthesized collagen (Figure 13). Although polarized light is useful for the dating of fibrosis [76-82], in this work histological slices have been examined under bright field illumination to detect and quantify collagen. The quantification of collagen in picrosirius stained slices using bright field has been described elsewhere [83-89]. For each animal, a mean value was derived from the analysis of nine histological slices.

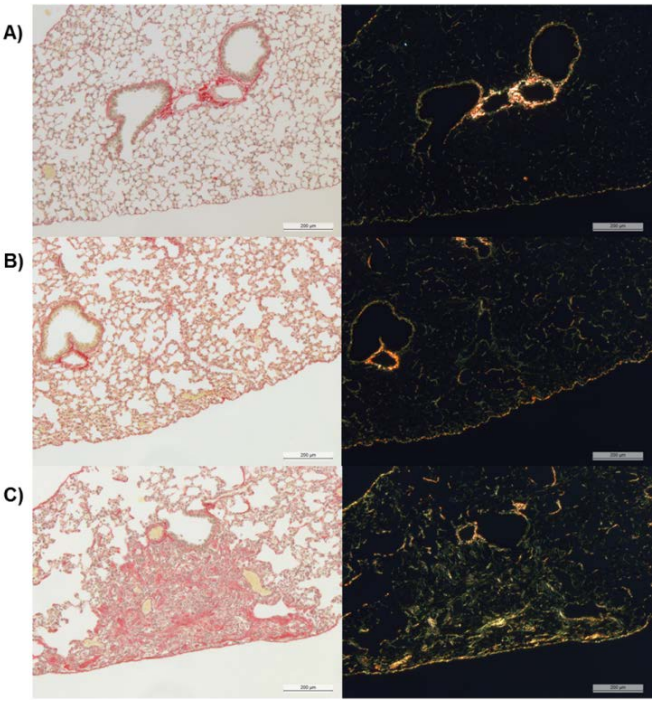

Figure 13: Picrosirius-stained histological slices of C57BL/6 mice observed at bright-field (left column) and at polarization (right column). The high intensity areas in the polarized view, corresponding to collagen, coincide well with the red areas in the bright-field view. In this work, collagen has been quantified by examining histological slices at bright-field. A) Saline-challenged mouse (OA administration). B) IN administration of bleomycin

Collagen was quantified using the program "Histolab" (Microvision Instruments, Evry, France). Picrosirius-stained slides were examined with a light microscope (Eclipse E600, Nikon, Egg, Switzerland) connected to a charge-coupled device (CCD) progressive scan video color camera (XCD-U100 CR, Sony, Tokyo, Japan). The whole surface of three slices of the left lung was captured at x10 magnification. The color corresponding to picrosirius was extracted by threshold setting and the area corresponding to picrosirius staining calculated. The

percentage of picrosirius to the total lung surface analyzed was calculated for each animal. Results were shown as picrosirius factors, expressing the collagen content in the lungs of bleomycin-challenged animals relative to the mean collagen content in the lungs of saline-treated animals.

Determination of hydroxyproline in lung tissue samples

Lung tissue samples were weighed, dried in an oven at 90°C overnight, and the weight was recorded again. Dry tissues were then boiled in 0.5 mL of 6 M HCl at 120°C overnight (8-16 h) in Pyrex tubes with heat- and acid-resistant screw-on caps (article TES-830-70G; Fisher Scientific, Wohlen, Switzerland). After cooling down and adding 5 µL of phenolphthalein (1%), the samples were neutralized with NaOH 10 M (Sigma N°S-5881) and 6 M HCl. Black precipitate and brown color was removed by adding 100 µL of carbon suspension [10 mg/mL activated charcoal (article C4386; Sigma-Aldrich, Buchs, Switzerland) in water], centrifugation, and filtration. Five microliters of standard or hydrolyzed sample were pipetted in triplicate onto a 96 well plate, and 5 µL citrate acetate buffer (5% citric acid, 7.2% sodium acetate, 3.4% sodium hydroxide, 1.2% glacial acetic acid, distilled water) was added to each well, as well as 100 µL of freshly prepared chloramine-T solution (14.1mg chloramine-T, 0.1mL n-propanol, 0.1mL distilled water, 0.8mL citrate acetate buffer). The samples were then incubated at room temperature for 20 minutes. After adding 100 µL of Ehrlich's reagent (2.5 g of 4-(dimethylamino)benzaldehyde, 9.3 mL of n-propanol, and 3.9 mL of 70% perchloric acid), the wells were incubated for 20 minutes at 65°C. After cooling down, the samples were measured at 550 nm on a spectrophotometer (SpectraMax 340PC, Molecular Devices, Sunnyvale, CA, USA) and a standard curve from 5 to 100 mg hydroxyproline in water was created. Data were expressed as µg/right lung lobe.

Quantitative real-time polymerase chain reaction (qRT-PCR)

Removed lung tissue was stabilized in liquid nitrogen and stored at -80°C until use. For RNA purification, samples were transferred to a 2 ml Eppendorf tube with 1000 µl of RLT buffer (Qiagen, Hombrechtikon, Switzerland; #79216) and β-mercaptoethanol (Sigma-Aldrich; #M3148) and one stainless bead (Qiagen, #69989). Samples were homogenized (Qiagen Tissue Lyser, #85300) in two to three 1-min runs at 30 rotations/s each, with 1 min on ice between

the runs. After centrifugation for 3 min at 13 000 rpm, 4°C, 300 µl of the resulting supernatant were processed on the Rneasy Mini Kit (Qiagen, #74106) with a DNAse digestion step (Qiagen, #79254) following the manufacturer's protocol. Resulting total RNAs were quantified on a NanoDrop™ system (NanoDrop Technologies Inc., Wilmington, DE, USA) and 1 µg was reverse-transcribed using the high capacity cDNA RT kit (Applied Biosystems, Zug, Switzerland; #4368813).

Expression of the different genes of interest was evaluated by RT- PCR using the ABI Prism 7900HT system (Applied Biosystems). Briefly, 10 ng/µl equivalent RNA per well was distributed in a 384 well plates (Applied Biosystems, #4326270), with 5 µl of the Taqman Universal Mastermix 2X kit (Applied Biosystems, #4324020) and 0.5 µl of 20X Assay-on-demand mix Taqman probe (Applied Biosystem, #4331182). The probes used were Mm00801666_g1 (Collagen type I, alpha 1; Col1α1), Mm00802529_m1 (epidermal growth factor-like module containing mucin-like, hormone receptor-like sequence 1, F4/80), and Mm00500554_m1 (matrix metalloproteinase 12; MMP12). Expression for each sample was normalized to Hypoxanthine-guanine phosphoribosyltransferase (HPRT, probe Mm03024075 m1) and compared to the vehicle-treated group, using the $2^{-\Delta\Delta CT}$ formula ($2^{-(\Delta CT1 - \Delta CT2)}$), where ΔCT1 is the averaged cycle threshold (CT) value of a sample, normalized to HPRT and ΔCT2 is the average of ΔCT in the control group (vehicle group), also normalized to the housekeeping gene, resulting in the relative fold induction. The expression of HPRT was the same in all analyzed groups.

Near-infrared-fluorescence (NIRF) imaging for distribution analyses

For comparison of the administration routes, in a separate set of experiments isoflurane-anesthetized mice received a solution containing the fluorescent dye Cy5.5 either IN (25 µL; 12.5 µL per nostril) or OA (25 µL). Animals were allowed to recover from anesthesia immediately after solution administration. However, they were sacrificed 60 min later with an overdose of thiopental (250 mg/kg i.p, 0.2 mL). The trachea was immediately ligated to avoid collapse of the lungs, which were harvested from the body. NIRF imaging was performed on the isolated lungs using a Photon Imager (Biospace Lab, Paris, France). For fluorescence excitation, a Xenon lamp at 660 nm was used. The fluorescent light emitted from the sample was detected by a charge-coupled device camera, equipped with a focusing lens system. The

matrix size of the images was 532 x 532 pixels. A hard filter was used for detection wavelength selection (700 nm).

Statistics

For statistical analysis the software SigmaPlot™ (Systat Software Inc., San Jose, CA, USA) has been used. One-way ANOVA and Bonferroni tests have been performed for endpoint readouts while one- or two-way repeated measures ANOVA with Bonferroni tests have been used for readouts with multiple measurements. The following abbreviations were used for the indication of significance: */#: 0.01<p<0.05; **/##: 0.001≤ p ≤ 0.01 ***/ ###: p< 0.001.

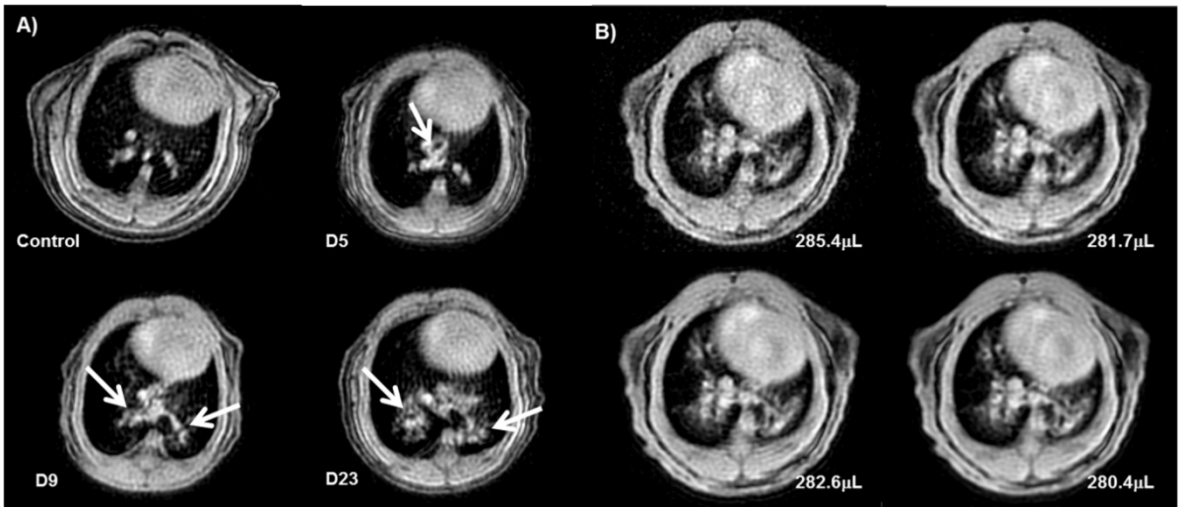

Figure 14: Detection of bleomycin-induced lung injury by UTE-MRI in BALB/c mice. A) Measurements (4-min-acquisition-time) on comparable slices before and at different time points (5, 9, and 23 days) after OA of 6 x 1.0 mg/kg bleomycin. Arrows point to bleomycin-induced lung injury. B) Comparison of UTE acquisitions with different numbers of averages in a bleomycin-treated animal. The volumes of signals in the lungs evaluated from these images were comparable for all acquisition conditions: 1 average (285.4 µL), 2 averages (281.7 µL), 4 averages (282.6 µL), 8 averages (280.4 µL). White arrows point to bleomycin induced lung injury.

Results

Detection of bleomycin-induced lung injury in mice by optimized UTE-MRI with short acquisition time

Due to a reduction of the echo time and a decrease in the number of averages, the acquisition time for MRI of mice lungs could be strongly shortened as compared to previous work [70,72]. Only four minutes were needed to generate images covering the whole lung of a mouse with ten slices, each averaged out of 2 single acquisitions (Figure 14A). The optimized acquisition was compared to longer acquisitions comprising 4 or 8 averages and resulting in data collection times of 8 and 16 minutes, respectively. Since the amount of

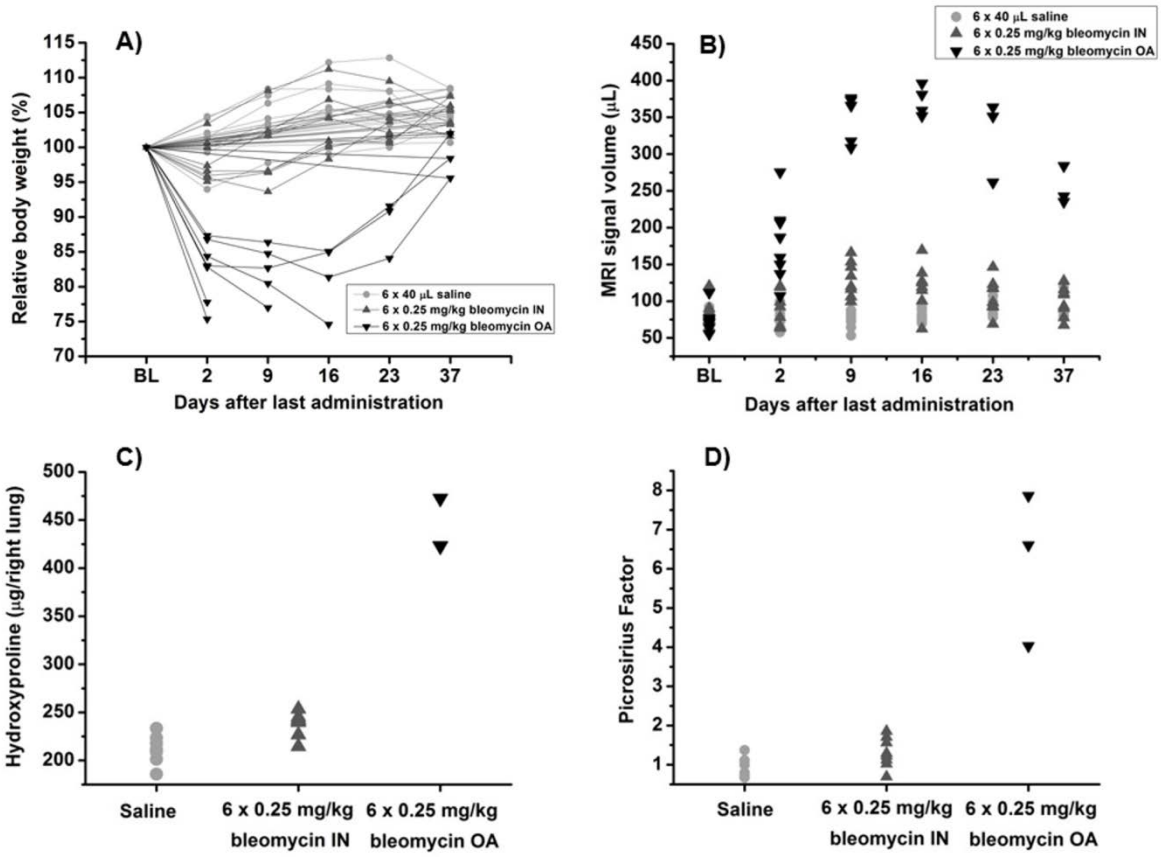

Figure 15: Comparison of OA to IN administration of bleomycin (6x0.25 mg/kg) in C57BL/6 mice (n=8 per group) by *in vivo* MRI and *post-mortem* analyses. All data are shown as means ± STDEV. A) Relative body weight and time point of death during the study. Animals have been sacrificed directly after their last measurements. Five out of eight mice receiving OA of bleomycin had to be sacrificed prematurely due to excessive bodyweight loss (A). B) Total volume of MRI signals in the lung (µL). The signal at baseline contains contributions from vessels, whereas signals following bleomycin reflect additionally the injury inflicted by the antibiotic. C*) Post-mortem* determination of hydroxyproline in right lung lobes (day 37). D) Amount of collagen detected by histology of picrosirius in left lung lobes (day 37). Results are expressed as collagen content relative to mean collagen content in the lungs of saline-treated mice (picrosirius factor).

detected lung signal, in healthy as well as in bleomycin-treated animals, was similar for all tested protocols (Figure 14B), the shorter acquisition, allowing a higher throughput and a strong reduction of narcosis time, was preferred.

OA of bleomycin led to increased induction of lung fibrosis in C57BL/6 mice compared to IN administration

The volume of signals induced by repeated IN bleomycin dosing (6x0.25 mg/kg) as described in Babin et al. [25] and detected by MRI never exceeded 120 µL, for different experimenters and studies performed in C57BL/6 mice. The maximum initial weight loss was of 15%. When the dose of bleomycin was doubled, namely to 6x0.5 mg/kg IN, a higher response was obtained (approximately 150 µL), but 40% of the animals had to be sacrificed prematurely due to weight loss in excess of 20%. Taken together, these preliminary data suggested that 6x0.25 mg/kg would be the best compromise for routine studies involving IN dosing of bleomycin, since fibrotic responses would be induced with low initial weight loss as shown earlier [25]. The main drawback of the IN dosing was that fibrotic lesions, despite being elicited in different

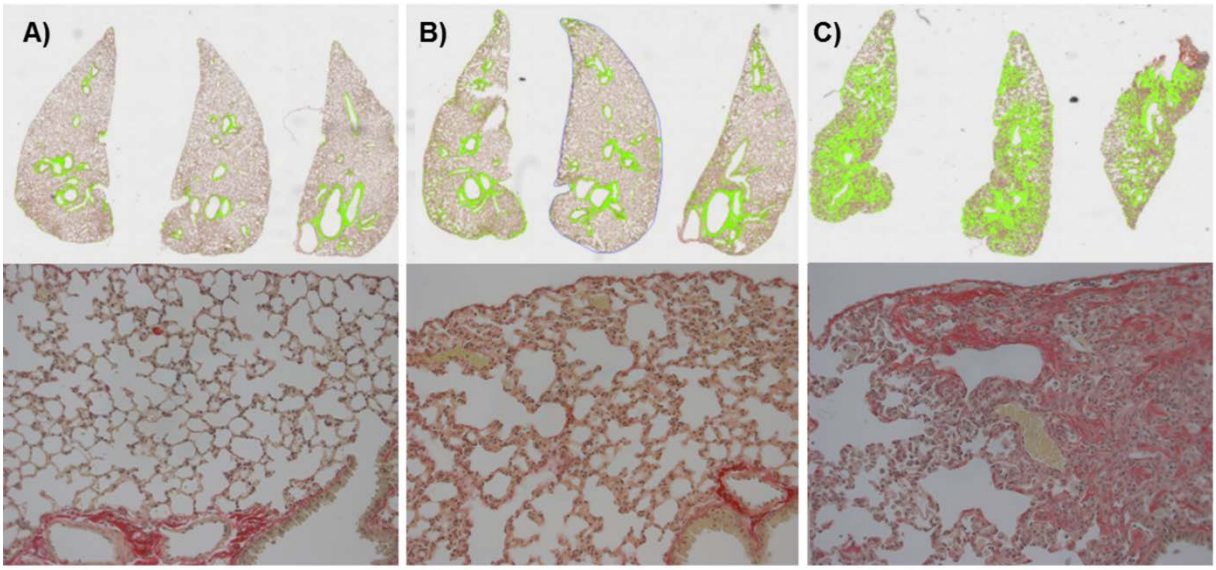

Figure 16: Histology of picrosirius stained lung slices from C57BL/6 mice. Collagen (green) visualized by picrosirius staining in three slices of the left lung lobe (upper row). Magnified views (x200) of a portion of the corresponding histological slices are shown in the bottom row. A) Stained collagen content in saline treated mouse lung 37 days after administration. B) Stained collagen content in a mouse lung 37 days after last IN bleomycin administration (0.25 mg/kg on six consecutive days). C) Collagen content in a mouse lung 37 days after last OA of bleomycin (0.25 mg/kg on six consecutive days). Compared to the IN administration, the amount of picrosirius was six times higher when bleomycin was oropharyngeally aspirated and the distribution of picrosirus staining was more homogeneous.

lung lobes, appeared predominantly around the largest superior airways [25]. We thus aimed at verifying whether another route, namely OA, might lead to a more homogeneous distribution of fibrotic lesions throughout the lungs. As a first step, the same dose of bleomycin optimized for the IN studies, namely 6x0.25 mg/kg, has been used.

C57BL/6 mice were treated on six consecutive days with saline or bleomycin (0.25 mg/kg) by either the IN or OA route. Whereas mice dosed with bleomycin IN had initial weight loss within 10% of the body weight, five out of eight animals that received bleomycin OA had to be sacrificed prematurely because of excessive weight loss (≥ 20% of the initial body weight) (Figure 15A). MRI baseline measurements before the first administration of bleomycin allowed the use of each animal as its own control. Further MRI measurements were performed on several time points after last bleomycin administration. The course of MRI-detected lung injury is shown in Figure 15B. Compared to the IN route, OA administration of bleomycin led to significantly higher responses in the lungs as evidenced by MRI from a very early (day 2 after last bleomycin administration) to a late time point (day 37 after last bleomycin administration) (Figure 15B). These findings were confirmed by *post-mortem* analysis of the lungs (37 days after last bleomycin administration). Determination of hydroxyproline in the right lung lobe (Figure 15C) showed a significantly higher amount of hydroxyproline in lungs from mice that had received bleomycin via the OA than the IN route or the control group (Saline). The amount of hydroxyproline in the lungs of IN-treated mice differed only slightly from the saline group. The amount of collagen in the left lung lobe was quantified by picrosirius staining in histological samples. The amount of collagen in the lungs of mice that had received bleomycin via OA was significantly higher than in all other groups (Figure 15D). There was no difference detectable between IN-treated animals and the control group. Additionally, the distribution of collagen after OA of bleomycin was more homogenous than after IN administration (Figure 16). For the OA route, fibrotic areas appeared all over the lung lobe (Figure 16C), while for the IN route, when compared to saline (Figure 16A), fibrotic lesions appeared mainly around the biggest airways (Figure 16B). No edema or emphysema has been observed by histology for either administration route. However, parenchymal infiltrate was more marked after OA of bleomycin than following IN administration of the antibiotic.

For comparison, the distribution of Cy5.5 for both administration routes has been studied on isolated lungs from a separate cohort of animals using NIRF imaging. Sixty minutes after OA of the dye, a homogenous distribution of the fluorescence signal all over the lung was observed. After IN administration of the dye, at the same time point, the fluorescence signal appeared mainly in the upper part of the lung and the trachea (Figure 17).

A known negative side effect of bleomycin-induced lung fibrosis in small rodents is a prominent loss of body weight. After OA of bleomycin (6 x 0.25 mg/kg), not only the amount of induced lung fibrosis was higher than for IN administration, but also the body weight loss (Figure 15A). For ethical reasons, five out of eight mice had to be sacrificed due to excessive weight loss (~20% of the initial body weight). Thus, for the OA of bleomycin a dose reduction was required. While the initial weight loss was tolerable (<20%) (Figure 18A), an adequate response has been obtained with six times 0.1 mg/kg OA of bleomycin (Figure 18B-D).

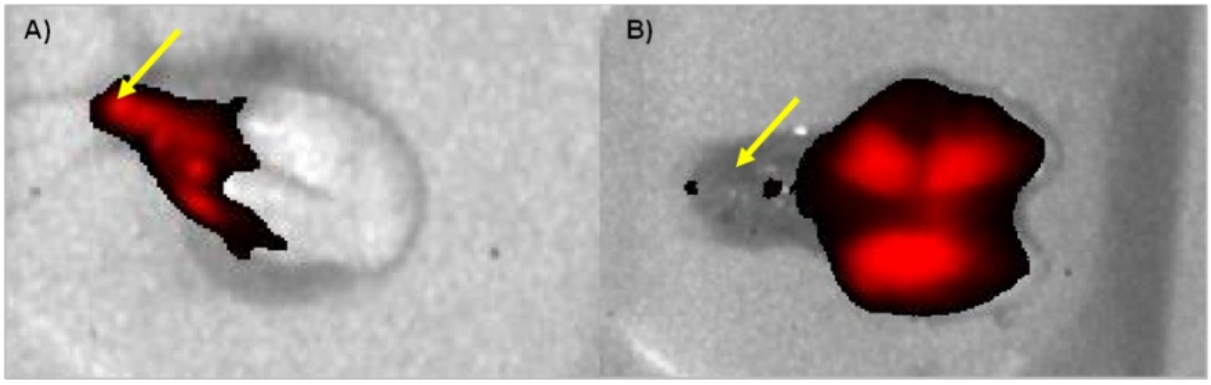

Figure 17: Ventral NIRF images of the lungs from two mice 60 min after instillation of the dye Cy5.5 (0.1mg/mL) either via the IN route (A) or via OA (B). Yellow arrows point to the trachea.

Dose adaptation of OA administered bleomycin in BALB/c mice

The motivation to analyze the effects of OA of bleomycin in BALB/c mice was the fact that many transgenic models have a BALB/c background. Former studies have shown that a much higher dose of bleomycin is needed to induce an amount of lung fibrosis in BALB/c mice that is comparable to the response in C57BL/6 mice [70,90,91]. Thus, an up to ten times higher dose of bleomycin was expected to induce an adequate amount of lung fibrosis in BALB/c mice when using the OA method. Three different doses of bleomycin were tested in groups of eight animals and compared to saline-treated mice. The induced lung injury was detected by UTE-MRI while picrosirius staining as well as determination of hydroxyproline and RT-PCR were

performed *post-mortem*. Compared to baseline, lung injury detected by UTE-MRI was significantly increased in animals treated with either 0.5 or 1.0 mg/kg bleomycin on six consecutive days (Figure 19A). Mice that received bleomycin that was divided between only three days (3 x 1.0 mg/kg, every second day) demonstrated a significant increase of MRI lung signal during the initial phase only (up to nine days after last administration). A treatment with 1.0 mg/kg on six consecutive days induced the significantly highest volume of lung injury in the four compared groups as evidenced by MRI and led to a tolerable loss of bodyweight (≤15 %; data not shown). Regarding *post-mortem* analyses (23 days after last

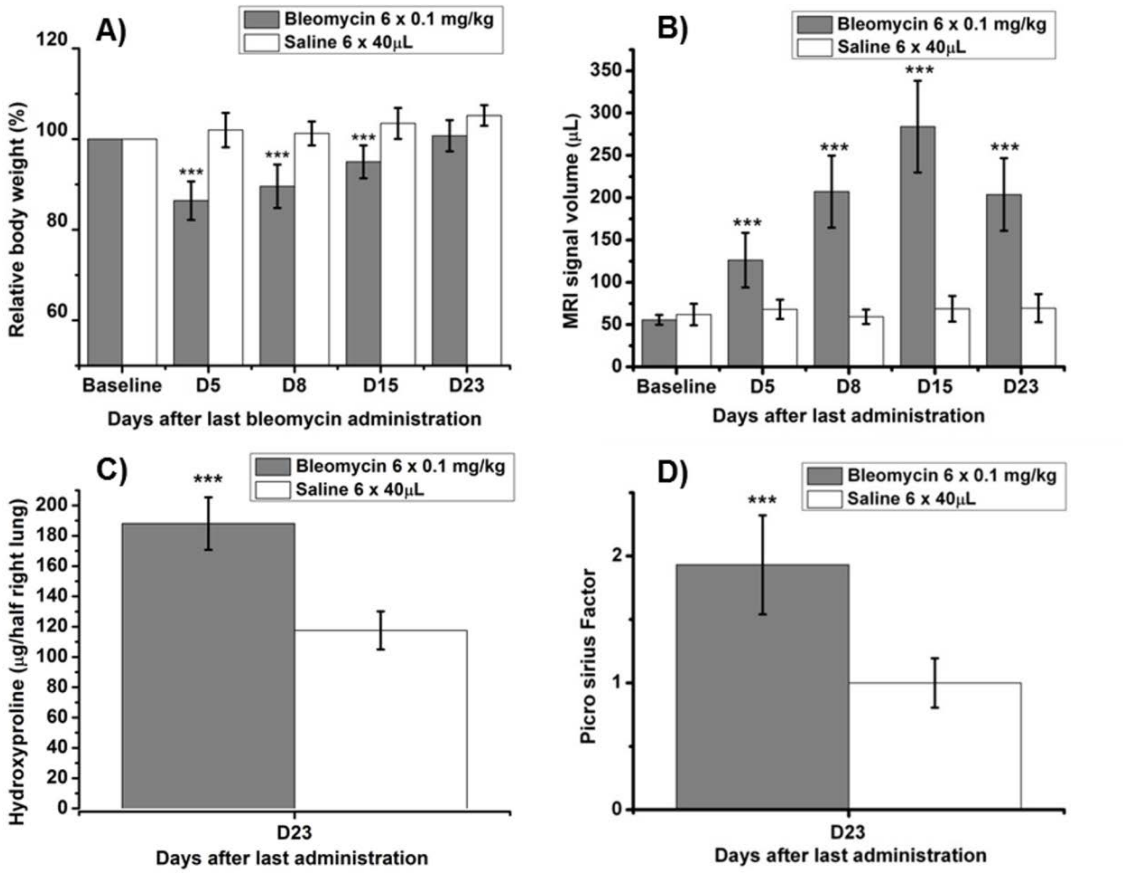

Figure 18: Detection of bleomycin-induced lung injury in C57BL/6 mice by UTE-MRI, picrosirius staining, and hydroxyproline determination. Animals were treated with 0.1 mg/kg bleomycin (n=9) or vehicle (n=5) on six consecutive days via OA. Data are shown as means ± STDEV. A) Relative body weight during the course of the experiment. The statistical significance values ***p<0.001 represent comparisons between saline and bleomycin-treated mice, at each time point. B) Total volume of MRI signals in the lung (µL). The signal at baseline contains contributions from vessels, whereas signals following bleomycin administration reflect additionally the injury induced by the antibiotic. The statistical significance values ***p<0.001 indicate comparison to baseline. C) *Post-mortem* determination of hydroxyproline in right lung lobes D) Picrosirius factor expressing the amount of collagen relative to the mean collagen content assessed in the lungs of saline-treated mice. The statistical significance value ***p<0.001 means comparison to saline treatment.

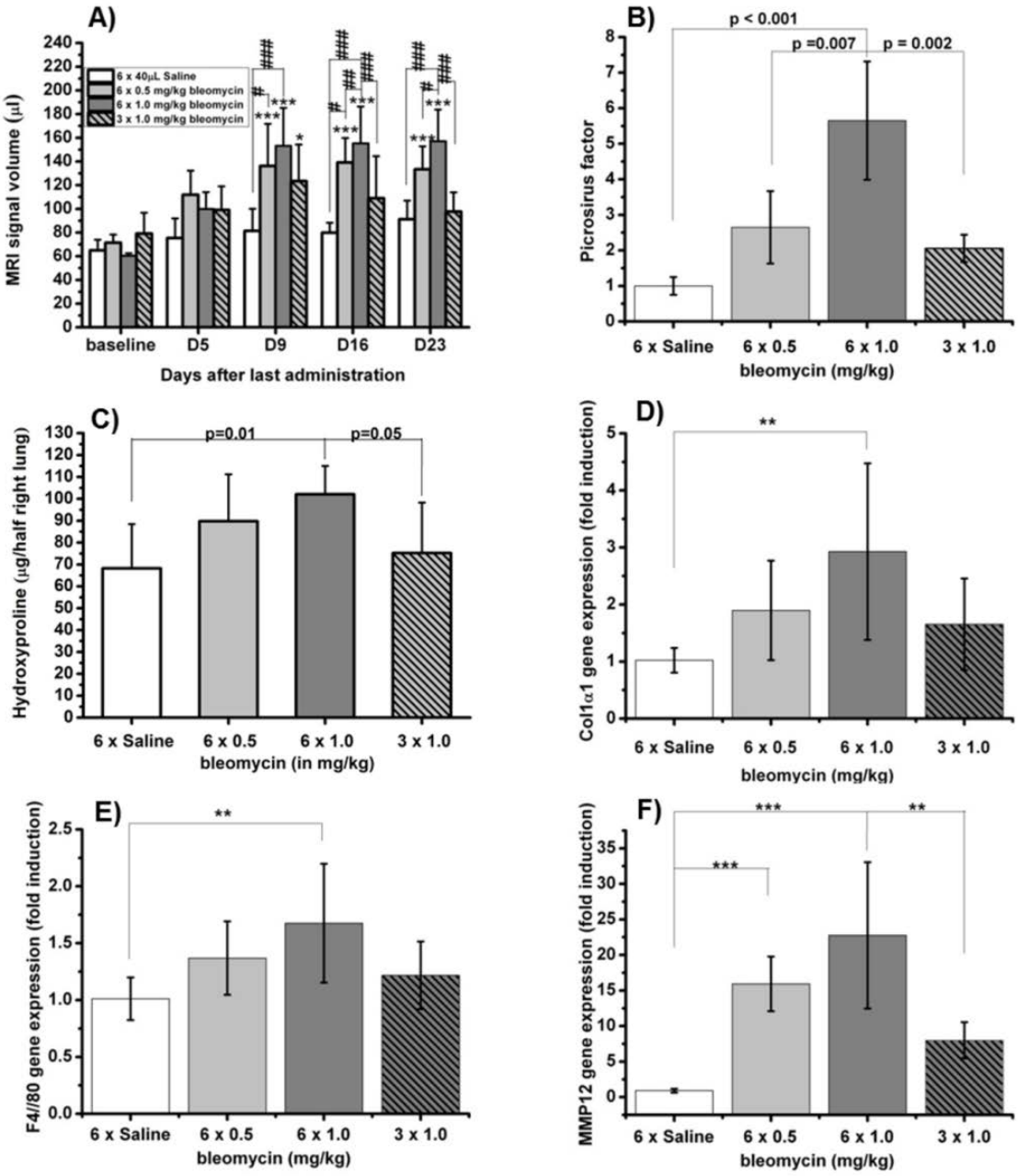

Figure 19: Dose adaptation of bleomycin to OA route and comparison of different bleomycin doses in BALB/c mice by UTE-MRI and *post-mortem* analyses (n=8 mice for each group except n=4 mice for histological analysis). Data are shown as means±STDEV. One-way ANOVA (Two-Way repeated measures ANOVA for MRI-results) with Bonferroni tests was used for statistical analysis. A) Total volume of MRI signals detected in the lung by UTE-MRI The signal at baseline contains contributions from vessels, whereas signals following bleomycin administration reflect additionally the injury induced by the antibiotic. B) Collagen content in left lung lobes detected by picrosirius staining. The picrosirius factor expresses the amount of collagen relative to the mean collagen content in the lungs of saline-treated mice. B) *Post-mortem* determination of hydroxyproline in right lung lobes (day 23); Data are shown as Mean ± STDEV of µg hydroxyproline per right lung. D-F) mRNA expression level of Col1α1, F4/80, and MMP12 compared to expression of HPRT. Data shown as means±STDEV of fold induction compared to control group.

bleomycin administration), only a sixfold administration of 1.0 mg/kg bleomycin induced an amount of lung fibrosis that led to a significant higher amount of collagen as detected by picrosirius staining (Figure 19B), hydroxyproline (Figure 19C), and Col1α1 gene expression (Figure 19D). The expression of MMP12 and F4/80, both markers for the presence of tissue macrophages [92-96], was significantly increased after a sixfold administration of 1.0 mg/kg bleomycin (Figure 19E-F). Neither edema nor emphysema has been observed histologically. Administration of 6 x 0.5 and 3 x 1.0 mg/kg bleomycin led to moderate, 6 x 1.0 mg/kg bleomycin to marked parenchymal cellular infiltration. The correlations between MRI, and all other readouts (picrosirius, hydroxyproline, and gene expression of col1α1, F4/80 and MMP12; Table 1) were significant (p at least 0.005). The strongest correlation (R = 0.90, p<0.00001) was found between the volume of MRI lung signal and the amount of collagen (picrosirius staining).

Correlation between MRI and	**R**	**P**
Picrosirius	0.90	< 0.00001
F4/80 gene expression	0.68	< 0.0001
MMP12 gene expression	0.60	< 0.001
Col1α1 gene expression	0.60	< 0.001
Hydroxyproline	0.48	0.005

Table 1: Correlations between MRI and all other readouts on day 23 analyzed in the present study for detection of bleomycin-induced lung fibrosis in BALB/c mice (n=32; except for Picrosirius n= 16): total MRI signal volume, picrosirius staining, hydroxyproline, and gene expression of Col1α1, F4/80 and MMP12. Saline-treated BALB/c animals (n=8, n=4 for picrosirius) were used as controls.

OA administration in rats

Currently, IT is the most often used route to apply substances into rat lungs. It is a well-established method and may still be the technique of choice for single dosing, but especially for multiple dosing there might be a preference for a less invasive administration route as for instance OA. Since there are not many reports available that describe the use of OA in rats, the feasibility of this administration route has been first tested in a single animal. One hundred microliters of saline were administered via OA, as described before. The liquid was rapidly aspired and no interruption of breathing, which is a common complication during IT administration, occurred. After a single dose of bleomycin (2 mg/kg) via OA, the development of lung injury was detected by UTE-MRI at different time points. Figure 20A shows a significant increase of MRI lung signal already seven days after administration that stayed constant until 21 days after bleomycin administration. A

homogenous collagen accumulation all over the lung with comparable intensity was detected by picrosirius staining in the left lung lobes (Figure 20C).

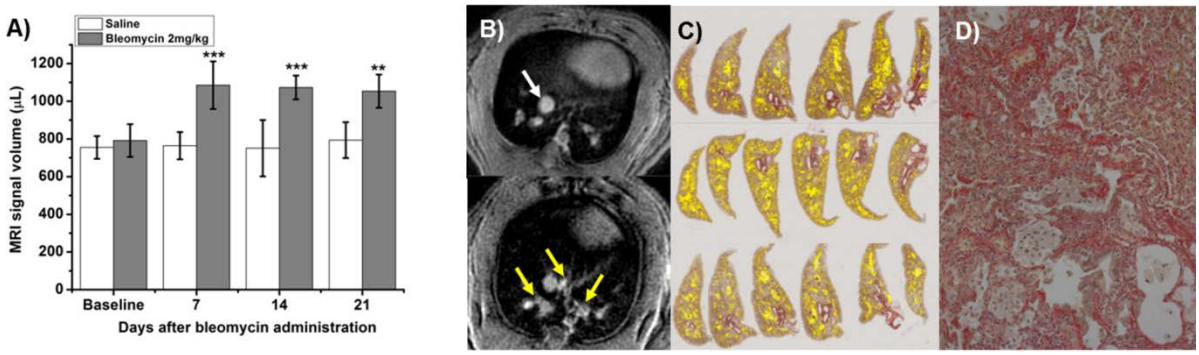

Figure 20: Oropharyngeal aspiration of 2 mg/kg bleomycin or of saline in Sprague Dawley rats (n=5 per group); A) Volumes of signals (means±STDEV) detected by UTE-MRI in the lungs of rats before and after bleomycin; Two-way repeated measures ANOVA with Bonferroni tests was performed. The statistical significance values ***p<0.001, **p<0.01 indicate comparison to baseline as well as comparison to Saline group. B) Signals at baseline contain contributions from vessel (white arrow in upper panel), whereas signals following bleomycin administration reflect additionally the injury induced by the antibiotic (yellow arrows in lower panel). C) Histological analysis of the left lung lobes. Yellow areas are representing collagen, stained by picrosirius; neither emphysema nor edema was observed. D) Magnified view (x200) of one of the histological slices demonstrating widespread fibrosis as evidenced by picrosirius staining.

Discussion

Despite substantial research during the last years, currently no efficacious treatment exists for lung fibrosis. The availability of a robust animal model allowing reliable predictions is important for the development of therapeutics against lung fibrosis. Fibrosis can be modeled in mice by the instillation of bleomycin into the lung [39,97]. Having access to non-invasive imaging is an advantage in the context of therapeutic treatment analysis, as randomization before treatment is feasible and the effect of a therapy on each single animal can be followed longitudinally. This is especially important in view of the variability of the responses induced by bleomycin. For instance, the bleomycin-induced injury can be quantified at a certain time point, just before beginning of treatment. The lung injury quantified non-invasively would then serve as baseline, immediately prior to treatment initiation. Alternatively, the responses induced by bleomycin and quantified by MRI can be used to randomize the treatment groups, in order to have similar mean values at the beginning of treatment across the different groups of animals.

Induction of lung fibrosis by IN or IT administered bleomycin has been used to investigate the effect of potential therapeutics or the influence of genes on the development of lung fibrosis for target finding [98,99]. Since, especially in mice, IT administration is difficult to perform and IN administration might lead to inhomogeneous responses, because of its dependence on different parameters as depth of anesthesia or animal position [64], it seemed to be appropriate to investigate the potential of the OA technique for the described model.

In the present work we demonstrated that the OA administration route offers a possibility to further optimize the murine bleomycin model. Intra-nasal administration and OA of bleomycin were compared in C57BL/6 mice regarding the amount (detected by UTE-MRI, histology, and hydroxyproline determination) and the distribution of induced lung injury. The volumes of administered fluid were chosen based on earlier work [64,65,67]. Using autoradiography Southam et al. [64]have shown that IN administration of 25 µl of fluid to mice leads to a similar uptake in the lung than 40 µl. Conversely, IN administration of lower volumes, e.g. 5 µl, leads to a preferential uptake in the brain. In our hands, we verified that it was easier to administer a volume of 25 µl than of 40 µl, as the latter volume significantly favored the formation of bubbles, resulting in extravasation of fluid out of the nasal cavity. On the other hand, using scintigraphy Foster et al. [20] demonstrated that OA of 50 µl of fluid led to a significantly better uptake in the lungs than 25 µl. We followed the paper of Lakatos et al. [22] and adopted 40 µl for OA delivery. Bleomycin administration via the OA route induced significantly higher amounts of lung injury, detected by MRI *in vivo* and identified as fibrosis by histology, as compared to IN administration. One explanation for this observation might be the obviation of swallowing due to pulling out the tongue during the OA, whereas the animals are, theoretically, still able to swallow during IN administration. A second explanation is proposed by the study of Southam et al., who investigated the distribution of IN administered ^{99m}Tc-labelled sulfide-colloid into different tissues [64]. When 25µL of ^{99m}Tc-labelled sulfide-colloid was administered IN, only 40 - 50 % reached the lung. The rest of the substance could be found in the brain (about 40%) and stomach (5-10%). According to our knowledge, no such study has been performed for the OA route but it might be suggested that, during OA of liquids, less material reaches the brain since the substance does not directly pass the nasal cavity with its access to the brain. Thus, the main part of oropharyngeally aspirated liquid should reach the lung. The more pronounced response induced by the OA of bleomycin allowed a significant

dose reduction from a total of 1.5 mg/kg to 0.6 mg/kg in C57BL/6 mice. This means a model refinement not only due the dose reduction of bleomycin but also because of the accompanying less pronounced body weight loss. Of note, the response induced by IN administration of bleomycin here was lower than that attained earlier for the same model [70]. A possible explanation could be the different suppliers of bleomycin in both studies.

The dose of bleomycin in BALB/c mice could be successfully adapted to OA. A six fold dosing of 1.0 mg/kg bleomycin induced an adequate increase of MRI lung signal which is strongly correlating with lung collagen content (picrosirius), collagen gene expression (Col1α1), hydroxyproline content, and markers for the presence of tissues macrophages that are supposed to be involved in fibrotic processes. The amount of detected MRI signal was of the same order of magnitude as the volume of lung injury in C57BL/6 mice (compare Figures 18B and 19A), and induced a tolerable initial body weight loss of less than 20%. In other words, in order to obtain a similar response in male BALB/c mice as that obtained in male C57BL/6 mice, the total bleomycin dose had to be increased by a factor of 10. This is consistent with previous results obtained using repeated IN administrations of bleomycin, showing that the responses induced by the same total dose of the antibiotic were approximately 10 times weaker in male BALB/c compared to male C57BL/6 mice [70]. Additionally to dose adaptation, it was tested in BALB/c mice whether the number of bleomycin administrations could be reduced from six to three. A threefold dose of 1.0 mg/kg bleomycin did not induce an adequate response as indicated by several readouts (Figure 19). A threefold dose of 2.0 mg/kg bleomycin (identical total dose as the preferred 6 x 1.0 mg/kg) was tested but excluded since the higher single dose evoked breathing interruptions. Therefore, a lower number of bleomycin administrations decreased the amount of induced lung fibrosis and is thus not recommended.

In addition to dose reduction, changing from IN administration to OA of bleomycin evoked another improvement of the lung fibrosis model. There was a clear change apparent regarding localization of fibrotic lesions. Picrosirius staining (Figures 16C and 20C) showed a homogenous distribution of fibrotic lesions after OA in comparison to IN administration of bleomycin (Figure 16B). These different localizations of induced fibrosis can be explained by NIRF images of OA or IN administered Cy5.5 (Figure 17). Whereas 60 minutes after OA of Cy5.5 the fluorescence signal could be detected all over the lung lobes (Figure 17B), the IN administered dye was localized in the trachea and the upper part of lung (Figure 17A).

Assuming that bleomycin is distributed in a comparable manner, this would explain why after IN administration of bleomycin the fibrotic lesions were primarily found around the main airways whereas the OA of bleomycin also induced fibrosis in the periphery of the lung. To have fibrotic areas in the lung periphery might be an important characteristic of a lung fibrosis model since this means a better comparability to the human disease where the deposition of collagen occurs with a peripheral distribution [100].

A similar distribution of fibrotic lesions could be found in rat lungs after OA of bleomycin. Since OA is not a commonly used method for lung instillation in rats, the feasibility was first tested in a small number of animals. The method was found to be easy, fast to apply and effective, since the amount of bleomycin that induced fibrosis was comparable to the amount in IT-treated rats [27]. Thus, OA in rats should be taken into account when a less invasive alternative to IT administration is needed, for instance for multiple dosing.

The UTE acquisition sequence for *in vivo* imaging has been optimized here for increased throughput in view of pharmacological applications. Compared to earlier work [70,72], the acquisition time of MR images of mice lungs could be considerably reduced by the use of the UTE sequence with short echo time. Although the method provides only a global view of the injury induced by bleomycin, the strong correlation ($R=0.90$, $p<0.00001$) between the signals quantified by MRI and the amount of collagen detected histologically (picrosirius staining) indicates that MRI reflected the development of fibrosis in the model. Moreover, although less strong, there was also a significant correlation between the MRI signals and the hydroxyproline content ($R=0.48$, $p=0.005$) as well as the expression of genes that are suggested to be involved in fibrotic processes. The expression of Col1a1, the gene that is encoding for the major component of type 1 collagen, but also the macrophage-specific expression of MMP12 and F4/80 [92-96] were highly correlated ($p < 0.001$) with the MRI signals.

In summary, repeated OA administration of bleomycin led to sustained fibrosis in mice, with an acceptable initial weight loss of less than 15%. The method was easy to perform, fast and effective, as the total dose of bleomycin could be reduced compared to IN dosing. Moreover, a more homogeneous distribution of fibrotic lesions has been obtained than when using IN dosing. In rats, the OA route could be taken into consideration for repeated dosing.

4.2) MRI-detected, bleomycin-induced lung injuries in mice and rats: What is causing the observed changes in MRI signal?

Introduction

Pulmonary fibrosis is a lethal disease and characterized by the infiltration of inflammatory cells and remodeling of ECM including deposition of collagen [22-27]. For *in vivo* studies on pulmonary fibrosis, bleomycin (BLM), an antibiotic used for cancer treatment, is often administered to induce pulmonary fibrosis in small rodents [33-36]. It has been shown before that BLM-induced injuries can be quantified by MRI. The main limitation of the technique is its non-specific nature: although a good correlation to histologically determined collagen has been demonstrated [27,70], the exact nature of the MRI signals remains elusive as they can hardly be distinguished from inflammatory responses. It is unlikely that collagen itself is the main source of the MRI signals during fibrotic processes because of the lack of free protons. Most probably, as during inflammation, free water might induce these MRI signals.

Proteoglycans as hyaluronic acid (HA) are, due their negative charge, able to attract water and are an important part of ECM. Since HA has been shown to be co-localized with collagen [101], to induce collagen production after subcutaneous administration [102,103], and was detectable (after subcutaneous administration) by MRI due to local increase of T2 [104], the possible role of HA on MRI signals in fibrotic lungs of mice has been investigated in this study. Therefore, hyaluronidase (HYAL), an enzyme degrading HA in humans and in small rodents, was administered via OA to BLM-treated mice and rats, with the aim to modulate the MRI signals induced by BLM.

Material and Methods

Ethics Statement

Experiments were carried out with the approval of the Veterinary Authority of the City of Basel (license number BS-1989).

Animals

Seven- to 9-week-old C57BL/6 male mice (n=30) or SD rats (n=12) (Elevage Janvier, Saint Berthevin, France) were used throughout the study. Animals were kept at an ambient temperature of 22 ± 2°C under a 12 h normal phase light-dark cycle and fed NAFAG® pellets (Nahr- und Futtermittel AG, Gossau, Switzerland). Drinking water and food were freely available.

Oropharyngeal aspiration of BLM or saline in mice

Animals were lightly anesthetized with 2% isoflurane delivered in a box and BLM hydrochloride (0.1 mg/kg) in 40 µl of saline (0.9%) or vehicle (40 µl of saline (0.9%)) was administered via OA using a micropipette. OA was performed as described by de Vooght et al. [68]. Mice were fixed on a surgery board, the tongue was pulled out with a forceps, and the liquid was placed onto the distal part of the oropharynx while the nose was gently closed. As for the intra-nasal administration protocol, the procedure was performed six times consecutively, once daily.

Oropharyngeal aspiration of BLM in rats

Animals were lightly anesthetized with 3.5% isoflurane delivered in a box and BLM hydrochloride, 2 mg/kg in 100 µl of saline (0.9%) was administered via OA with a micropipette using a similar procedure as described above for mice.

Administration of hyaluronidase and budesonide.

16-160 U HYAL (from bovine testes, Sigma Aldrich, St. Louis, MO) dissolved in phosphate buffered saline (PBS, Life Technologies, Carlsbad, CA) and 1-3 mg/kg budesonide (BUD) (Sigma Aldrich, St. Louis, MO) solved in 2% dimethyl sulfoxide (DMSO) were administered via OA while the animals were lightly anesthetized with isoflurane delivered in a box (same procedures described for OA delivery of BLM).

Magnetic resonance imaging (MRI)

During MRI signal acquisitions, animals were placed in supine position in a cradle made of Plexiglas. Body temperature was kept at 37±1°C using warm air or a heating pad. Following a short period of introduction in a box, anesthesia was maintained with 1.5% isoflurane for mice and 2% for rats in a mixture of O2/N2O (1:2), administered via a nose cone. All measurements were performed on spontaneously breathing animals; neither cardiac nor respiratory triggering was applied. As demonstrated earlier [70,72], averaging over several respiratory cycles suppressed artifacts caused by movements of the chest and the heart without the necessity of triggering the data acquisition. Measurements were carried out with a Biospec 47/40 spectrometer (Bruker Medical Systems, Ettlingen, Germany) operating at 4.7 T and equipped with an actively shielded gradient system capable of generating a gradient of 200 mT/m. The operational software of the scanner was Paravision (Bruker).

An UTE sequence [73-75] with the following parameters was applied for the detection of BLM-induced lung injury in mice: TR 20.0 ms, TE 601 μs, 604 projections, 2 averages, band width 200 kHz, flip angle of the excitation pulse 25°, matrix size 192x192, slice thickness 1.4 mm and FOV 3.0 x 3.0 cm2. The total acquisition time was of 4.0 min for 10 consecutive axial slices covering the entire lung. A birdcage resonator of 32 mm diameter was used for excitation and detection. For rats an UTE sequence with the following parameters was used: TR 15 ms, TE 801 μs, 604 projections, 2 averages, band width 200 kHz, flip angle of the excitation pulse 25°, matrix size 192x192, slice thickness 1.5 mm and FOV 6.0 x 6.0 cm2. The total acquisition time was of 7.25 min for 24 consecutive transverse slices covering the entire lung. A birdcage resonator of 70 mm diameter was used for excitation and detection.

MR image analysis

At a given time point, the area of BLM-induced lesions was quantified on each image from the dataset covering the whole lung, using a semi-automatic segmentation procedure implemented in the IDL (Interactive Data Language Research Systems, Boulder, Colorado, USA) environment on a Linux system. Images were first low-pass-filtered with a Gaussian profile filter and then transformed into a set of four grey level classes using adaptive Lloyd-Max histogram quantitation. The highest class in the transformed images was extracted interactively by a region grower, whose border was drawn manually on each slice to control

the growing and limit it to areas within the lung (Figure 12). For each image, the area thus segmented by region growing corresponded to high intensity signals in the lung. The total volume of high intensity signals was then calculated by adding the areas obtained for each image from the dataset, and multiplying the summed value by the slice thickness. Segmentation parameters were the same for all analyzed images.

Quantitative real-time polymerase chain reaction (qRT-PCR)

Animals were sacrificed with an overdose of thiopental (Pentothal®, Abbott; 250 mg/kg i.p., 0.2 ml) immediately after an MRI acquisition. The trachea was immediately ligated to avoid collapse of the lung. Removed lung tissue was stabilized in RNA later (Ambion, Zug, Switzerland; #AM7021,) and stored at -80°C until use. For RNA purification, samples were transferred to a 2 ml Eppendorf tube with 1000 µl of RLT buffer (Qiagen, Hombrechtikon, Switzerland; #79216) and β-mercaptoethanol (Sigma-Aldrich, Buchs, Switzerland; #M3148) and one stainless bead (Qiagen, #69989). Samples were homogenized (Qiagen Tissue Lyser, #85300) in two to three 1-min runs at 30 rotations/s each, with 1 min on ice between the runs. After centrifugation for 3 min at 13 000 rpm, 4°C, 300 µl of the resulting supernatant were processed on the Rneasy Mini Kit (Qiagen, #74106) with a DNAse digestion step (Qiagen, #79254), accordingly to the manufacturer's protocol.

Resulting total RNAs were quantified on a NanodropTM system (Wilmington, DE, USA) and 1 µg was reverse-transcribed using the high capacity cDNA RT kit (Applied Biosystems, Zug, Switzerland; #4368813).

Expression of the different genes of interest was evaluated by real time PCR using the ABI Prism 7900HT system. Briefly, 10 ng/µl equivalent RNA per well was distributed in a 384 well plates (Applied Biosystems, #4326270), with 5 µl of the Taqman Universal Mastermix 2X kit (Applied Biosystems, #4324020) and 0.5 µl of 20X Assay-on-demand mix Taqman probe (Applied Biosystem, #4331182). The different probes used and respective genes were: Mm00476206_m1 (HYAL1), Mm01230689_g1 (HYAL2), and Mm00662097_m1 (HYAL3).

Expression for each sample was normalized to HPRT (Mm03024075 m1) and compared to the vehicle-treated group, using the 2-ΔCT formula. The expression of HPRT was the same in both analyzed groups.

Results

HYAL induced changes in BLM-induced MRI signals in mice

In a proof-of-concept study, eight male C57BL/6 mice have been treated with 0.1 mg/kg BLM on six consecutive days. Twelve days after the last administration, half of the animals were treated with 16 U of HYAL while the other four animals received PBS as negative control. Additionally, 16 U of HYAL were administered to two saline-treated animals. Within 24 h the evaluated MRI signal volume tended to increase in HYAL-treated animals, while the average signal volume in both control groups did not change (Figure 21A). The signal increase in the BLM group relative to baseline was about 90 µL at that time point. At 40 days after last BLM administration, a time point at which the MRI signal was still 50 µL above baseline, another dose of HYAL (16 U) induced a slight increase in MRI signal volume in the BLM group overnight but no changes in the control group (Figure 21B).

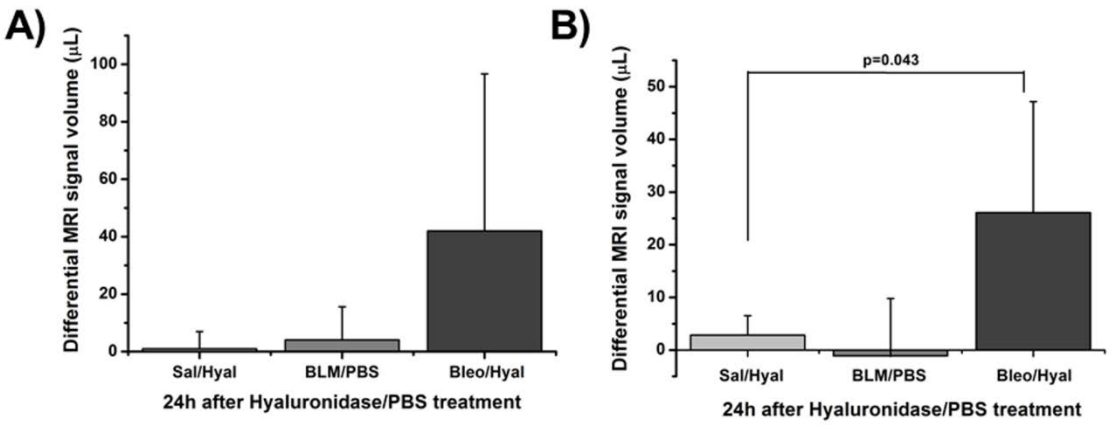

Figure 21: Differential MRI signal volume 24h after HYAL/PBS treatment at A) day 12 and B) day 40 after last BLM administration. For statistical analysis one-way ANOVA with Fisher-Test was applied.

It has been suggested that parts of the ECM and therewith small fragments of hyaluronic acid, which is a degradation product produced by HYAL, are involved in inflammatory processes [105-108]. To investigate whether the observed signal increase could have been caused by inflammation, the same mice were again treated with HYAL/PBS on day 51 after BLM and received3 mg/kg BUD after MRI measurements on day 52. The increased MRI signal in BLM- and HYAL-treated animals was reduced by BUD and reached initial level within 24 h (Figure

22). The combination of BUD and HYAL was then tested in another cohort of n=10 BLM challenged C57BL/6 mice. At day 14 after last BLM challenge (6x0.1mg/kg), treatment started with 1 mg/kg BUD. On the following three days 16 U of HYAL were administered once daily. Mice in the control group (n=8) received vehicle once daily. After two weeks of treatment the relative MRI signal volume was decreased in both groups, but the relative MRI signal volume was slightly lower in the HYAL- and BUD-treated animals (Figure 23).

HYAL induced changes in BLM-induced MRI signal in rats

A combined treatment of BUD (1mg/kg) and HYAL (160 U) was administered to BLM-challenged SD rats. Twelve days after induction of PF by administration of 2 mg/kg BLM via OA, 1 mg/kg BUD was administered via OA directly after MRI measurements. On day 13 another imaging session was performed and the animals were then treated with either HYAL (160 U) or vehicle. No significant change in MRI signal volume occurred 24 h after BUD administration, while the signal volume decreased 24 h after 160 U of HYAL (Figure 24). The difference in MRI signal between the two groups stayed until day 20 after BLM challenge.

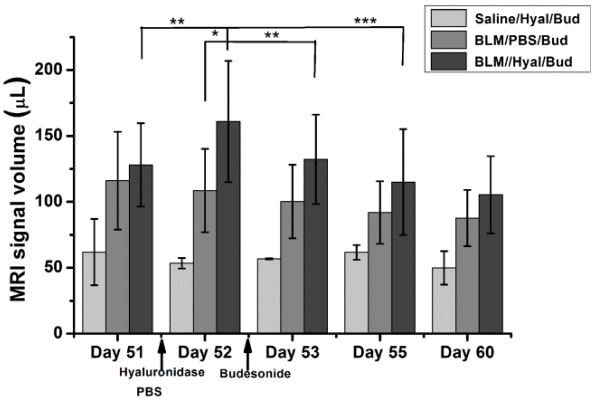

Figure 22: Influence of HYAL and BUD on MRI signal volume at day 51 after last BLM administration in mice. HYAL induced a slight increase in BLM-treated mice. For Statistical analysis Two-Way repeated measures ANOVA with Tukey-Test was applied.

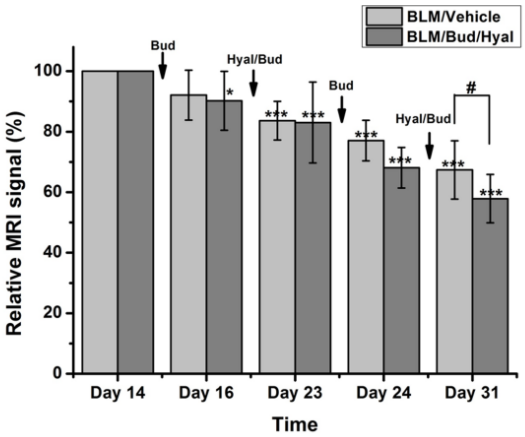

Figure 23: Combination treatment of HYAL and BUD on PF in mice. A Dose of 1mg/kg BUD was followed by three times 16U HYAL per mouse on three following days. Eighteen animals were used for the study; n=10 for Bleo/HYal group and n=8 for the Bleo/Veh group t(wo animals had to be sacrificed because of high body weight loss. For Statistical analysis Two-Way repeated measures ANOVA with Tukey-Test was applied.

Gene expresseion of HYAL increased in the mice BLM model

Gene expression of three types of HYAL (1-3) was determined in lung tissue taken from saline- (n=8) and BLM-treated (6x0.5mg/kg i.n.; n=7) C57BL/6 mice at day 14 after last challenge. Figure 25

shows a reduced expression of the three types of HYAL in BLM- compared to saline-treated mice.

Discussion

In this small pilot-study, the hypothesis was investigated whether HA, a part of ECM, co-localized with collagen [101] and able to attract water, could be contributing to the MRI signals detected after BLM administration. HA plays a role in PF and its production was shown to be increased in humans [109] and rats [110]. A further indication that HA is involved in fibrotic processes is given in this study by the gene expression of HYAL1-3. Cheng et al. have already shown that the expression of HYAL 1 & 2 was decreased in a murine model of asthma, while the expression of hyaluronan synthase 1 & 2, the enzyme responsible for HA production, was increased [101]. In the murine BLM model for PF, the relative gene expression of HYAL1 was reduced and HYAL2-3 showed a tendency to a reduced expression.

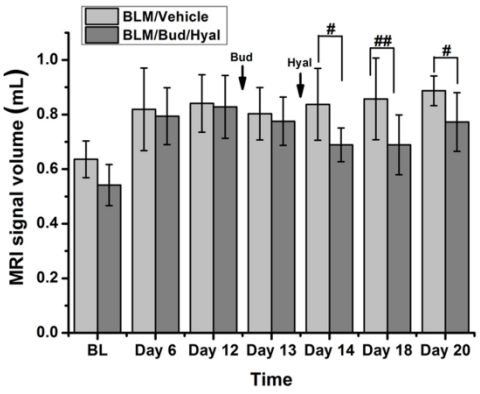

Figure 24: Combined treatment of HYAL and BUD on PF in BLM-treated rats (n=6+6). A dose of 1mg/kg BUD on day 12was followed by OA of 160U HYAL per rat. For Statistical analysis Two-Way repeated measures ANOVA with Tukey-Test was applied.

After administration of HYAL, the enzyme which is degrading HA, the MRI signal showed a tendency to increase in mice at an early time point after BLM administration (day 12) and a significant increase at late time points (days 40 and 51; Figure 21 and 22). The observed signal increase was consistent with published data suggesting that small fragments of HA, resulting

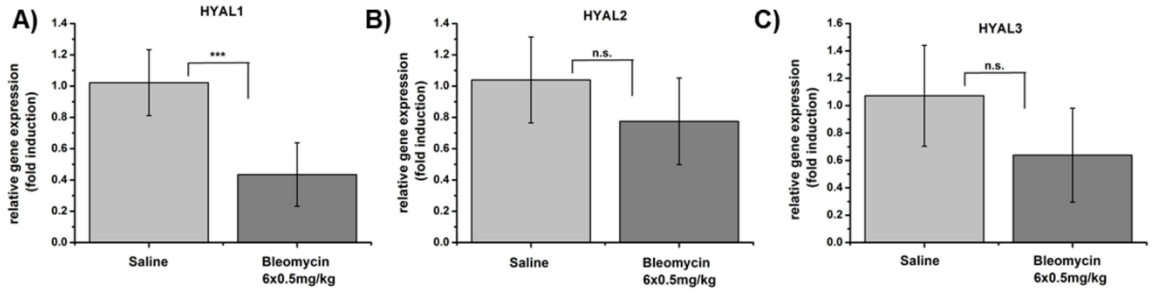

Figure 25: Relative gene expression of HYAL1-3 in lung tissue of saline- and BLM-treated mice (n=8 and n=7, respectively), 14 days after last challenge. HPRT was used as housekeeping gen. For Statistical analysis One-Way ANOVA with Tukey-Test was applied.

from HA degradation, are involved in inflammatory processes [105-108]. Administration of an anti-inflammatory drug (budesonide) led to a reduction of the MRI signal, which supports the hypothesis that the observed signal increase in HYAL-treated mice was due to inflammatory processes (Figure 22). After a combined treatment with HYAL and budesonide the MRI signal could be reduced in BLM-challenged mice and rats (Figures 23 and 24). The observed changes in MRI signal might not have represented a therapeutic effect, since no effect of HYAL and budesonide could be observed histologically or by hydroxyproline determination (data not shown), but it indicates that the MRI signal can be modulated by HYAL, even though the changes are small.

Overall the data of this pilot study support the hypothesis that HA plays a role in the appearance of BLM-induced changes in MRI signal. Since HA has been shown to be involved in fibrotic processes [109,110] and co-localized with collagen [101], the data strengthen the detection of BLM-induced injuries by MRI as a noninvasive *in vivo* readout for PF.

Manuscript:

4.3) "MRI-detected lung volume as a noninvasive readout for tissue deposition in the rat bleomycin model of pulmonary fibrosis"

Christine Egger[1,2], Catherine Cannet[1], Christelle Gérard[1], Andrew Dunbar[1], Bruno Tigani[1], Nicolau Beckmann[1,#]

Novartis Institutes for BioMedical Research, [1]Global Imaging Group, CH-4056 Basel, Switzerland and [2]University of Basel, Biocenter, CH-4056 Basel, Switzerland.

Introduction

Pulmonary fibrosis, a progressive and lethal disease that is characterized by proliferation of fibroblasts and declined lung function, leads to lung damage including accumulation of connective tissue, interstitial pneumonia, and respiratory bronchiolitis [1-3]. A patchy alveolar wall fibrosis develops in patients with chronic obstructive pulmonary disease (COPD) whereas in chronic asthmatics, a fibrotic response occurs predominantly in the lamina reticularis, leading to thickening of the basement membrane [17,18]. In both cases the ongoing inflammation-repair cycle leads to permanent structural changes in the airway wall (remodeling) of which fibrosis is a major constituent [19,20].

Although the pathway of remodeling during the fibrotic processes is still not completely understood, it is so far known that the lung structure is altered by the infiltration of inflammatory cells, thickening of the alveolar walls and deposition of collagen, elastin, and proteoglycans [22-27,111,112]. These changes in lung structure lead to an impairment of lung function. Increased lung tissue resistance and elastance, as well as decreased compliance have been shown in humans [2,15] and in small rodent pulmonary fibrosis models [23-25,28-31]. Moreover, changes in tidal volume and breathing cycle times have been shown in a mouse fibrosis model [113].

Treatment with bleomycin, an antibiotic with activity against gram-negative bacteria [32] and chemotherapeutic properties [114,115], leads to pulmonary fibrosis in about 18% of patients [116,117]. Therefore, bleomycin has become the mainly used substance to model pulmonary fibrosis in small rodents [39,118,119]. Several studies have shown that bleomycin instilled directly into the lung of small rodents elicits an early inflammatory and a late fibrotic response [33-36]. Application of bleomycin causes an acute inflammatory reaction and fibrotic changes that resemble human fibrotic lung disease both histologically and physiologically [22,39].

The availability of the bleomycin model of pulmonary fibrosis provides the opportunity to investigate *in vivo* novel pharmacological approaches aiming to treat this crippling disease [118]. Non-invasive readouts are of importance in the frame of pharmaceutical research, since the ongoing mechanisms during the development of pulmonary fibrosis are still not completely known and target identification and development of therapeutics against PF are challenging. We reported the use of MRI to non-invasively follow the course of lung injury

induced by bleomycin administration to mice [70,120] and rats [27,120,121]. The ability of MRI to non-invasively quantify lung injury in bleomycin-treated animals facilitates *in vivo* pharmacological studies in the model. Repetitive measurements open new avenues in testing compounds as the responses at several time points during the course of treatment can be easily compared. Specifically, studies at the chronic phase, when fibrosis is already established, become amenable.

The present work shows that remodeling of lung tissue, which is induced by OA of bleomycin in rats, leads to an increase of lung tissue weight and lung volume, which can be non-invasively quantified by MRI. The characterization of lung volume changes in the bleomycin model was motivated by the fact that they impact lung function.

Material and Methods

Experiments were carried out with the approval of the Veterinary Authority of the City of Basel (licenses BS-1989 and BS-2565).

Animals

Seven- to nine-week-old SD rats (n=44, age at the beginning of the study) from Elevage Janvier, Saint Berthevin, France, were used throughout the study. Animals were kept at an ambient temperature of 22 ± 2°C under a 12 h normal phase light-dark cycle and fed NAFAG® pellets (Nahr- und Futtermittel AG, Gossau, Switzerland). Drinking water and food were freely available.

Oropharyngeal aspiration of bleomycin or saline in rats

Animals were lightly anesthetized with 2.5% isoflurane (Abbott, Cham, Switzerland) delivered in a box and bleomycin hydrochloride (2-3 mg/kg; Teva, Basel, Switzerland) in 100 µl of saline (0.9%) or vehicle (100 µl of saline (0.9%)) was administered via OA using a micropipette. OA was performed as described earlier [120]. Rats were fixed on a surgery board, the tongue was pulled out with a forceps, and the liquid was placed onto the distal part of the oropharynx while the nose was gently closed.

Magnetic resonance imaging (MRI)

During MRI signal acquisitions, animals were anaesthetized and placed in prone position in a cradle made of Plexiglas. Body temperature was kept at 37±1°C using a heating pad. Following a short period of introduction in a box, anesthesia was maintained with 2.0% isoflurane in a mixture of O_2/N_2O (1:2), administered via a nose cone. Measurements were performed on spontaneously breathing animals. Measurements were carried out with either a Biospec 47/40 or a 70/30 spectrometer (Bruker Medical Systems, Ettlingen, Germany) operating at 4.7 or 7.0 T, respectively. The operational software of the scanners was Paravision (Bruker).

An UTE sequence [73-75] with the following parameters was used for non-gated applications: RT 15.0 ms, TE 801 µs, 604 projections, 2 averages, band width 200 kHz, flip angle of the excitation pulse 25°, FOV 6.0 x 6.0 cm^2, matrix size 192x192, and slice thickness 1.5 mm. The total acquisition time was of 7.25 min for 24 consecutive transverse slices covering the entire lung. In order to have faster acquisitions, a gradient-echo sequence with the following parameters was used for respiratory-gated acquisitions: TR 15.0 ms, TE 2.520 ms, 8 averages (4 averages for gated acquisitions), flip angle of the excitation pulse 10°, FOV 5.0 x 5.0 cm^2, matrix size 256x128, and slice thickness 2.0 mm. Eighteen to twenty-four consecutive transverse slices covered the entire lung. A birdcage resonator of 72 mm diameter was used for excitation and detection.

Respiratory-gated acquisitions

Most acquisitions were performed in spontaneously breathing rats, without gating. For selected experiments, however, it was of importance to acquire images in different respiratory phases of the animal. Therefore, acquisition has been triggered using a small animal monitoring and gating system (model 103—IBP-50, SA Instruments, Inc., Stony Brook, NY, USA). The breathing rate was monitored and kept between 50 and 60 strokes per minute (regulation via anesthesia level). For obtaining images of the lung at the inflated state, data acquisition was performed for a duration of approximately 200 ms with respect to the inspiration peak of the respiratory cycle. The inverted trigger-signal of the breathing cycle was used to acquire data in order to reconstruct images reflecting the lung in the deflated state.

Evaluation of Lung Volume

To evaluate lung volumes (which is defined for this work as total volume of the lung, including tissue, air, and airways), regions of interest (ROI) have been manually drawn around the lung on each acquired slice using the software Paravision. The calculated areas of all ROIs for one animal have been added and multiplied by the slice thickness, resulting in the total lung volume.

Post-mortem analyses

Animals were sacrificed with an overdose of thiopental (Pentothal®, Abbott; 250 mg/kg i.p., 0.2 ml) immediately after an MRI acquisition. The trachea was ligated to avoid total collapse of the lung for histological analysis. For determination of wet weight, dry weight, and hydroxyproline content, all lung lobes were removed without trachea and bronchi.

Histology

Histological analysis was performed as described in more detail earlier [27,120]. Lung lobes were immersed in 10% neutral buffered formalin for 24 h. Following fixation, lungs were trimmed, and three transverse slices were cut through the left lung (superior, median, and caudal parts) to include the main bronchi as well as the pulmonary alveoli. Sections were then dehydrated through increasing graded series of ethylic alcohol and embedded in one block of paraffin wax. Serial sections (3 µm) were stained with picrosirius red for the identification of collagen fibers and newly synthesized collagen.

Determination of hydroxyproline in lung tissue samples

Lung tissue samples were weighed, dried in an oven at 90°C overnight, and the weight was recorded again. Dry tissues were then boiled in 0.5 mL of 6 M HCl at 120°C overnight (8-16 hours) in Pyrex tubes with heat- and acid-resistant screw-on caps (article TES-830-70G; Fisher Scientific, Wohlen, Switzerland). After cooling down and adding 5 µL of phenolphthalein (1%), the samples were neutralized with NaOH 10 M (Sigma N°S-5881) and 6 M HCl. Black precipitate and brown color was removed by adding 100 µL of carbon suspension [10 mg/mL activated charcoal (article C4386; Sigma-Aldrich, Buchs, Switzerland) in water], centrifugation, and filtration. Five microliters of standard or hydrolyzed sample were pipetted in triplicates

onto a 96 well plate, and 5 µL citrate acetate buffer (5% citric acid, 7.2% sodium acetate, 3.4% sodium hydroxide, 1.2% glacial acetic acid, distilled water) was added to each well, as well as 100 µL of freshly prepared chloramine-T solution (14.1mg chloramine-T, 0.1mL n-propanol, 0.1mL distilled water, 0.8mL citrate acetate buffer). The samples were then incubated at room temperature for 20 minutes. After adding 100 µL of Ehrlich's reagent (2.5 g of 4-(dimethylamino)benzaldehyde, 9.3 mL of n-propanol, and 3.9 mL of 70% perchloric acid), the wells were incubated for 20 minutes at 65°C. After cooling down, the samples were measured at 550 nm on a spectrophotometer (SpectraMax 340PC, Molecular Devices, Sunnyvale, CA, USA); a standard curve from 5 to 100 mg hydroxyproline in water was created. Data were expressed as µg/right lung lobe.

Statistics

For statistical analysis the software SigmaPlot™ (Systat Software Inc., San Jose, CA, USA) has been used. One-way ANOVA and t-tests have been performed for endpoint readouts while Two-way repeated measures ANOVA with Tukey tests have been used for readouts with multiple measurements. The following abbreviations were used for the indication of significance: */#: $0.01<p<0.05$; **/##: $0.001\leq p \leq 0.01$ ***/ ###: $p< 0.001$.

Results

Bleomycin induces an increase in MRI detected lung volume in rats

SD rats that have been treated with a single dose of bleomycin (2mg/kg OA) showed enlarged lung areas on non-gated UTE-MR images (Figure 26A). Therefore, lung volume of bleomycin challenged rats have been determined, by defining the lung area on each image and calculating the lung volume as described in the method section, and compared to the lung volume of healthy animals. Within seven days bleomycin-treated rats showed a significant increase in MRI-detected lung volume (Figure 26B) that persisted until the end of the experiment (21 days after challenge). The determined lung volume of bleomycin treated rats was significantly higher compared to vehicle group, even though the lung volume of healthy animals increased slightly with age.

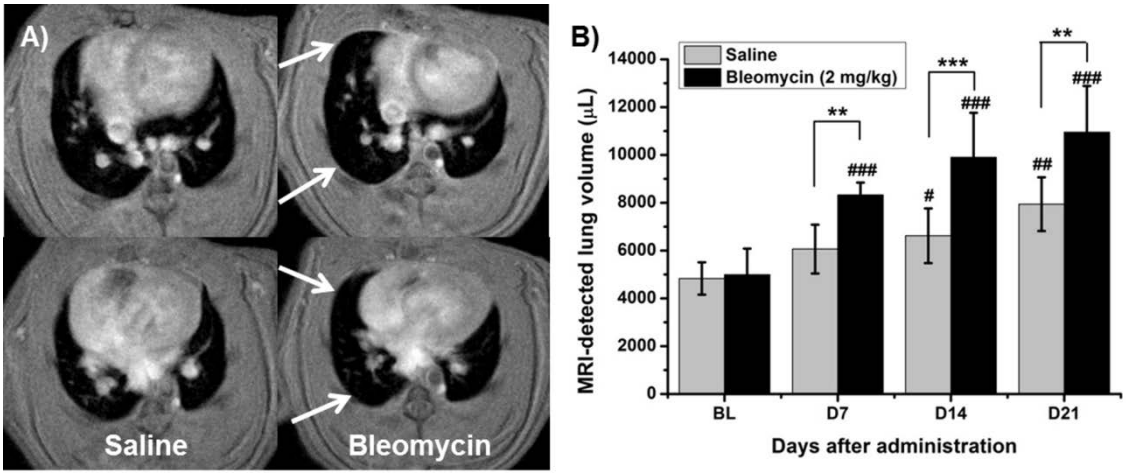

Figure 26: Bleomycin-treated rats showed increased total lung volumes as compared to control, saline-challenged animals. A) Images acquired at 7 T of saline- (left) and bleomycin-treated rats (right), 14 days after challenge; arrows point to enlarged lung areas. B) Quantified increase of MRI-detected lung volume in bleomycin treated rats (n=5) compared to saline treated animals (n=5). Data are shown as mean ± STDEV; significance level above bars mean significance to baseline; Two-way repeated measures ANOVA was applied.

Influence of breathing rate and physiological growth on lung volume detected by non-triggered UTE-MRI

Non-triggered MRI acquisitions of the lung result in an averaged image over all respiratory phases [122]. Factors as for instance bodyweight and therewith growth of lung or breathing rate of the animal might have an influence on the evaluated lung volume. In a first study we investigated the influence of breathing rate, length of narcosis and body weight on detected lung volume. Six healthy SD rats have been imaged by UTE-MRI during four weeks. During all imaging sessions the breathing rate has been monitored. No correlation has been found between the lung volume assessed by MRI and the breathing rate (Figure 27A). In order to investigate the possible influence of time in anesthesia on the detected lung volume, a second image has been acquired approximately 15 minutes after the first acquisition (resulting in a total anesthesia time of about 35 minutes, including induction time). When the animals were kept for a longer time in anesthesia, the detected lung volume decreased (Figure 27B). Therefore, in routine applications and non-gated acquisitions, care was taken to maintain the total anesthesia time approximately the same and under 15 minutes per session.

Saline-treated animals showed a slight increase in lung volume over 21 days (Figure 26B). This effect may be rather explained by physiological lung growth than by effects of saline

instillation. Formulas that were published by Mirfazaelian et al. [123] for calculating the weight of certain rat organs led suggest that the rat lung can grow until the age of approximately 14 weeks (Figure 27C). For predicting the physiological increase in lung volume, the ratios between the lung wet weights and the corresponding MRI-detected lung volumes have been assessed from several studies, resulting in an averaged lung density of 0.21±0.019 mg/mL (±STDEV). Introducing the averaged lung density into the formula of Mirfazaelian et al. [123], the increase of lung volume due to growth has been predicted

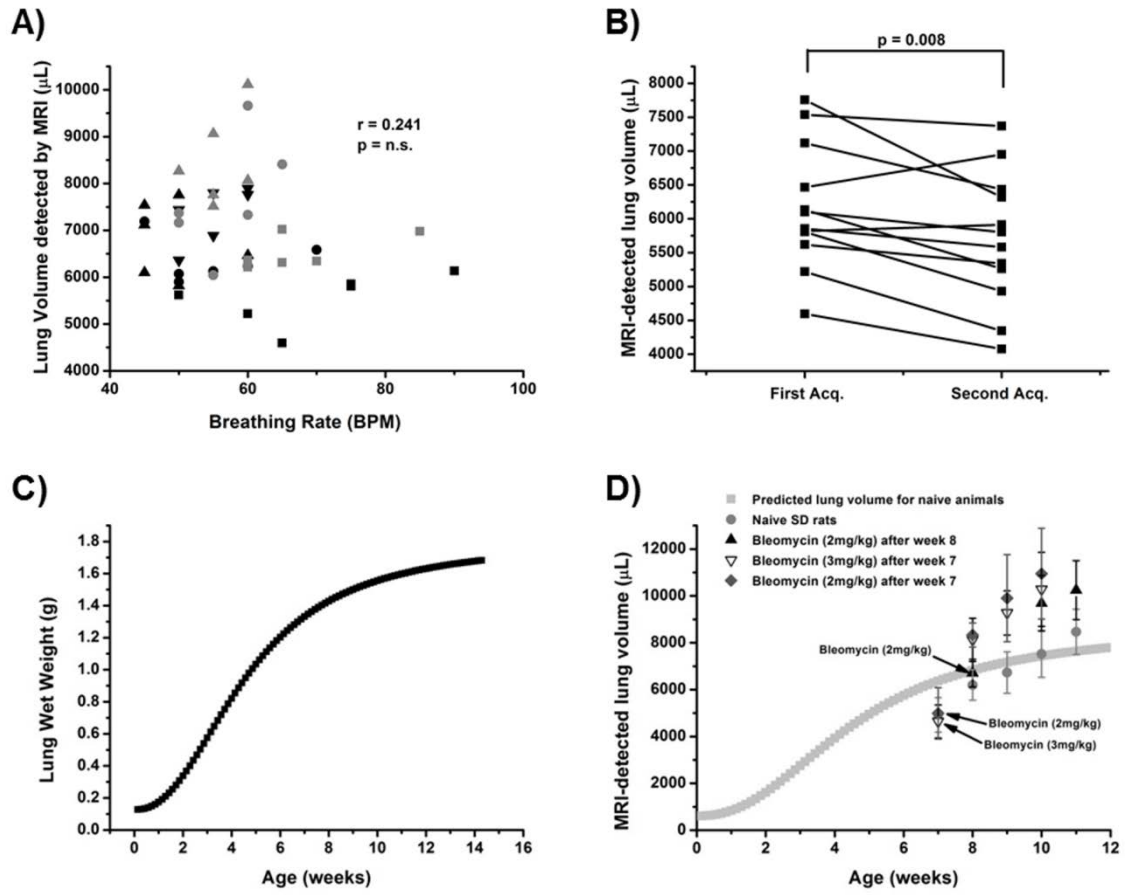

Figure 27: A) Correlation between breathing rate (breaths per minute) and MRI-detected lung volume. Lung volume of 2x6 naïve or saline-treated rats at seven different time points within 3 weeks have been evaluated. One symbol represents one group of six rats at one time point; Linear Fit showed no significant p-value B) Influence of narcosis on MRI-detected lung volume in n=6 animals at two different time points. The time between the first and the second acquisition was about 15 minutes; Lines are linking results of the same animal. C) Prediction for lung wet weight development in SD rats using the formula of Mirfazaelian et al. [123]. D) Prediction for lung volume of naïve SD rats (grey curve) using the formula of Mirfazaelian et al. [123] and averaged lung density of collected data from several studies. MRI-detected lung volumes for naive animals and bleomycin treated rats are shown as mean ± STDEV; arrows point to treatment start.

(Figure 27D). The lung volumes of naive SD rats (n=6) assessed by UTE-MRI were comparable to the predicted lung volumes (Figure 27D). The administration of different doses of bleomycin in rats of different age let in all cases to an increase in MRI-detected lung volume, that clearly differed from the physiological growth of lung volume in naive rats (Figure 27D).

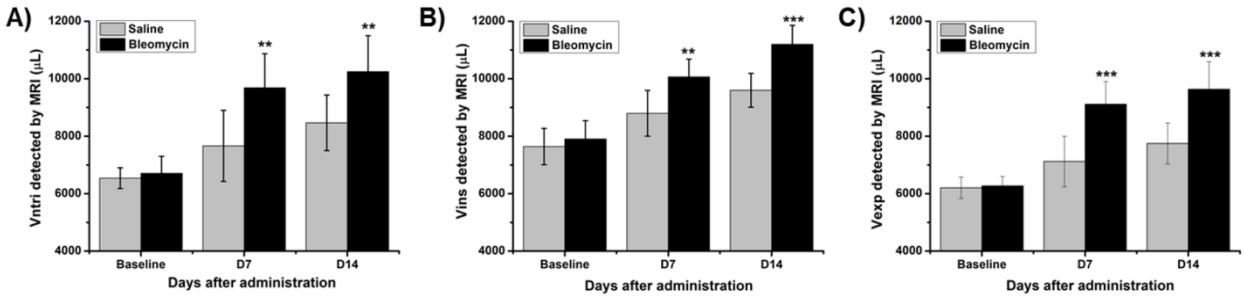

Figure 28: MRI-detected lung volume of saline (n=6) and bleomycin (2mg/kg) treated rats (n=6) in different phases of breathing cycle. A) Non-triggered MRI. B) Vins, Lung Volume in the inflated state. C) Vexp, Lung volume in the deflated state. Data are shown as mean ± STDEV; Significance level result from comparison to saline group at the same time point. Two-way repeated measures ANOVA was applied.

Characterization of lung volume detected by MRI

Twelve male SD rats have been examined during three weeks by MRI. After baseline measurements all animals have been treated with either 100 µL of saline (0.9%) or bleomycin (2mg/kg) via OA. At each time point, a non-triggered acquisition was followed by two gated acquisitions to reflect inflated and deflated state, as described in the methods section.

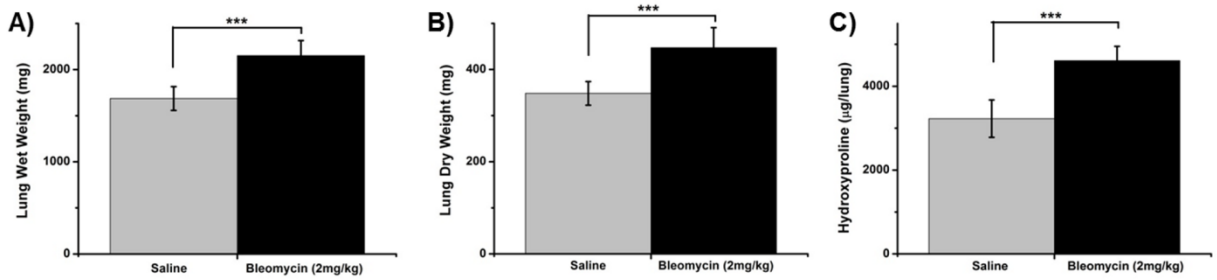

Figure 29: *Post-mortem* analysis A) Terminal lung wet weight, two weeks after challenge; data are shown as mean ± STDEV; One-way ANOVA was performed. B) Terminal lung dry weight, two weeks after challenge; data are shown as mean ± STDEV; One-way ANOVA was performed. C) Hydroxyproline content in all five lung lobes, two weeks after challenge; data are shown as mean ± STDEV; One-way ANOVA was performed.

Bleomycin-treated animals showed, compared to the vehicle group, a significant increase in non-triggered-MRI detected lung volumes (Vntri); similarly, the volumes of inflated (Vins) and deflated lungs (Vexp) were also increased (Figure 28A-C). Animals of the control group showed a slight increase in lung volumes that was comparable to the increase in lung volume of naive animals (Figure 28A-C, see also Figure 27D). The wet and dry weight of all five lung lobes have been determined *post-mortem* and were significantly higher in the bleomycin group (Figure 29A-B). The hydroxyproline content, determined in all five lung lobes, was significantly increased after bleomycin administration (Figure 29C). The relative water content was the same in both groups (79.3 % for saline, 79.2% for bleomycin group). Correlations between the lung volumes derived by MRI (non-triggered and triggered acquisitions), dry and wet lung weights, as well as hydroxyproline content are presented in Figure 30A-D.

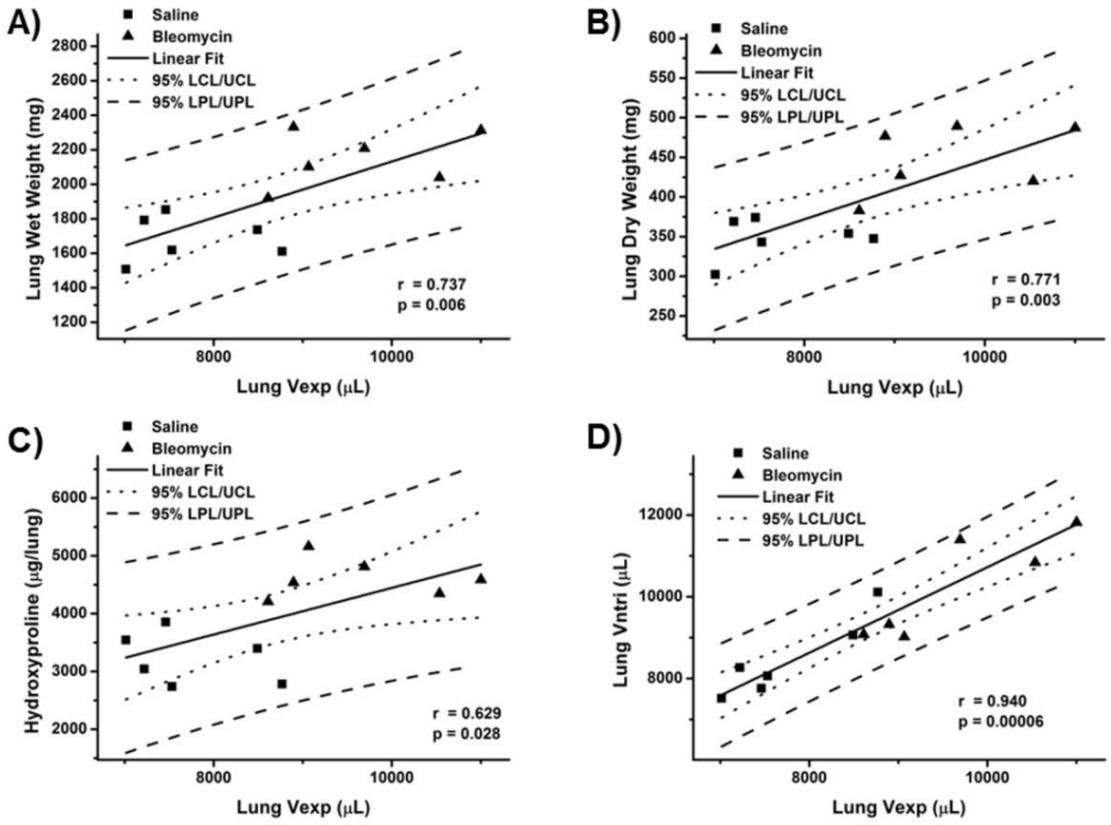

Figure 30: A) Correlation between lung wet weight and MRI-detected lung volume in expiration phase (Vexp) of saline and bleomycin treated SD rats (n=6+6) two weeks after challenge. B) Correlation between lung dry weight and MRI-detected lung volume in expiration phase (Vexp) of saline and bleomycin treated SD rats two weeks after challenge. C) Correlation between hydroxyproline content of all five lung lobes and MRI-detected lung volume in expiration phase (Vexp) of saline and bleomycin treated SD rats. D) Correlation between MRI-detected lung volume in expiration phase and without triggering.

Figure 31 summarizes histological evidence of collagen deposition in the lungs of rats treated with bleomycin (2 mg/kg, OA route). Histology also revealed perivascular, peribronchial and parenchymal infiltration of inflammatory cells. However, no edema has been detected. Also, no emphysema was present in the lung sections.

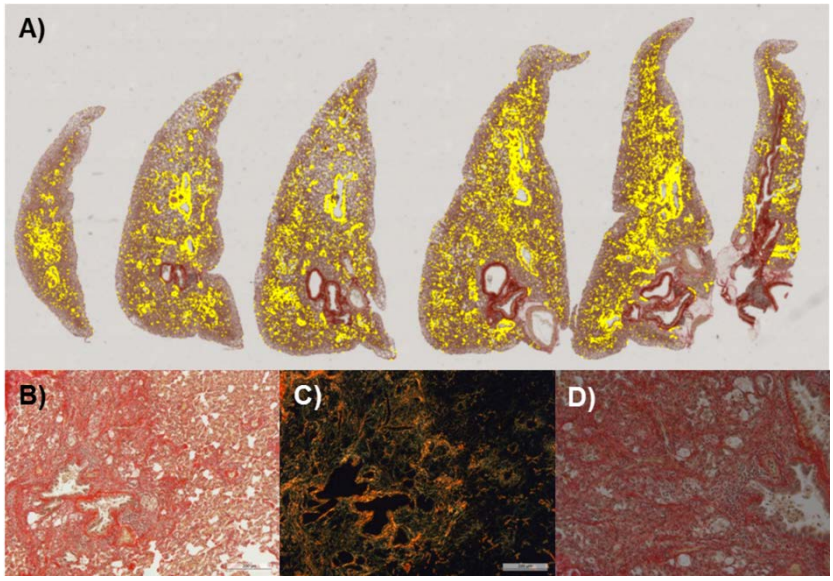

Figure 31: Histological analysis of bleomycin treated (2mg/kg, OA) left rat lung lobes, at day 21 after administration of the antibiotics. A) Picrosirius staining; yellow areas represent picrosirius stained collagen ; View under bright field light (B) and polarized light (C); D) 20x magnified view under brightfield light ; neither emphysema nor edema could be observed.

Discussion

Despite substantial research during the last years, currently no efficacious therapy and only few non-invasive *in vivo* diagnostic tools for lung fibrosis exist. The availability of such methods and a representative animal model would be of great importance for the development of therapeutics against lung fibrosis. It has been shown in former studies that fibrosis can be modeled by the instillation of bleomycin into the lung [39,97]. Induction of lung fibrosis by instillation of bleomycin has often been used to investigate the effect of potential therapeutics or the influence of genes on the development of lung fibrosis for target finding [33,98,99].

It has been shown earlier that proton MRI techniques are able to non-invasively follow the progression of bleomycin-induced lung injury in rats [27,120,121,124] and mice [33,120]. The signals quantified by MRI in the lung showed high correlation to histological analysis of collagen and to hydroxyproline content. In the present work we aimed at validating lung volume as an alternative readout that might reflect changes in lung function in the model, since the improvement of lung function is a main aim for therapeutics against several lung diseases.

The lung volume detected by non-triggered MRI increased after instillation of bleomycin (Figures 26 and 27D). An increase in lung volume has also been reported earlier for non-triggered MRI acquisitions of spontaneously respiring rats following an intra-tracheal administration of elastase [125], due to emphysema induced by the enzyme. No emphysema could be observed in histological analysis of rat lungs after instillation of 2 mg/kg bleomycin (Figure 31). Also, the presence of edema was excluded by histology and by the fact that the relative water content of 79% did not change upon instillation of bleomycin (data not shown). Breathing rate or anesthesia showed no or only slight influence on MRI-detected lung volume and could not explain the observed increase after instillation of bleomycin (Figure 27A,B). Finally, the increase in lung volume after bleomycin administration was clearly more pronounced than that expected from the physiological growth-curve (Figure 27D). Therefore, the increase in lung volumes following bleomycin detected with non-gated MRI acquisitions had to be related to either anatomical or lung function changes, or by a combination of both.

Similarly to non-gated images, respiratory-triggered acquisitions of bleomycin-challenged rats showed a significant increase in lung volume both in the inflated (Vins) and deflated (Vexp) state (Figure 28A-C). Therefore, the increase in lung volume on non-gated images of bleomycin-treated animals evolved from a significant increase of Vins but also Vexp. Since neither emphysema nor edema could be observed in this model, the increase in lung volume after expiration (Vexp) can only be explained by either air that remained in the lung as a consequence of a loss in lung function or by tissue remodeling due to the deposition of collagen, elastin, and proteoglycans [22-27]. The *post-mortem* assessed lung wet and dry weight, as well as hydroxyproline content (Figure 29A-C) and picrosirius staining (Figure 31) as markers for collagen deposition, were all increased in bleomycin-treated rats. These observations indicate that the increase in MRI-assessed lung volumes in the bleomycin group (Figure 28A-C), particularly of Vexp was due to tissue deposition (remodeling) induced by the antibiotic. This suggestion is reinforced by the correlation of Vexp to lung wet weight (Figure 30A), dry weight (Figure 30B) and hydroxyproline (Figure 30C): an examination of the linear fits reveal that an increase of Vexp from 8 to 10 mL corresponded to a relative increase of the other readouts (Figure 30A-C) by the same amount (around 25%) The strong correlation of Vexp to Vntri (Figure 30D) with a ratio of about 1.0 demonstrates that not only volume

assessments at the expiratory phase (Vexp) but also the less time-consuming non-gated assessments (Vntri) provide a readout for bleomycin-induced tissue deposition in rats.

Tissue deposition in the lung, as for instance collagen, elastin, and proteoglycans, induced by bleomycin correlates to an increase in lung resistance [23,24,26,111,112] and therewith to a decrease in lung compliance. Therefore, MRI-detected alterations in lung volume, which in this work were shown to be related to increases of lung wet and dry weight as well as of collagen content, may also be considered as reflecting changes of lung function in the model. As measurements are performed in spontaneously breathing rats, it is recommended to keep the animals at approximately the same time in anesthesia (at maximum 20 minutes) in each imaging session, since prolonged anesthesia may lead to a reduction of the total lung volume. Moreover, the physiological growth of the lung needs to be taken into account by the incorporation of appropriate control groups or by correcting the assessed lung volumes using the formula of Mirfazaelian et al. [123]. As therapies aim primarily at improving the lung function, incorporation of this readout into pharmacological testing in the bleomycin model could be of interest. Further pharmacological validation and comparison to invasive functional tests is warranted in order to qualify this anatomical readout as noninvasive marker of changes in lung function in spontaneously breathing, bleomycin-challenged rats.

5) MRI-detected effects of two compounds on pulmonary fibrosis in the bleomycin model

Manuscript:

5.1) "Therapeutic Effects of the Fibroblast Activation Protein Inhibitor, PT100, in a Murine Model of Pulmonary Fibrosis"

Christine Egger[1,3], Catherine Cannet[1], Christelle Gérard[1], Iwona Ksiazek[2], Agnès Feige[2], Thomas Suply[2], Andrew Dunbar[1], Bruno Tigani[1], Nicolau Beckmann[1,#]

Novartis Institutes for BioMedical Research, [1]Global Imaging Group, CH-4056 Basel, Switzerland, [2]Developmental and Molecular Pathways Department, CH-4056 Basel, Switzerland; and [3]University of Basel, Biocenter, CH-4056 Basel, Switzerland.

Introduction

Pulmonary fibrosis, characterized by fibroblast proliferation and ECM remodeling, is the end result of diverse types of severe lung damage that include usual interstitial pneumonia, desquamative interstitial-pneumonia, non-specific interstitial pneumonia, respiratory bronchiolitis interstitial lung disease, and acute interstitial pneumonia [1-3]. In patients with chronic obstructive pulmonary disease a patchy alveolar wall fibrosis develops whereas in chronic asthmatics, a fibrotic response occurs predominantly in the lamina reticularis, leading to a thickening of the basement membrane [17,18]. In both cases the ongoing inflammation-repair cycle leads to permanent structural changes in the airway wall (remodeling) of which fibrosis is a major constituent [19,20]. However, up to 50% of the cases of pulmonary fibrosis are defined as IPF [21]. Current therapies for IPF are not particularly effective and involve treatment with corticosteroids and other immunosuppressive/cytotoxic agents such as prednisone and cyclophosphamide [126].

Bleomycin (BLM) is an antibiotic with activity against gram-negative bacteria [32] that also possesses chemotherapeutic properties and is highly efficient in some types of carcinomas. However, BLM produces a dose-dependent pulmonary fibrosis in most patients [21]. A single IT instillation of BLM is commonly used to induce experimental pulmonary fibrosis in rodents [33-35]. In this animal model, the single application of the antibiotic causes an acute inflammatory reaction and fibrotic changes that resemble human fibrotic lung disease both histologically and physiologically [22,39]. The availability of this animal model of pulmonary fibrosis provides the opportunity to investigate novel pharmacological approaches that can be used to treat and prevent this crippling disease.

Talabostat mesilate (PT100) is an orally active, specific inhibitor of dipeptidyl peptidases, including tumor-associated fibroblast activation protein (FAP) [127]. By an independent mechanism, talabostat also stimulates the upregulation of cytokines and chemokines to engender a tumor-specific host immune response, thus giving it a unique dual mechanism of action. In clinical trials, talabostat has demonstrated significant activity, including achieving complete responses in patients with non-small-cell lung cancer and malignant melanoma. In house, the compound has shown encouraging results in a mouse kidney fibrosis model. These data provide the rationale for testing the compound in a second fibrosis model.

In the present study proton MRI was applied to assess non-invasively and in spontaneously breathing mice the effects of PT100 on established fibrosis following repeated IN application of BLM [70]. *Post-mortem* histological and qRT-PCR analyses were performed on lung samples to validate the MRI readouts.

Methods

Experiments were carried out with the approval of the Veterinary Authority of the City of Basel (license number 1989).

Animals

Seven- to 9-week-old C57BL/6 male mice (n=32, Charles River, L'Arbresle, France) were used throughout the study. Animals were kept at an ambient temperature of 22 ± 2°C under a 12 h normal phase light-dark cycle and fed NAFAG® pellets (Nahr- und Futtermittel AG, Gossau, Switzerland). Drinking water was freely available.

Intra-nasal administration of bleomycin or saline

Mice were lightly anesthetized with 1.5% isoflurane (Abbott, Cham, Switzerland) in a chamber and bleomycin hydrochloride (0.5 mg/kg; Euro Nippon Kayaku, Frankfurt am Main, Germany) in 25 µl of saline or vehicle (25 µl of saline) was administered IN via a micropipette (12.5 µl per nostril). This procedure was performed six times, on days -7, -6, -5, -2, -1, 0.

Study groups

PT100 (NVP-CGQ158-AA-3; 40 µg/mouse, dissolved in 0.9%NaCl) or vehicle was dosed per os (p.o.) by gavage twice daily (at approximately 8 am and 5 pm) from day 1 to day 14 after last BLM application. Animals were divided into the following groups: Saline-challenged mice (n=8) have been treated with PT100 vehicle (0.9%NaCl), BLM-challenged mice (n=12) with PT100 vehicle, and BLM-challenged mice (n=12) with PT100.

Mice were randomized into groups 2 or 3 according to the BLM-induced responses detected by MRI at day 0, in order to have the same mean lesion volumes in both treatment groups at the beginning of compound dosing. Animals displaying a weight loss of more than 20% were sacrificed before the end of the study.

Magnetic resonance imaging (MRI)

During MRI signal acquisitions, mice were placed in supine position in a cradle made of Plexiglas. Body temperature was maintained at 37±1°C using warm air. Anesthesia was maintained with 1.3% isoflurane, in a mixture of O2/N2O (1:2), administered via a nose cone. All measurements were performed on spontaneously breathing animals; neither cardiac nor respiratory triggering was applied. As demonstrated earlier [72] averaging over several respiratory cycles suppressed artifacts caused by movements of the chest and the heart without the necessity of triggering the data acquisition. Measurements were carried out with a Biospec 47/40 spectrometer (Bruker Medical Systems, Ettlingen, Germany) operating at 4.7 T and equipped with an actively shielded gradient system capable of generating a gradient of 200 mT/m. The operational software of the scanner was Paravision (Bruker).

An UTE sequence [73] with the following parameters was applied for the detection of BLM-induced lung injury: TR 9.5 ms, TE 651 µs, 314 projections, 32 averages, band width 200 kHz, flip angle of the excitation pulse approximately 10°, matrix size 150x150, slice thickness 1.4 mm and FOV 2.5x2.5 cm2. The total acquisition time was of 15.9 min for 10 consecutive transverse slices covering the entire lung. A birdcage resonator of 32 mm diameter was used for excitation and detection.

MR image analysis

At a given time point, the area of BLM-induced lesions was quantified on each of the 10 images covering the whole lung, using a semi-automatic segmentation procedure implemented in the IDL (Interactive Data Language Research Systems, Boulder, Colorado, USA) environment on a Linux system. Images were first low-pass-filtered with a Gaussian profile filter and then transformed into a set of four grey level classes using adaptive Lloyd-Max histogram quantitation. The highest class in the transformed images was extracted interactively by a region grower, whose border was drawn manually to control the growing (Figure 12). The total volume of high intensity signals was calculated by adding the areas obtained for each of the 10 images, and multiplying the summed value by the slice thickness. Segmentation parameters were the same for all analyzed images, chosen to segment regions corresponding to high intensity signals. Because the lesion signals and those from vessels were of comparable intensities, the volume corresponding to the vessels was assessed on baseline images and

then subtracted from the volumes determined on post-treatment images. Differential signal volumes (parsed, baseline-subtracted data) reflecting the BLM effects are presented. Thus, for each mouse, the volume of high intensity signals present in baseline images was subtracted from the volumes evaluated at later time points.

Post-mortem analyses

Animals were sacrificed with an overdose of thiopental (Pentothal®, Abbott, Baar, Switzerland; 250 mg/kg i.p., 0.2 ml) immediately after the MRI acquisitions. The main left bronchus was immediately ligated to avoid collapse and the left lung was removed for histological analyses. The right lobes of the lung were used for qRT-PCR.

Histology

As described earlier [72], left lungs were immersed in 10% neutral buffered formalin for 24 h. Following fixation, lungs were trimmed, and three transverse slices were cut through the left lung (superior, median, and caudal parts) to include the main bronchi as well as the pulmonary alveoli. Sections were then dehydrated through increasing graded series of ethylic alcohol and embedded in one block of paraffin wax. Serial sections (3 µm) were stained with hematoxylin and eosin (H&E) to assess the general morphology, PAS for demonstrating excreted mucus and mucus-containing goblet cells, and picrosirius red for the identification of collagen fibers and newly synthesized collagen.

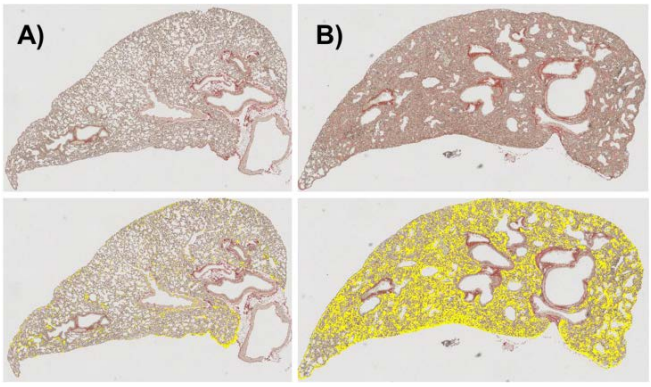

Figure 32: Quantification of picrosirius-stained histological slices of the lungs of mice, at day 14 after last administration of saline (A) or BLM (B). Areas corresponding to collagen accumulation were automatically recognized (yellow zones, lower panel). In these examples, the percentage of collagen areas were of 0.5 and 7.0%, respectively for the saline and the BLM-treated mouse.

Sections were analyzed by blinded to the treatment. The extent and the severity of parenchyma infiltration with inflammatory cells and fibrosis were analyzed using a scoring system adapted from the literature [128]. Severity scores were assigned to edema (perivascular, peribronchial, alveolar) and infiltration of inflammatory cells (perivascular,

peribronchial, parenchymal), following the classification: none (score 0), slight (score 1), moderate (score 2), marked (score 3) and severe (score 4). The extent of the lesions was classified based on their percentage distribution as none (0%, score 0) focal (<25%, score 1), multifocal (26-50%, score 2) and diffuse (>51%, score 3). Abnormal histological features were recorded according to their extent and severity (total resultant score being the multiplication of severity and extent scores). Collagen was quantified using "Histolab" (Microvision Instruments, Evry, France). Picrosirius-stained slides were examined with a light microscope (Eclipse E600, Nikon, Egg, Switzerland) connected to a CCD progressive scan video color camera (XCD-U100 CR, Sony, Tokyo, Japan). The whole surface of the median slice of each lung section was captured at x10 magnification. The color corresponding to picrosirius was extracted by threshold setting and the area corresponding to picrosirius staining calculated (Figure 32). Results were expressed as percentage of picrosirius to the total lung surface.

Immunohistochemistry was performed on paraffin sections using the following antibodies for detection of rabbit anti-ionized calcium-binding adapter molecule 1 (IBA-1) expressed by activated macrophages (019741, IBA-1 at 1/500, WAKO Chemicals, Neuss, Germany), goat anti-matrix metalloproteinase (MMP12), secreted by macrophages and involved in the breakdown of extracellular matrix (sc-8839, MMP12 at 1/50, Santa Cruz Biotechnology, Heidelberg, Germany), and rabbit anti-cluster of differentiation 3 (CD3) involved in T cells activation (RM9107S, CD3 at 1/40, Neomarkers, Thermo Fisher Scientific, Basel, Switzerland). The demonstration of these antibodies was carried out using the Ventana immuno-auto-stainer Discovery XT (Ventana, Tucson, Arizona, US), according to programs Nr 69 (IBA1), 779 (MMP12) and 811 (CD3).

For quantification of IBA-1, MMP12 or CD3 on the histological sections, similar analyses were performed as described above for picrosirius determination.

Quantitative real-time polymerase chain reaction (qRT-PCR)

Removed lung tissue was stabilized in RNA later (Ambion, Zug, Switzerland; #AM7021,) and stored at -80°C until use. For RNA purification, samples were transferred to a 2 ml Eppendorf tube with 1000 µl of RLT buffer (Qiagen, Hombrechtikon, Switzerland; #79216) and β-mercaptoethanol (Sigma-Aldrich, Buchs, Switzerland; #M3148) and one stainless bead (Qiagen, #69989). Samples were homogenized (Qiagen Tissue Lyser, #85300) in two to three

1-min runs at 30 rotations/s each, with 1 min on ice between the runs. After centrifugation for 3 min at 13 000 rpm, 4°C, 300 µl of the resulting supernatant were processed on the Rneasy Mini Kit (Qiagen, #74106) with a DNAse digestion step (Qiagen, #79254), accordingly to the manufacturer's protocol.

Resulting total RNAs were quantified on a NanodropTM system (Wilmington, DE, USA) and 1 µg was reverse-transcribed using the high capacity cDNA RT kit (Applied Biosystems, Zug, Switzerland; #4368813).

Expression of the different genes of interest was evaluated by real time PCR using the ABI Prism 7900HT system. Briefly, 10 ng/µl equivalent RNA per well was distributed in a 384 well plates (Applied Biosystems, #4326270), with 5 µl of the Taqman Universal Mastermix 2X kit (Applied Biosystems, #4324020) and 0.5 µl of 20X Assay-on-demand mix Taqman probe (Applied Biosystem, #4331182). The different probes used and respective genes were: Mm00801666_g1 (Col1a1), Mm00483888_m1 (Col1a2), Mm00607939_s1 (Actinβ), Mm00802331_m1 (Col3a1), Mm00500554_m1 (Mmp12), Mm00441724_m1 (TGFb1), Mm01192933_g1 (CTGF), Mm00441818_m1 (Timp1), Mm99999056_m1 (MCP-1), Mm00443113_m1 (MCP-3), Mm99999057_m1 (MIP1-a).

Expression for each sample was normalized to HPRT (Mm03024075 m1) and compared to the vehicle-treated group, using the 2-ΔCT formula. The expression of HPRT was the same in all analyzed groups.

Statistics

Raw (baseline-unsubtracted) MRI data were analyzed using ANOVA with random effects (SYSTAT 12, Systat Software, Inc., San Jose, CA) to take into account the longitudinal structure of the data. For multiple comparisons a Bonferroni correction followed the ANOVA analysis. Histological and qRT-PCR data were analyzed using ANOVA comparisons (Student-Newman-Keul's method). Outliers identified by the Dixon's test (mean±2xstandard deviation) were excluded from the statistical analyses. Mann-Whitney analyses (SYSTAT 11) were performed on histological scores. Significance was considered for $p<0.05$.

Results

Body weight development

The body weight development during the course of the study is summarized in Figure 33. As body weight is an accepted indicator of the well-being of the mice during a challenge and an accurate abortion criterion, five and three BLM-challenged mice belonging respectively to the vehicle and the PT100 group were sacrificed before the end of the study (≥ 20% weight loss with respect to baseline body weight). Vehicle-treated mice were sacrificed at days 5, 7, 8, and 10 (two animals) after last BLM administration. In the PT100 group, animals were sacrificed at days 4, 7, and 8. Weight loss is a known effect of the antibiotic in small rodents [24].

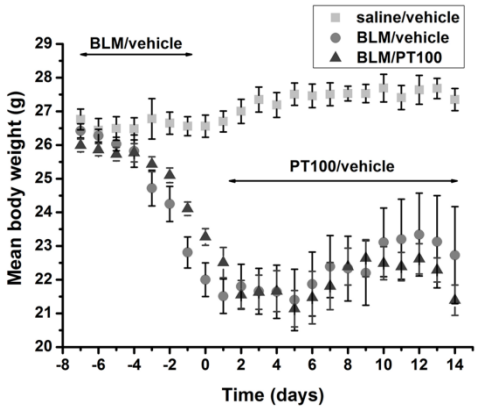

Figure 33: Body weight (means±sem). The initial numbers of animals were 8 in the saline group and 12 in the BLM groups.

Magnetic resonance imaging (MRI)

Figure 34 shows axial MR images from BLM-challenged mice, treated with either vehicle or PT100. With the exception of signals from vessels (dotted arrows), the lung signal was low at baseline, due to the short T2* relaxation time of parenchymal tissue at 4.7 T [129]. Immediately after last BLM dosing (day 0), MRI revealed the presence of lesions throughout the lung (arrows), induced by the antibiotic. For each animal and time point, the total volume of these lesions was quantified from the MR images as described before. The volumes of lesions during the experimental period are shown individually in Figure 35A, while the average volumes for vehicle- or PT100-treated mice are summarized in Figure 35B. Animals were randomized at day 0 according to the BLM-elicited responses detected by MRI, in order to have similar average lesion volumes in the vehicle and the PT100 groups, at the beginning of compound treatment (day 1).

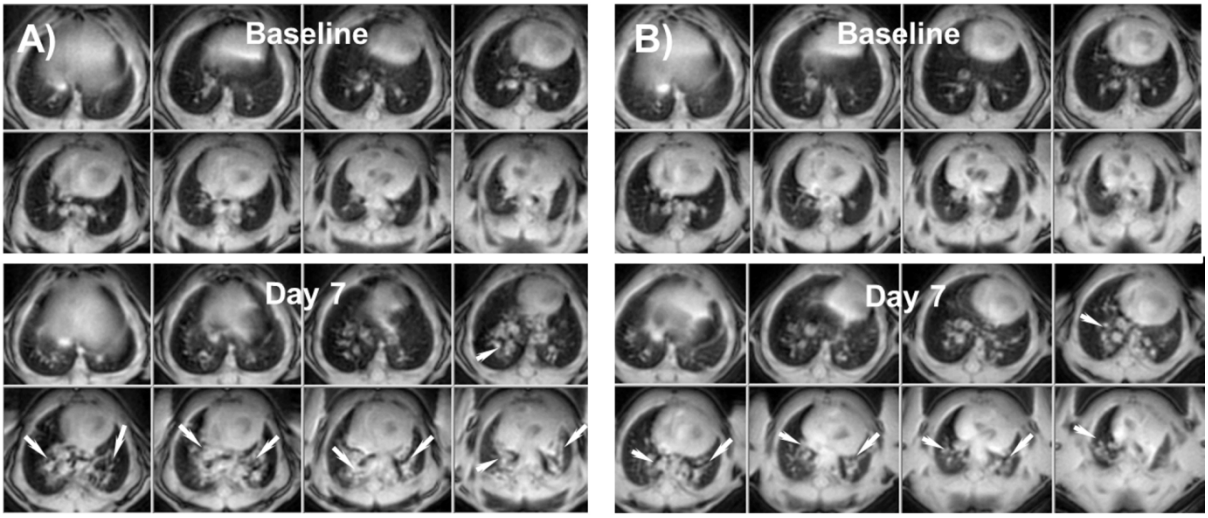

Figure 34: Axial MR images of two mice challenged with BLM and treated with either vehicle (A) or PT100 (B) from day 1 to 14. Day 0 corresponds to the time of last BLM dosing. For each animal, eight images covering the lung are shown per time point. Some lesions induced by BLM are indicated by white arrows. Images were acquired from spontaneously breathing animals. Neither cardiac nor respiratory gating was used.

Histology of cellular infiltration and collagen deposition

Histology at the end of the study revealed neither edema nor perivascular and peribronchial cellular infiltration in lung sections from naive and BLM-treated mice. Slight (score 1), focal (score 1) parenchymal cellular infiltration was detected in 4 out of 8 naive control animals. Moreover, focal to diffuse (scores 1 to 3) and moderate to severe (scores 2-4) parenchymal cellular infiltration was seen in BLM-treated mice. The total scores for parenchymal

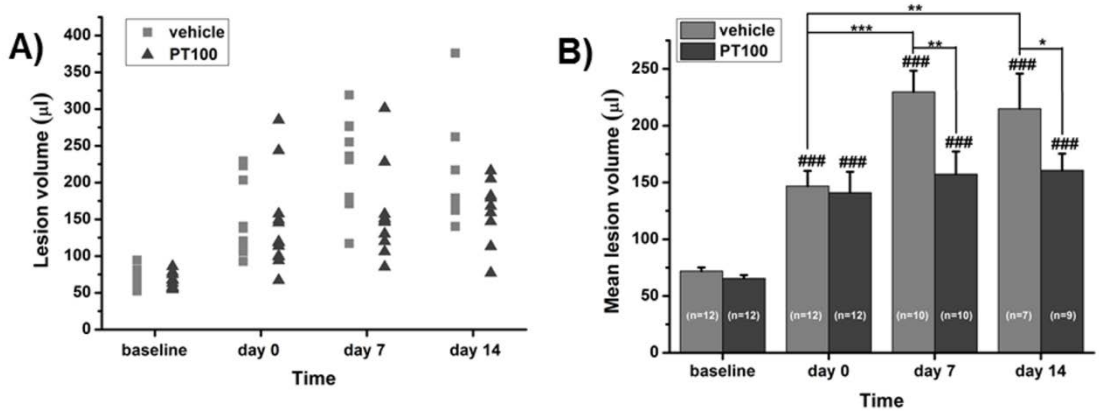

Figure 35: Pulmonary lesion volumes assessed from MR images in BLM-challenged mice. Treatment with compound (or vehicle) has begun at day 1, and continued until the end of the study. A) Individual values for each animal, at the different time points. B) Means±sem for the numbers of animals measured at every time point (indicated in parentheses). Following the acquisition at day 0, animals were randomized in order to have the same mean values in the PT100 and vehicle groups. ### $p<0.001$ indicate Anova comparisons with respect to baseline values, while * $p=0.04$, ** $0.001<p<0.01$, and *** $p<0.001$.

infiltration (multiplication of severity and extent scores) for animals that had received BLM and were treated with either vehicle or PT100 are summarized in Figure 36.

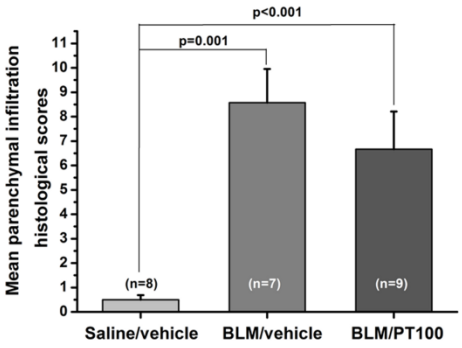

Figure 36: Total histological scores (means±sem) for cellular infiltration comprising the multiplication of severity and extent scores for each mouse. Scores in the groups were compared using Mann-Whitney analyses.

The mean collagen content assessed in picrosirius-stained slices at day 14 after last vehicle or BLM challenge is summarized in Figure 37A. Significant correlation was seen between the volumes of BLM-induced lesions detected *in vivo* by MRI and the collagen content determined histologically in the lungs of the same animals (Figure 37B). Both MRI and histological observations suggest a reduced BLM-induced response in the lungs of PT100 - compared to vehicle-treated mice.

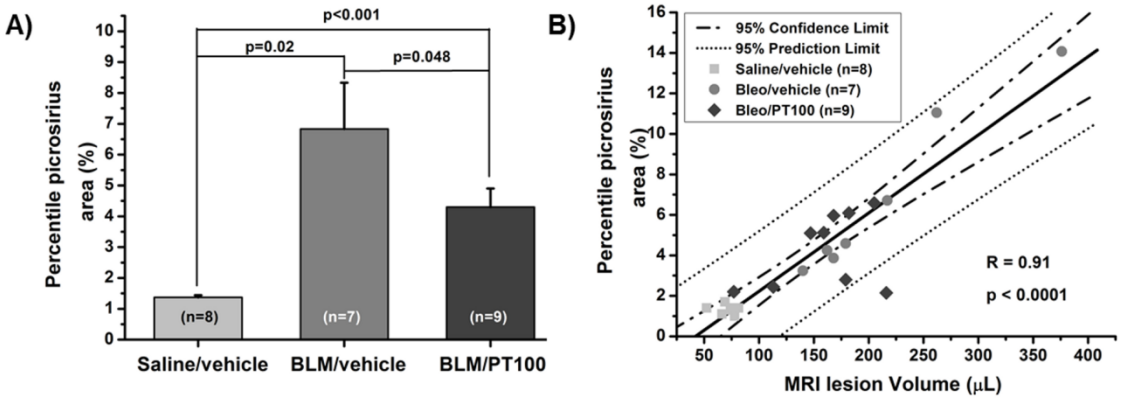

Figure 37: Quantification of collagen content in picrosirius-stained slices at day 14 after last saline or BLM administration. (a) Picrosirius areas reflecting collagen deposition are given as means (± sem) for the numbers of mice provided in parentheses. Levels of significance correspond to Anova comparisons (Student-Neuman-Keuls tests). (b) Correlations between the lesion volumes assessed in vivo by MRI and the collagen content determined in histological sections.

Quantitative real-time polymerase chain reaction (qRT-PCR)

To determine the relative messenger RNA (mRNA) expression level of several markers in the lung fibrosis model, qRT-PCR on lung tissue was performed 14 days after the multiple administration of either saline or BLM. The following markers were chosen because of their

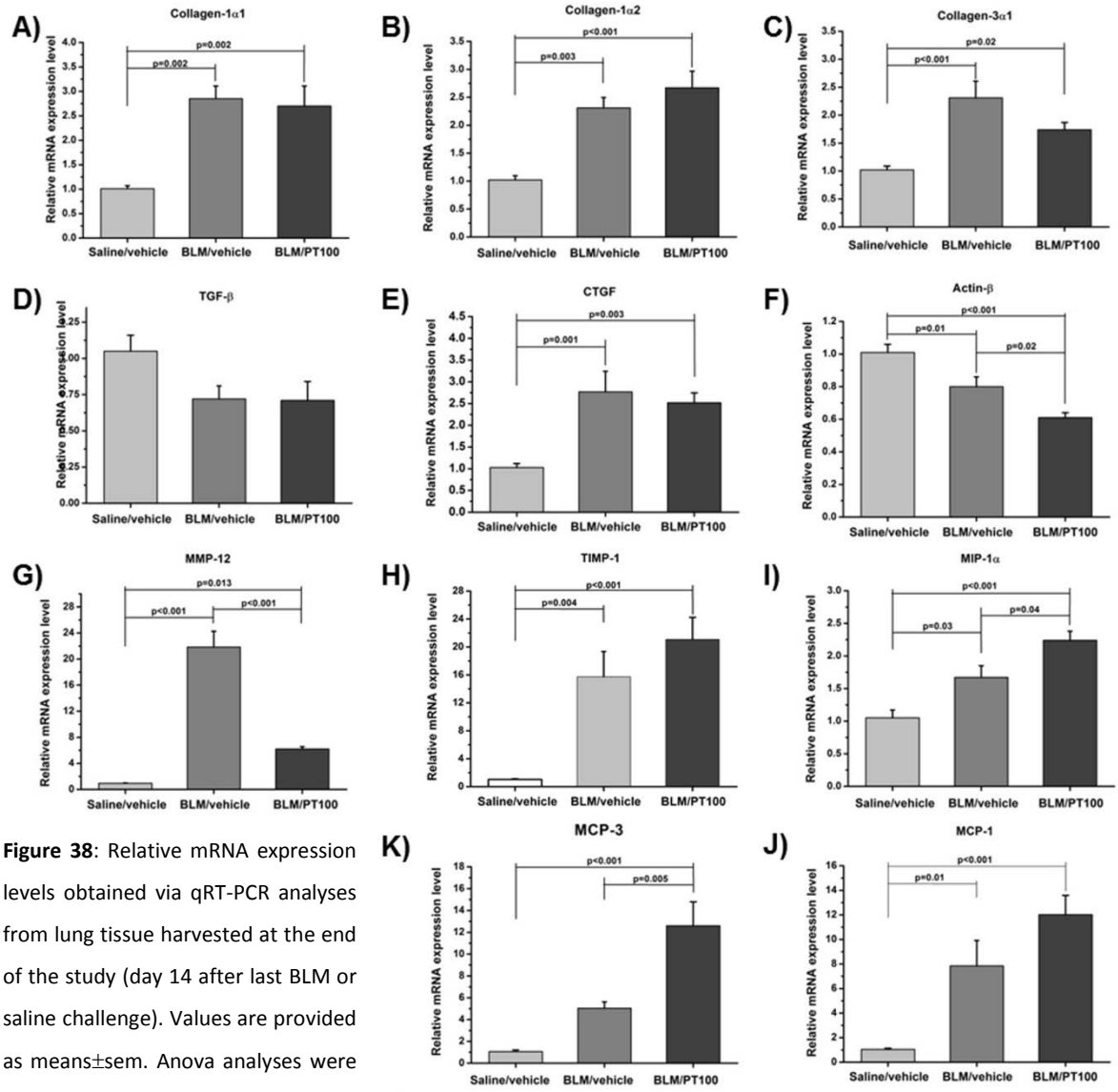

Figure 38: Relative mRNA expression levels obtained via qRT-PCR analyses from lung tissue harvested at the end of the study (day 14 after last BLM or saline challenge). Values are provided as means±sem. Anova analyses were performed using Student-Newman-Keuls tests.

relationships to fibrosis development: collagen-1α1, -1α2, and -3α1, TGF-β1 (one of the main profibrogenic cytokines involved in the pathogenesis of lung fibrosis, which induces fibroblast differentiation into myofibroblasts and produce high levels of collagen), connective tissue growth factor (CTGF; widely thought to promote the development of fibrosis in collaboration with TGF-β; cooperative interactions between CTGF and TGF-β signaling are required to elicit overt tissue fibrosis); actin-β, MMP-12 (mice deficient in MMP-12 have reduced fibrosis in the model of interleukin-13 dependent pulmonary fibrosis induced by challenge with S. Mansoni eggs [130]), tissue inhibitor of metalloproteinases (TIMP-1; upregulated during fibrosis [131]), macrophage inflammatory protein (MIP)-1α, and

monocyte chemotactic protein (MCP)-1 and -3. Significant differences were found in the actin-β, MMP-12, MIP-1α, and MCP-3 mRNA expression levels in the lungs of PT100- compared to vehicle-treated mice (Figure 38). There were significant correlations between the relative mRNA expression levels of collagen-1α1 (R=0.8, p<0.001), -1α2 (R=0.75, p<0.001), -3α1 (R=0.81, p<0.001) and histologically-determined collagen content (picrosirius staining).

Histology of macrophages

The reduced mRNA expression for MMP-12 [a marker of macrophages [132] and increased mRNA expression for MIP-1α and MCP-3 in the BLM/PT100 as compared to the BLM/vehicle group suggested an implication of macrophages in the mechanism of action of the compound.

Immunohistochemical analyses at day 14 after last saline or BLM administration revealed that MMP-12 (a macrophage marker), IBA-1 (a macrophage activation marker) and CD3+ (a marker for T lymphocytes) were significantly increased in BLM- compared to saline-challenged mice (Figure 39). Moreover, IBA-1 was significantly increased in compound X-treated animals, suggesting an increased number of activated macrophages in this group.

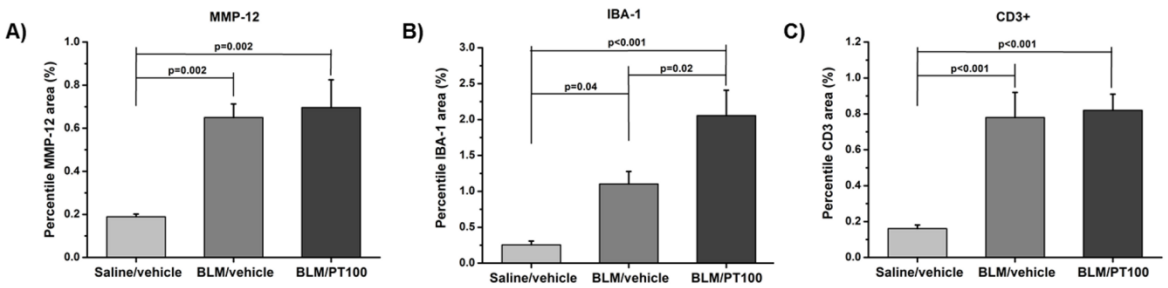

Figure 39: Quantification of MMP-12, IBA-1 and CD3+ (means± sem) in histological slices at day 14 after last saline or BLM administration. Levels of significance correspond to ANOVA comparisons (Student-Neuman-Keuls tests).

Discussion

In the present work the effects of the FAP inhibitor, PT100, in the lungs of BLM-challenged C57BL/6 mice were assessed longitudinally with proton MRI. Measurements were performed on spontaneously breathing animals using a short echo time UTE sequence. No contrast agent

was injected for the imaging procedure. At the end of the study, histological and qRT-PCR analyses were performed to further characterize the responses.

In an earlier study concerning the same animal model, we had shown that BLM administered repeatedly in the nostrils of male C57BL/6 mice elicited a lasting response detected by MRI up to day 70 after dosing [70]. Histology revealed early fibrotic foci within the inflammatory areas at day 7 after repeated BLM dosing. This is consistent with evidence from the literature suggesting that the major fibro-proliferative phase induced by BLM in rats and mice occurs within the first week following its administration and that this process co-exists with inflammation. Histology also showed that from day 14 onwards fibrosis was the predominant component of the response elicited in the lungs of male mice by repeated BLM. Overall, those data indicated that repeated BLM administration leads to consistent and sustained fibrosis formation with moderate initial inflammation [70].

As evidenced longitudinally by MRI in the present study, the lesions induced by BLM in the lungs of vehicle-treated mice progressed over time. In contrast, the responses elicited by BLM did not progress in animals receiving PT100. Histology at the end of the study demonstrated significant less fibrosis in PT100- than in vehicle-treated, BLM-challenged mice. These observations suggest that PT100 administered therapeutically had an anti-fibro-proliferative effect.

Significant differences in the actin-β, MMP-12, MIP-1α, and MCP-3 mRNA expression levels in the lungs of PT100- compared to vehicle-treated mice were revealed by qRT-PCR analyses. There were significant correlations between the relative mRNA expression levels of collagen-1α1, -1α2, -3α1 and histologically-determined collagen content (picrosirius staining).

Contrary to qRT-PCR, immunohistochemistry did not show differences in MMP-12 between the vehicle and PT100 treatment groups. Nonetheless, we consider these two approaches as equally informative and complementary. One reflects an average level of transcriptional activity for the gene of interest while the other addresses protein localization, with possible bias such as time lag for mRNA profiles to be translated into protein, or possible regulatory mechanisms at the translational level resulting in no protein. Therefore, follow up studies aiming at an in-depth characterization of the different molecular events and related kinetics

by microarray, western blotting and immunohistochemistry would result in a better understanding of the bleomycin induced lung injury model and PT100 effect.

Of note, however, was the fact that the IBA-1 level determined histologically was higher in the lungs of PT100 - compared to vehicle-treated mice. Taken together, these observations suggest that therapeutic treatment with PT100 had an effect on the number of activated macrophages with no effect on the activation of fibroblasts.

To date, several hundreds of compounds were identified in various models of experimental pulmonary fibrosis and proposed to have therapeutic potential for IPF [133]. However, only a small number have reached clinical trials and very few have been assessed in a therapeutic setting [133,134]. The vast majority of compounds that were examined in drug intervention studies in experimental pulmonary fibrosis are only successful in a preventive or prophylactic setting, which means they are given with or prior to administration of the fibrogenic stimulus [133]. Intervention studies in models of fibrosis could be more meaningful if the compound was administered in the fibrotic phase of the disease and not as prevention. As illustrated here, imaging may significantly support such studies, by enabling longitudinal assessments in the same animal. Moreover, randomization of animals at the beginning of treatment may assist drug testing, as BLM elicits rather variable responses in the lungs.

Manuscript:

5.2) "Therapeutic Effect of Pasireotide on Bleomycin-Induced Lung Injuries in Rats - Detection by MRI and *post-mortem* analysis"

Christine Egger[1,3], Catherine Cannet[1], Christelle Gérard[1], Ramona Rebmann[2] , Andrew Dunbar[1], Bruno Tigani[1], Herbert Schmid[2], Nicolau Beckmann[1,#]

Novartis Institutes for BioMedical Research, [1]Global Imaging Group, CH-4056 Basel, Switzerland, [2]Oncology, CH-4056 Basel, Switzerland; and [3]University of Basel, Biocenter, CH-4056 Basel, Switzerland.

Introduction

Pulmonary fibrosis is a lethal disease with often unknown cause (IPF) [21], characterized by fibroblast proliferation and extracellular remodeling (such as collagen and elastin deposition), thickening of alveolar walls, and infiltration of inflammatory cells [22-27]. Remodeling leads to an increased resistance of the lung tissue and therewith an increased compliance, which means a serious loss of organ function for the patients. To date no treatment against pulmonary is available and the limited numbers of *in vivo* readouts is challenging the pharmaceutical research.

The availability of the bleomycin model of pulmonary fibrosis provides the opportunity to investigate in small rodents novel pharmacological approaches aiming to treat this crippling disease. Bleomycin is an antibiotic with activity against gram-negative bacteria [32] that possesses chemotherapeutic properties and is highly efficient in some types of carcinomas. In spite of these therapeutic characteristics, bleomycin may produce a dose-dependent pulmonary fibrosis in a significant portion of patients [21]. Therefore, single [33-35] or multiple [36] instillations of bleomycin is commonly used to induce experimental pulmonary fibrosis in small rodents. Application of the antibiotic causes an acute inflammatory reaction and fibrotic changes that resemble human fibrotic lung disease both histologically and physiologically [22,39].

Somatostatin (sst) has been shown to be upregulated in human fibrotic lungs [135] and in the mouse bleoymycin model [136]. Thus, interest raised whether sst analogues may provide a potential therapy against pulmonary fibrosis. Indeed, a few sst analogues have shown antifibrotic activities *in vitro* and *in vivo* [137]. The somatostatin analogue, pasireotide (SOM230), binds to four out of five sst receptors (sst1, sst2A, sst3, and sst5) and is in use for treatment of Cushing's disease. SOM230 attenuated pulmonary fibrosis in a mouse bleomycin model [136].

Recently we reported the use of MRI to non-invasively follow the course of lung injury induced by repeated administration of bleomycin to mice [70,120], or of single or repeated bleomycin administration to rats [27]. In the present work this model of lung fibrosis has been used to investigate a therapeutic effect of SOM230 on established pulmonary fibrosis in rats. The

responses in the lungs detected *in vivo* by MRI have been compared to *post-mortem* hydroxyproline and lung dry and wet weight determination.

Material and Methods

Ethics Statement

Experiments were carried out with the approval of the Veterinary Authority of the City of Basel (license number BS-2565).

Animals

Seven- to 9-week-old Sprague Dawley (SD) rats (n=69) (Elevage Janvier, Saint Berthevin, France) were used throughout the study. The presented data were collected in two independent studies (n=33 and n=36) with the same protocol regarding bleomycin challenge, SOM230 treatment, and necropsy. Animals were kept at an ambient temperature of 22 ± 2°C under a 12 h normal phase light-dark cycle and fed NAFAG® pellets (Nahr- und Futtermittel AG, Gossau, Switzerland). Drinking water and food were freely available.

Oropharyngeal aspiration of bleomycin or saline

Animals were lightly anesthetized with 3.5% isoflurane delivered in a box and bleomycin hydrochloride (3.0 mg/kg) in 100 µl of saline (0.9%) or vehicle (100 µl of saline (0.9%)) were administered via oropharyngeal aspiration (OA) using a micropipette. OA was performed as described by de Vooght et al. [68]. Rats were fixed on a surgery board, the tongue was pulled out with a forceps, and the liquid was placed onto the distal part of the oropharynx while the nose was gently closed.

Injection of SOM230-LAR

SOM230 in a long acting release (LAR) formulation (8 or 80mg/kg) was injected sub-cutaneously (s.c.) in the neck of the animals, nine days after bleomycin challenge with an injection volume of 1 mL/kg for 8 mg/kg and 2 mL/kg for 80mg/kg administration. Rats were randomized into groups according to the bleomycin-induced responses detected by MRI at

day 8, in order to have the same mean lesion and lung volumes in all treatment groups at the beginning of compound dosing.

Magnetic resonance imaging (MRI)

During MRI signal acquisitions, animals were placed in prone position in a cradle made of Plexiglas. Body temperature was kept at 37±1°C using warm water flowing through the cradle. Following a short period of introduction in a box, anesthesia was maintained with 1.5-2% isoflurane in a mixture of O_2/N_2O (1:2), administered via a nose cone. All measurements were performed on spontaneously breathing animals; breathing rate was monitored and kept at approximately 60 breaths per minute. Averaging over several respiratory cycles suppressed artifacts caused by movements of the chest and the heart without the necessity of triggering the data acquisition [70,72]. As mentioned before, the presented data were collected in two independent studies using either a 47/40 or a Biospec 70/30 spectrometer (Bruker Medical Systems, Ettlingen, Germany) operating at 4.7 or 7.0 T, respectively. The operational software of the scanner was Paravision (Bruker). Two- and three-dimensional UTE sequences were used at 4.7 and 7.0 T, respectively. The following parameters were applied for the detection of bleomycin-induced lung injury and total lung volume in rats: 2D-UTE: TR 15.0 ms, TE 801 µs, 604 projections, 2 averages, flip angle of the excitation pulse 25°, matrix size 192x192, slice thickness 1.5 mm and FOV 6.0 x 6.0 cm^2. The total acquisition time was of 7.25 min for 24 consecutive axial slices covering the entire lung. A birdcage resonator of 70 mm diameter was used for excitation and detection. 3D-UTE: TR 2.7 ms, TE 20 µs, 51360 projections, 5 averages, band width 64 kHz, flip angle of the excitation pulse 2°, matrix size 128x128x128, and FOV 5.0 x 5.0 x 7.0 cm^3. The total acquisition time was of 11.5 min for the FOV covering the entire lung. A birdcage resonator of 86 mm diameter was used for excitation and detection.

MR image analysis – Volume of lung lesions

At a given time point, the area of bleomycin-induced lesions was quantified on each image from the dataset covering the whole lung, using a semi-automatic segmentation procedure implemented in the IDL (Interactive Data Language Research Systems, Boulder, Colorado, USA) environment on a Linux system. Images were first low-pass-filtered with a Gaussian profile filter and then transformed into a set of four grey level classes using adaptive Lloyd-

Max histogram quantitation. The highest class in the transformed images was extracted interactively by a region grower, whose border was drawn manually on each slice to control the growing and limit it to areas within the lung (Figure 12). For each image, the area thus segmented by region growing corresponded to high intensity signals in the lung. The total volume of high intensity signals was then calculated by adding the areas obtained for each image from the dataset, and multiplying the summed value by the slice thickness. Segmentation parameters were the same for all analyzed images.

MR image analysis – Total Lung Volume

To evaluate lung volumes (which is defined for this work as total volume of the lung, including tissue, air, and airways), regions of interest (ROI) have been manually drawn around the lung on each acquired slice using the software Paravision (Figure 40). The calculated areas of all ROIs for one animal have been added and multiplied by the slice thickness, resulting in the total lung volume.

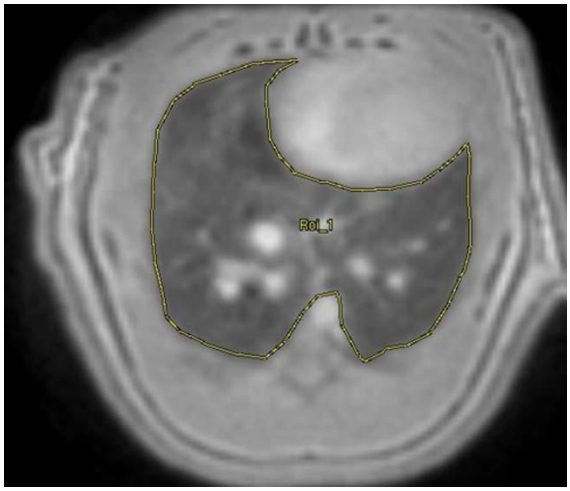

Figure 40: Evaluation of total lung volume. ROI (yellow line) was manually drawn around the lung on each acquired slice.

Post-mortem analyses

Animals were sacrificed with an overdose of thiopental (Pentothal®, Abbott; 250 mg/kg (i.p.)) 24 h after last MRI acquisition. The trachea and left bronchus were immediately ligated to avoid collapse of the lung. Following the organ's removal, the left lobe was stored for later histological analyses, while the two right lobes were employed for the determination of hydroxyproline content. The other two right lobes were stored for later qRT-PCR analyses.

Determination of hydroxyproline in lung tissue samples

Lung tissue samples were weighed, dried in an oven at 90°C overnight, and the weight was recorded again. Dry tissues were then boiled in 0.5 mL of 6 M HCl at 120°C overnight (8-16 h) in Pyrex tubes with heat- and acid-resistant screw-on caps (article TES-830-70G; Fisher Scientific, Wohlen, Switzerland). After cooling down and adding 5 µL of phenolphthalein (1%),

the samples were neutralized with NaOH 10 M (Sigma N°S-5881) and 6 M HCl. Black precipitate and brown color was removed by adding 100 µL of carbon suspension [10 mg/mL activated charcoal (article C4386; Sigma-Aldrich, Buchs, Switzerland) in water], centrifugation, and filtration. Five microliters of standard or hydrolyzed sample were pipetted in triplicate onto a 96 well plate, and 5 µL citrate acetate buffer (5% citric acid, 7.2% sodium acetate, 3.4% sodium hydroxide, 1.2% glacial acetic acid, distilled water) was added to each well, as well as 100 µL of freshly prepared chloramine-T solution (14.1mg chloramine-T, 0.1mL n-propanol, 0.1mL distilled water, 0.8mL citrate acetate buffer). The samples were then incubated at room temperature for 20 minutes. After adding 100 µL of Ehrlich's reagent (2.5 g of 4-(dimethylamino)benzaldehyde, 9.3 mL of n-propanol, and 3.9 mL of 70% perchloric acid), the wells were incubated for 20 minutes at 65°C. After cooling down, the samples were measured at 550 nm on a spectrophotometer (SpectraMax 340PC, Molecular Devices, Sunnyvale, CA, USA); a standard curve from 5 to 100 mg hydroxyproline in water was created. Data were expressed as µg/right lung lobe.

Statistics

For statistical analysis the software SigmaPlot™ (Systat Software Inc., San Jose, CA, USA) has been used. One-way ANOVA and Tukey tests have been performed for endpoint readouts while ANOVA with random effects and Tukey or Fisher tests have been used for readouts with multiple measurements to take into account the longitudinal structure of the data. The following abbreviations were used for the indication of significance: */#: $0.01<p<0.05$; **/##: $0.001\leq p \leq 0.01$ ***/ ###: $p< 0.001$.

Results

SOM230 reduced MRI-detected, bleomycin-induced lung injuries and total lung volume

Oropharyngeal aspiration of 3mg/kg bleomycin in SD rats induced lung lesions, which could be detected by 2D and 3D UTE-MRI in two separate experiments (Figure 41 A-B). Starting at nine days after bleomycin challenge, two groups have been treated with either 8 or 80 mg/kg SOM230 LAR. Already one week after injection of SOM230, MRI signals significantly decreased

in both groups, compared to bleomycin-challenged animals without treatment. Note that the volumes of signals quantified using the 3D-UTE sequence were systematically higher than those quantified with 2D-UTE. This difference can be explained by a difference in sensitive between both approaches (see Discussion). Representative images of bleomycin- and saline-challenged lungs at day 8 (before begin of SOM230 treatment) and day 20 (end of the study) are shown in Figure 42 and 43. The lesion volume, relative to the treatment begin (day 9, both studies combined) is shown in Figure 44. In this figure, relative signal volumes were provided because of the systematic differences in signal volumes due to differences in sensitivity between the 2D- and 3D-UTE acquisitions. SOM230 reduced, in a not dose-dependent way, bleomycin-induced lung injuries, while both control groups showed no changes in MRI lesion volume.

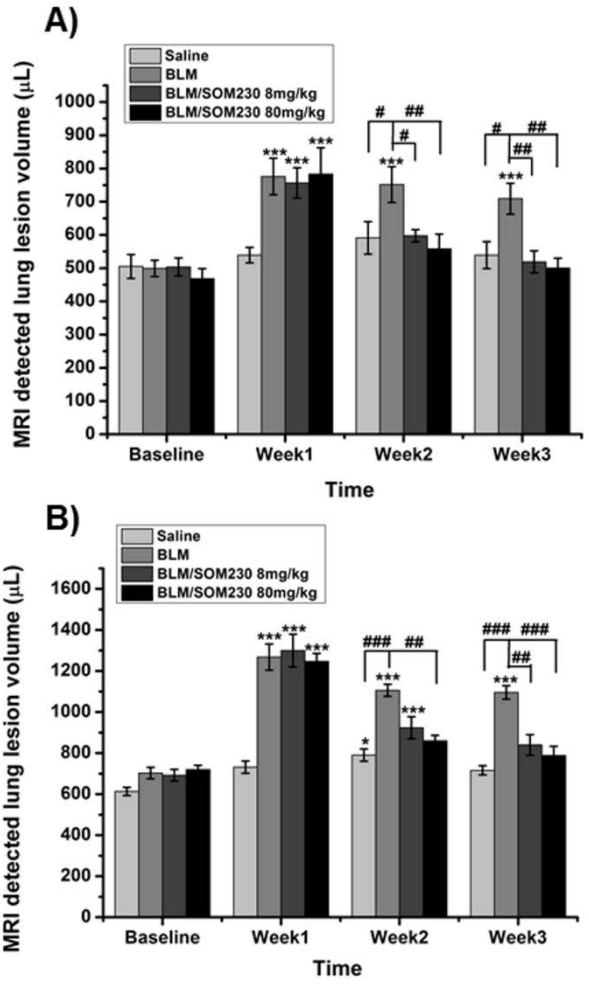

Figure 41: MRI detected lung lesion volume in saline- and BLM treated rats, before and after SOM230 treatment in two separate experiments. A) Experiment 1: Lesion volume evaluated on images acquired by 2D-UTE. Number of animals were n=6 for saline and n=9 for all other groups. B) Experiment 2: Lesion volume evaluated on images acquired by 3D-UTE. Number of animals were n=9 all groups. . The statistical significance values ***p<0.001 *p<0.5 indicate comparison to baseline

As discussed in Chapter 4.3 ("MRI-detected lung volume as a noninvasive readout for tissue deposition in the rat bleomycin model of pulmonary fibrosis"), MRI detected an increased total lung volume in the rat bleomycin model, with a correlation to wet and dry weight of the lungs. Since MRI-detected total lung volume reflects the effect of tissue deposition in the bleomycin model for pulmonary fibrosis (see chapter mentioned before), total lung volumes have been determined for all groups and time points and are presented in Figure 45. One week after bleomycin challenge, total lung volume was increased in all bleomycin groups, compared

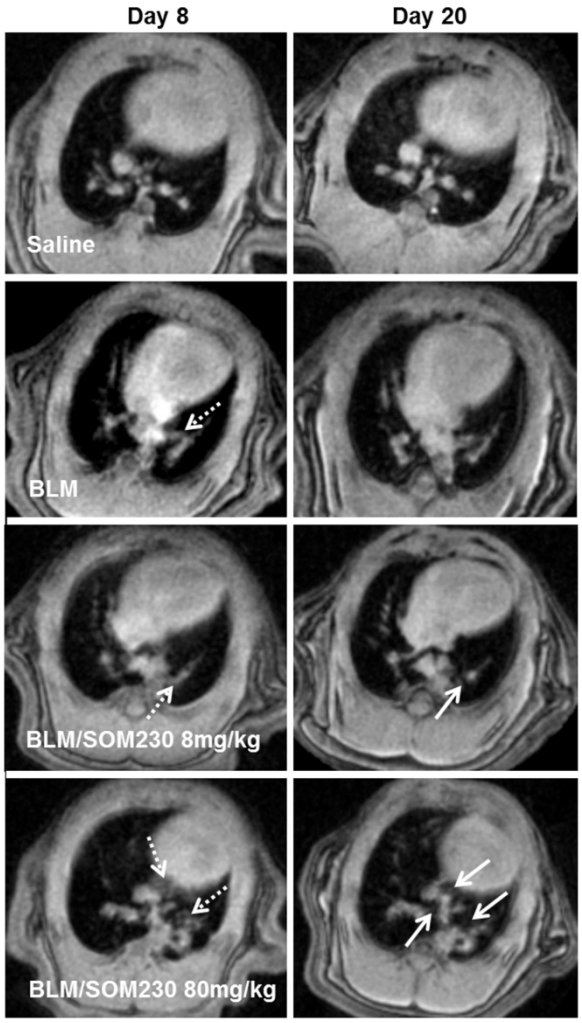

Figure 42: Representative images acquired by 2D-UTE MRI showing one animal per group at two different time points. Images on the left side have been acquired 8 days after BLM- or saline-challenge, before SOM230 treatment. Images on the right side have been acquired at the end of the study. Dotted arrows on the left side point to bleomycin-induced lesions. Arrows on the right side point to areas where lesions were resolved.

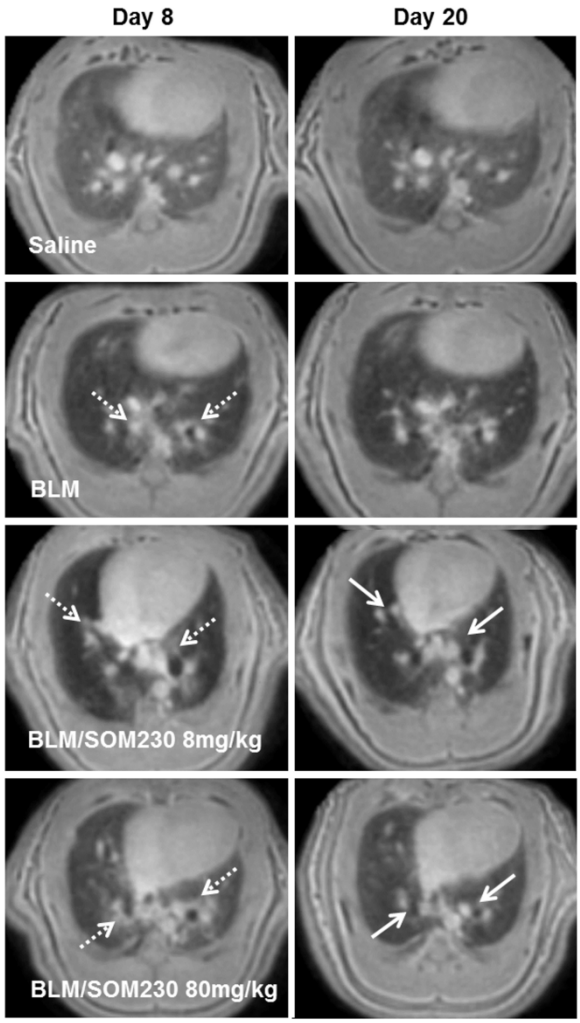

Figure 43: Representative images acquired by 3D-UTE MRI showing one animal per group at two different time points. Images on the left side have been acquired 8 days after BLM- or saline-challenge, before SOM230 treatment. Images on the right side have been acquired at the end of the study. Dotted arrows on the left side point to bleomycin-induced lesions. Arrows on the right side point to areas where lesions were resolved.

to saline group. After injection of SOM230, lung volumes in both SOM230 groups stagnated and/or even slightly decreased, while the lung volumes of both control groups further increased between days 8 and 20. At the end of the study, two weeks after injection of SOM230, the lung volumes of rats treated with 8 or 80mg/kg SOM230 did not differ from those of saline-treated, healthy animals, while lung volumes in rats belonging to the bleomycin control group were still significantly increased, compared to all three other groups.

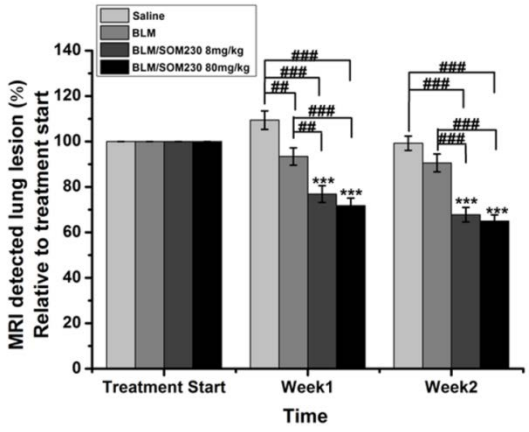

Figure 44 Effect of SOM230 on MRI-detected, BLM-induced lung lesions. Data are presented relative to lung lesion volume eight days after challenge, before injection of SOM230. The statistical significance values ***p<0.001 indicate comparison to "Treatment start".

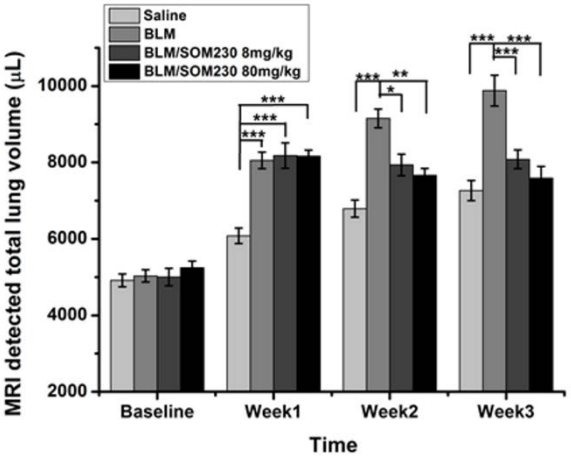

Figure 45: MRI detected total lung volume in saline- and BLM-treated rats, before and after SOM230 treatment. A) Lung volume was evaluated on images acquired by 2D- and 3D UTE MRI. Number of animals was n=15 for saline and n=18 for all other groups.

SOM230 treated and bleomycin-challenged rats showed no difference in lung wet and dry weight compared to saline-group

After the last MRI session, all animals have been sacrificed at day 21 after bleomycin- or saline-challenge and two right lung lobes (caudal and cranial) have been weighed and dried for hydroxyproline determination. Wet and dry weight of these two lung lobes are presented in Figure 46. Bleomycin-challenged rats showed increased values of lung wet and dry weight, compared to all other groups. There was no significant difference observable between saline-challenged and bleomycin/SOM230-treated animals, and no difference between the two SOM230 groups. The relative water content was 78.6-79.6% for all three groups with no significant difference.

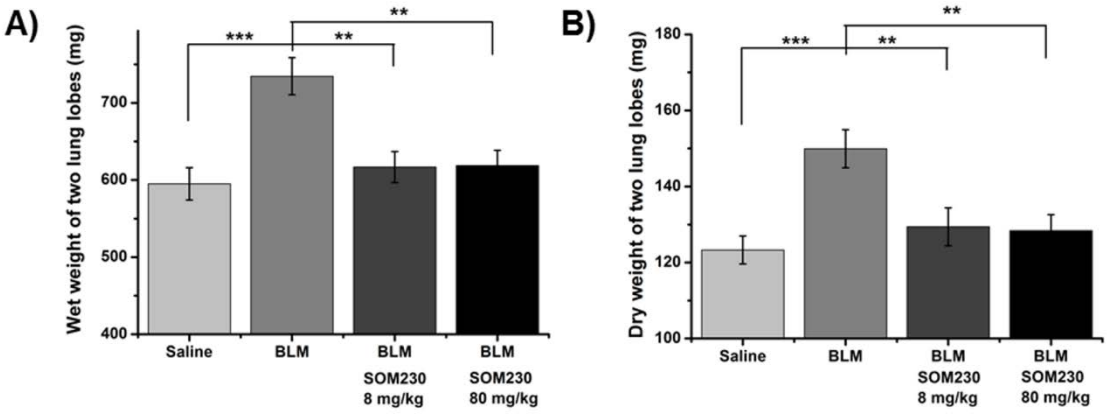

Figure 46 Wet weight (A) and dry weight (B) of two right lung lobes removed from SOM230- and untreated SD rats, 21 days after BLM- or saline-challenge. Number of animals was n=15 for saline- and n=18 for all BLM-groups.

Correlation

To confirm MRI-detected total lung volume as a readout for tissue deposition, correlation between lung volume and lung dry weight has been calculated (Figure 47). A strong correlation between the two readouts could be observed.

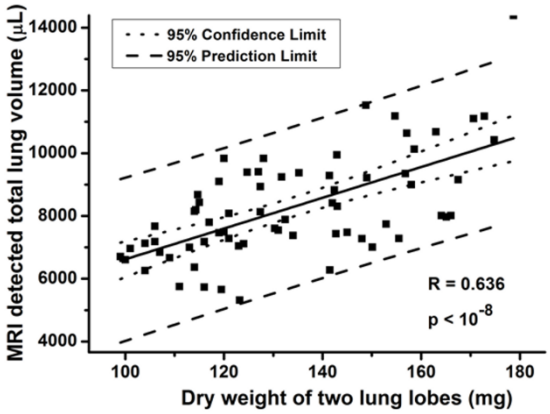

Figure 47 Correlation between MRI-detected total lung volume and dry weight of two lung lobes. Number of samples was n=69.

Hydroxyproline content

Hydroxyproline content of two right lung lobes was determined as described earlier, 21 days after saline- or BLM-challenge. BLM-challenged rats showed a significantly higher lung hydroxyproline content compared to saline group (Figure 48). Hydroxyproline content was also increased in the lungs of SOM230-treated animals, but the values of both SOM230 groups were slightly lower than in the BLM group (Figure 48).

Discussion

To date, only a small number of compounds, suggested to have antifibrotic effect on pulmonary fibrosis, have reached clinical trials [133,134]. Most of them have been assessed in preventive or prophylactic settings [133,134]. However, assessing the effects of on established fibrosis is more meaningful. In this work the therapeutic effect of SOM230, a somatostatin analogue, on bleomycin-induced pulmonary fibrosis has been investigated. MRI served as a non-invasive *in vivo* readout and was confirmed by several *post-mortem* analysis.

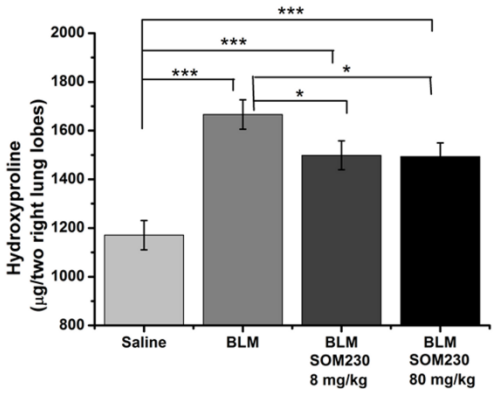

Figure 48 Hydroxyproline content in two right lung lobes of un- and SOM230-treated SD rats, 21 days after saline- or bleomycin-challenge. For statistical analysis, one-way ANOVA and Fisher-Test have been applied.

The injection of two different doses of SOM230 LAR (8 and 80 mg/kg) led to a reduction of MRI-detected bleomycin-induced lung injuries in two independent studies. In the second study, baseline values and bleomycin-induced increase were slightly higher than in the first study. Since both studies were performed following exactly the same treatment protocol, the differences in absolute MRI signal values can be explained by use of two different MRI techniques. For the second study a 7.0 T magnet has been used and a 3D UTE sequence was applied. Since this sequence allows the detection of a 3D volume without slice selection, more signal, especially from the lung parenchyma, could be detected compared to the 2D acquisition (for comparison between images acquired by 2D- and 3D-UTE see Figures 42 and 43). Moreover, a significantly shorter TE was obtained using the 3D-UTE sequence (20 µs compared to 800 µs in the 2D-UTE sequence), which also contributed to the enhanced sensitivity. Nonetheless, in both studies SOM230 significantly reduced the detected injuries, relative to treatment start, in a comparable manner.

Additionally to lung lesion volume, total lung volume has been evaluated. SOM230 stopped the bleomycin-induced increase of MRI-detected total lung volume in such a way that, at the end of the study, no difference was found between the saline and both SOM230 groups. The

results of lung wet weight, dry weight confirmed that observation. No differences between the BLM/SOM230- and saline-treated animals could be observed, while the values in the BLM-challenged control group were significantly increased. The presence of lung edema may be excluded, since the relative water content of the lungs was in the same range, in all four groups. SOM230 slightly decreased the lung hydroxyproline content, compared to BLM group, but the values of both SOM230 groups were still significantly higher than in the saline group. These data let suggest, that hydroxyproline that has been deposited during the first nine days, before begin of SOM230 treatment, could not completely be removed.

Overall, the presented data let suggest that SOM230 reduced the bleomycin-induced tissue deposition, in a not dose-dependent manner. Twenty and one days after injection of SOM230, no readout, except hydroxyproline, showed a difference between saline- and BLM/SOM230-treated animals. The question whether SOM230 actually healed bleomycin-induced lung fibrosis, has to be answered by histological analysis. As discussed earlier (see chapter “MRI-detected lung volume as a noninvasive readout for tissue deposition in the rat bleomycin model of pulmonary fibrosis”), the bleomycin-induced increase in total lung volume reflects a change in lung mechanics. The fact that the lung volumes in bleomycin-challenged rats treated with SOM230 were decreased, compared to control groups, suggests that the sst analogue may have a positive impact on the lung function.

Since SOM230’s mechanism of action is not completely understood, further analyses have to be performed. Gene expression of Col1α1, Col3α1, TGF-β, TNF-α and all five sstr will be determined in lung tissue samples and several biomarkers for inflammation and fibrosis will be measured in blood serum and plasma, taken before the euthanasia of the animals at the end of the study.

6) Imaging of Renal Fibrosis by MRI: Perfusion, Renal Clearance, and Macrophage Visualization

6.1) Manuscript: "Adriamycin-Induced Nephropathy in Rats: Functional and Cellular Effects Characterized by MRI"

Christine Egger[1], Catherine Cannet[1], Christelle Gérard[1], Corinne Debon[2], Nadine Stohler[2], Andrew Dunbar[1], Bruno Tigani[1], Jianping Li[2], Nicolau Beckmann[1,*]

Novartis Institutes for BioMedical Research, [1]Global Imaging Group and
[2]Autoimmune Diseases Department, CH-4056 Basel - Switzerland

Introduction

Adriamycin (doxorubicin, Pfizer) is licensed for the treatment of different cancers, such as breast cancer, lung cancer, and ovarian cancer. The medication works by binding to DNA in cells, altering the shape of the DNA and killing the cells. While adriamycin can kill healthy and cancerous cells, it has a greater effect on cancerous cells because they multiply more rapidly. Adriamycin is a well-known inducer of renal injury in rodents, which mirrors that seen in human chronic kidney disease due to primary focal segmental glomerulosclerosis [45-47]. Adriamycin-induced nephropathy has enabled a greater understanding of the processes underlying the progression of chronic proteinuric renal disease [48,49]. The model is characterized by podocyte injury followed by glomerulosclerosis, tubulointerstitial inflammation and fibrosis. Adriamycin-induced renal injury has been shown in numerous studies to be modulated by both non-immune and immune factors, thus facilitating mechanistic studies of tubulointerstitial injury [47,138].

In the present work, MRI techniques have been used to non-invasively characterize kidney anatomy and function in a rat model of adriamycin-induced nephropathy. Renal function has been analyzed with a dynamic contrast enhanced (DCE) technique as reported earlier by Baumann and Rudin [139] and Laurent et al. [140]. The approach is based on the fact that Gd chelates are small particles similar to inulin that are first disseminated to the vascular space after the intra-venous (i.v.) administration and then pass through the extracellular space and are freely filtered from the glomeruli. Kidney perfusion was assessed by the i.v. injection of an extravascular, SPIO contrast agent. As SPIO nanoparticles are removed from the circulation by cells from the mononuclear phagocyte system via adsorptive endocytosis [141] in a process mediated by the monocyte integrin Mac-1 receptor [142], anatomical images were acquired 24 h after SPIO administration with the aim of detecting the infiltration of macrophages into diseased kidneys. This property of SPIO nanoparticles has been exploited extensively to track *in vivo* by MRI macrophage infiltration into inflamed areas in several disease areas, ranging from atherosclerosis, stroke and myocardial infarction to solid organ transplantation (see [143,144] for reviews). Finally, in addition to MRI evaluations, the glomerular filtration rate (GFR) has been assessed biochemically, and histological as well as hydroxyproline analyses have been performed at the end of the study.

It has been demonstrated earlier that 1D11, in particular in combination with angiotensin II blockade, had antifibrotic effects in models of glomerulonephritis [42,145,146]. In those studies, the antibody was administered preventatively, before onset on injury. In this study, 1D11 has been administered after the induction of nephropathy to investigate a potential therapeutic effect of the antibody.

Materials and Methods

Experiments were carried out with the approval of the Veterinary Authority of the City of Basel (license BS-2353).

Animals

Male Wistar rats (n=26) (Elevage Janvier, Saint Berthevin, France) weighing approximately 270 g at the beginning of the study were used. Animals were kept at an ambient temperature of 22 ± 2°C under a 12 h normal phase light-dark cycle and fed NAFAG® pellets (Nahr- und Futtermittel AG, Gossau, Switzerland). Drinking water and food were freely available. Three groups of rats were analyzed:

Group 1: saline-challenged rats (control group) (n=6)

Group 2: adriamycin-challenged, vehicle-treated rats (n=10 at the beginning of the study)

Group 3: adriamycin-challenged, 1D11-treated rats (n=10 at the beginning of the study)

Adriamycin administration

Rats were anesthetized with 2.0% isoflurane (Abbott, Cham, Switzerland) delivered through a nose cone and adriamycin (4 mg/kg; doxorubicin hydrochloride, Sigma-Aldrich, Buchs, Switzerland) or vehicle (2 ml/kg of saline (0.9%)) was administered intravenously into the tail. Animals were allowed to recover immediately afterwards.

Compound administration

Adriamycin-challenged rats were dosed i.p. once a week with vehicle (saline) or the TGFβ$_{1,2,3}$ antibody, 1D11 (2 mg/kg; R&D Systems, Minneapolis, MN), starting on day 7 after adriamycin.

Biochemical analysis

Blood biochemistry

Blood was taken from the sublingual vein into edetic acid–coated tubes for monitoring hematologic values by using a counter (Technicon H*1E; Bayer, Zurich, Switzerland). Blood was also collected in heparin-coated Eppendorf tubes and centrifuged for 3 minutes at 13 000 rpm in an Eppendorf tabletop centrifuge (Biofuge; Brinkmann Instruments, Westbury, NY). The resulting supernatant was biochemically analyzed for determination of creatinine by using a Synchron CX5 instrument (Beckman Coulter, Fullerton, CA).

Glomerular filtration rate (GFR)

GFR was determined by multiplying the ratio of creatinine in urine and in blood serum by the amount of urine secreted per hour. Urine secretion was assessed by placing the animals in individual metabolic cages in which the bottom was permeable. During the stay in the metabolic cages (24 h), animals had access to food and water provided and their consumption was measured. Urine was collected in Plexiglas tubes cooled with ice water, the day before an MRI examination. The creatinine and total protein content in the urine were assessed by using a Synchron CX5 instrument.

Magnetic resonance imaging (MRI)

Experiments were performed on a 4.7-T Bruker Biospec MRI system (Bruker Biospin, Ettlingen, Germany) equipped with a self-shielded 12-cm bore gradient system capable of switching 200 mT/m in 170 µsec. The operational software of the scanner was Paravision (Bruker). A proton birdcage resonator with diameters of 72 mm (Bruker Biospin) was used for radiofrequency excitation and detection. During MRI signal acquisitions, animals were placed in supine position in a cradle made of Plexiglas. Body temperature was kept at 37±1°C using a heating pad. Following a short period of introduction in a box, anesthesia was maintained with 2% in a mixture of O2/N2O (1:2), administered via a nose cone. All measurements were performed on spontaneously breathing animals; neither cardiac nor respiratory triggering was applied.

After placing a rat in the magnet, scout fast images were acquired for localization purposes. Dynamic acquisitions of the kidney in conjunction with the i.v. administration of a

paramagnetic contrast agent were then followed by perfusion analyses using an intravascular agent containing SPIO nanoparticles. As SPIO is taken up by monocytes in the blood stream, further MRI acquisitions aiming at assessing macrophage infiltration into the kidney were performed 24 h later. Animals were fully recovered from anesthesia about 10 min after the end of an imaging session.

Dynamic contrast enhanced (DCE) MRI of the kidney

The acquisition of functional data was performed using a gradient-echo sequence with the following parameters: TR 10.6 ms, TE 2.2 ms, bandwidth 200 kHz, FOV 70x60 mm^2, matrix 128x72, slice thickness 1.5 mm, number of averages 4, flip angle of the radiofrequency excitation 25°. The position of the slice was chosen to have both the right and the left kidneys well delineated. The acquisition time for one image was of 3.05 s. In one session, 170 images of the same slice were acquired sequentially. Following the acquisition of 15 baseline images, a paramagnetic contrast agent (Gd-DOTA, Dotarem, Guerbet, Rossy, France; 20 µL/100 g body weight) approved for clinical use was administered intravenously as a bolus and then flushed with 0.3 mL of saline within 2 s. This procedure is based on the fact that Gd-DOTA is excreted though the kidneys [147-149].

Perfusion

Perfusion measurements were performed using a gradient-echo sequence with the following parameters: TR 8.7 ms, TE 3.8 ms, bandwidth 100 kHz, flip angle of the excitation pulse 10°, FOV 70x60 mm^2, matrix 128x64, slice thickness 1.5 mm. The acquisition time for one image was 560 ms. Eighty images were acquired consecutively at the same anatomical location. After the 10^{th} image, 500 µL/kg body weight of SPIO particles (Endorem, Guerbet; 11.2 mg Fe/mL, nanoparticles having a diameter on the order of 150 nm) were injected into the tail vein for 1 s.

Anatomy

Anatomical images were acquired using a gradient-echo sequence with the parameters: TR 22.6 ms, TE 8.4 ms, bandwidth 29.8 kHz, flip angle of the excitation pulse 10°, FOV 60x60 mm2, matrix size 128x128, slice thickness 1.5 mm, and number of averages 20, fat suppression, resulting in a measurement time of 57.9 s per image. A single slice image was obtained by interpolating the dataset to 256x256 pixels. Five contiguous slices were acquired sequentially per imaging session.

MR image analysis

Kidney function via DCE MRI

Following the bolus injection of the contrast agent, MRI monitored the passage of the contrast agent through the renal system in a time-resolved manner, thus yielding a measure for the kidney function. Functional information was derived by analyzing the mean signal intensities for regions-of-interest (ROIs) in the outer strip of the outer medulla, for each of the 170 images comprising one functional data set. Position, shape, and size of the ROIs were carefully chosen in order to ensure that they covered approximately the same region, despite movements of the kidney caused by respiration.

From the time-dependent signal intensity curves specific to each kidney region, the local Gd-DOTA concentration ([Gd-DOTA]) was assessed using the procedure described in detail in [139,140,150]. This procedure is based on the fact that Gd-DOTA is predominantly excreted though the kidneys [147-149] without tubular secretion or reabsorption [147]; thus, the main route of its elimination is glomerular filtration. Time-course changes in signal intensities were translated into local Gd-DOTA concentrations assuming a linear dependence with signal enhancement, as described previously [139,140].

For each animal, the mean of the Gd-DOTA concentrations in the left and right kidneys was obtained for the outer stripe of the outer medulla in a time-resolved manner, from the signal changes induced by the contrast agent in the MR images. From this [Gd-DOTA] profile, the tracer washout rate (TWR, in mmol/min) has been determined by calculating the rate with which the concentration decreased over time.

Perfusion analysis

The superparamagnetic contrast agent induced local changes in susceptibility that resulted in a signal attenuation proportional to the perfusion of the kidney. For a series of images, signal intensities were assessed on ROIs located in the cortex/outer stripe of outer medulla. Position, shape, and size of the ROIs were carefully chosen in order to ensure that they covered approximately the same region, despite movements of the kidney caused by respiration. The mean signal intensities for the pre-injection images provided baseline intensities, S(0). Perfusion indexes were determined from the mean values of the ratios [151] $-\ln[S(t)/S(0)] \sim TE.V.c_T(t)$ where TE is the echo time, V the blood volume, and c_T the concentration of contrast agent, over five images following injection of the superparamagnetic contrast agent.

Anatomical analysis

Signal intensities were assessed on ROIs located in the cortex/outer stripe of outer medulla. Position, shape, and size of the ROIs were carefully chosen in order to ensure that they covered approximately the same anatomical region. The signal in the kidney was normalized to signal in the muscle. An average signal intensity was calculated over the five anatomical images acquired for every animal at each imaging session.

Post-mortem analyses

At the end of the study, rats were sacrificed with an overdose of CO_2 immediately after an MRI acquisition. Following the organ's removal, the left kidney was used for histological analyses, while the right kidney was used for hydroxyproline analyses.

Histology

Histological analysis was performed in a blind manner as described in more detail earlier [152,153]. Kidneys were harvested and fixed with 10% neutral phosphate-buffered formalin, pH 7.4, for 48 h. After fixation of the tissue, dehydration through increasing graded series of ethylic alcohol (50%, 70%, 80%, and 100%) and embedding in paraffin wax, six serial 3-µm sections were cut longitudinally through the kidneys, so as to include cortical and medullary tissue as well as renal papilla, and six different stainings were applied: H&E to assess the general morphology; PAS reaction for the demonstration of basal membranes and

carbohydrates, in order to evaluate the extent of glomerulosclerosis and tubular infiltration; picrosirius red for the demonstration and the quantification of collagen (fibrosis); AFOG for the demonstration of glomerular protein deposits; Perls'reaction for the demonstration of iron in the kidney; and ED1 immunohistochemistry for the detection of macrophages in the kidney.

Assessment and scoring of abnormal histological features

Following features were scored: interstitial changes, tubulopathy, and glomerulopathy.

Interstitial changes: infiltration of the renal parenchyma with mononuclear cells. Cellular infiltration was assessed on the whole transverse kidney section as follows [154]: 0 = none; 1 = occasional infiltrates surrounding glomeruli and blood vessels; 2 = multiple infiltrates surrounding glomeruli and blood vessels; 3 = severe infiltration accompanied by peritubular infiltration and interstitial fibrosis

Tubulopathy: tubulitis, sclerotic tubules, distended tubules and hyaline casts. Five hundred tubules were counted per section and the number of either infiltrated, sclerotic, distended or hyaline cast content tubules was expressed as a percentage of the total number of tubules per section

Glomerulopathy: PAS positive deposits, mesangial expansion, enlarged capillary lumen and thickening of the basal membrane. One hundred glomeruli were counted per section and the number of abnormal glomeruli was expressed as a percentage of the total number of glomeruli analyzed per section.

Tubulopathy and glomerulopathy were scored semi quantitatively on a scale (0 to 3) derived from the Banff scoring for chronic rejection [155] as follows: 1 = less than 25% of abnormal features; 2 = 26 to 50% of abnormal features; 3 = more than 51% of abnormal features.

Assessment and scoring of ED1 infiltration

Immunohistochemistry labeling for ED1 positive macrophages was done on each kidney section and the quantification performed as follows:

Glomeruli: One hundred glomeruli were observed per section and the number of glomeruli infiltrated with at least one ED1 positive cell was counted. Results were expressed as a percentage of positive ED1 glomeruli.

Interstitium: ED1 positive staining was quantified using the image analysis software "Spectrum Plus" (Aperio, Nikon, Egg, Switzerland). ED1 labeled slides were scanned with SanScope (Aperio) at x40 magnification. The whole surface of each kidney section was manually delineated and the color corresponding to the ED1 was extracted by threshold setting. The ED1area within the delineated region was automatically calculated. Values were recorded as a percentage of ED1 of the total measured area.

For each animal, a nephropathy score was calculated by adding the glomerulopathy score, the score for mononuclear infiltration into the interstitium, and the tubular score.

Quantification of iron

Sections were stained applying Perl's Prussian blue reaction to demonstrate ferric iron in tissue. The percentage of iron was determined using a classical black/white digitization. Two representative areas of 280,000 μm^2 each were chosen in the cortex and results are presented as means of the two values assessed per kidney.

Quantification of collagen

Sections (3 µm) were stained with picrosirius red for the identification of collagen fibers and newly synthesized collagen. As described earlier for analyses of pulmonary fibrosis [27,70], collagen was quantified using the program "Histolab" (Microvision Instruments, Evry, France). Picrosirius-stained slides were examined with a light microscope (Eclipse E600, Nikon) connected to a CCD progressive scan video color camera (XCD-U100 CR, Sony, Tokyo, Japan). One third of the surface of each kidney section was captured at x10 magnification and the color corresponding to picrosirius red was extracted by threshold setting and the all collagen area automatically calculated. Values were recorded as a percentage of picrosirius of the total measured area.

Determination of hydroxyproline in kidney tissue samples

Hydroxyproline assessments in kidney tissue were performed using analogous procedures described earlier for the lung [120]. Kidney tissue samples were weighed, dried in an oven at 90°C overnight, and the weight was recorded again. Dry tissues were then boiled in 0.5 mL of 6 M HCl at 120°C overnight (8-16 hours) in Pyrex tubes with heat- and acid-resistant screw-on caps (article TES-830-70G; Fisher Scientific, Wohlen, Switzerland). After cooling down and adding 5 µL of phenolphthalein (1%), the samples were neutralized with NaOH 10 M (Sigma N°S-5881) and 6 M HCl. Black precipitate and brown color was removed by adding 100 µL of carbon suspension [10 mg/mL activated charcoal (article C4386; Sigma-Aldrich, Buchs, Switzerland) in water], centrifugation, and filtration. Five microliters of standard or hydrolyzed sample were pipetted in triplicate onto a 96 well plate, and 5 µL citrate acetate buffer (5% citric acid, 7.2% sodium acetate, 3.4% sodium hydroxide, 1.2% glacial acetic acid, distilled water) was added to each well, as well as 100 µL of freshly prepared chloramine-T solution (14.1 mg chloramine-T, 0.1mL n-propanol, 0.1mL distilled water, 0.8mL citrate acetate buffer). The samples were then incubated at room temperature for 20 minutes. After adding 100 µL of Ehrlich's reagent (2.5 g of 4-(dimethylamino)benzaldehyde, 9.3 mL of n-propanol, and 3.9 mL of 70% perchloric acid), the wells were incubated for 20 minutes at 65°C. After cooling down, the samples were measured at 550 nm on a spectrophotometer (SpectraMax 340PC, Molecular Devices, Sunnyvale, CA, USA); a standard curve from 5 to 100 mg hydroxyproline in water was created. Data were expressed as µg/kidney.

Statistics

For statistical analysis the software SYSTAT 13 (Systat Software, Inc., San Jose, CA) has been used. GFR, biochemical and MRI data were analyzed employing ANOVA with random effects (SYSTAT 12, Systat Software, Inc., San Jose, CA) to take into account the longitudinal structure of the data. Histological data were analyzed with Anova. Kruskal-Wallis tests were used to compare histological scores. RT-PCR results were analyzed with t-tests. Statistical significance was assumed at the level $p<0.05$.

Results

Because of necrosis in the tail around the site of injection, one animal in the adriamycin group and three rats in the adriamycin plus 1D11 group had to be sacrificed prematurely, around ten days after injection.

GFR and biochemical markers

Figure 49A summarizes the GFR determined for saline and adriamycin-treated rats, derived from the ratio of creatinine in urine and blood, multiplied by the amount of urine secreted per hour. Protein in urine is shown in Figure 49B.

DCE-MRI

Figure 50A shows representative profiles of [Gd-DOTA], calculated from signal changes evaluated in the outer stripe of the outer medulla. From such profiles, it becomes evident that, in adriamycin-treated rats, the course of contrast material in the kidney differed significantly from that in saline-treated rats, both concerning the time point of maximum concentration, and the maximum concentration itself. The TWR, assessed from such concentration profiles (Figure 50B), is summarized in Figure 50C for the different treatment groups. The data suggest that the kidney function was already impaired at week 2 after adriamycin administration.

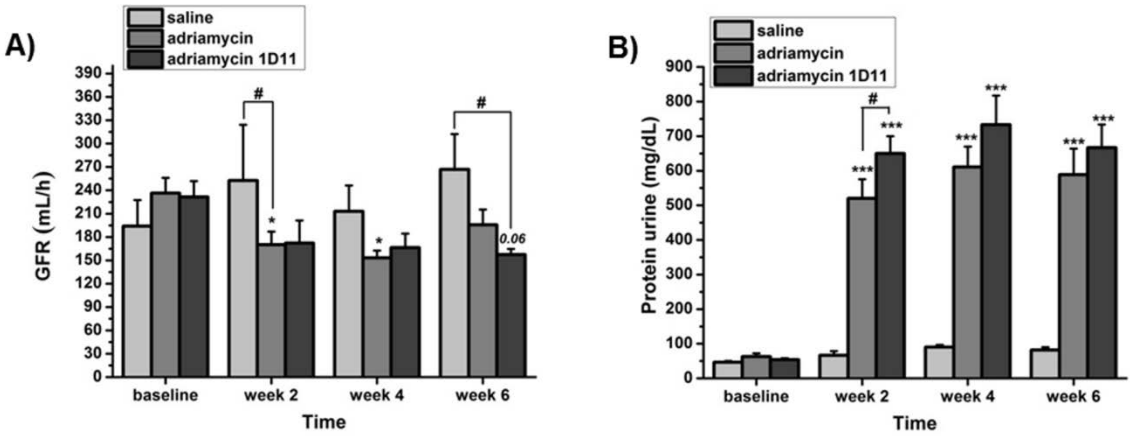

Figure 49: Biochemical assessments in blood and urine. A) GFR (means±sem) and B) protein in urine (means±sem) for saline and adriamycin-treated rats. The levels of significance reflect comparisons using Anova with random effects (those levels indicated above the bars correspond to comparisons with the baseline values, in the same group). Although not indicated explicitly, the protein values for adriamycin-challenged animals were significantly higher ($p<0.001$) compared to saline controls at all time points, except at baseline.

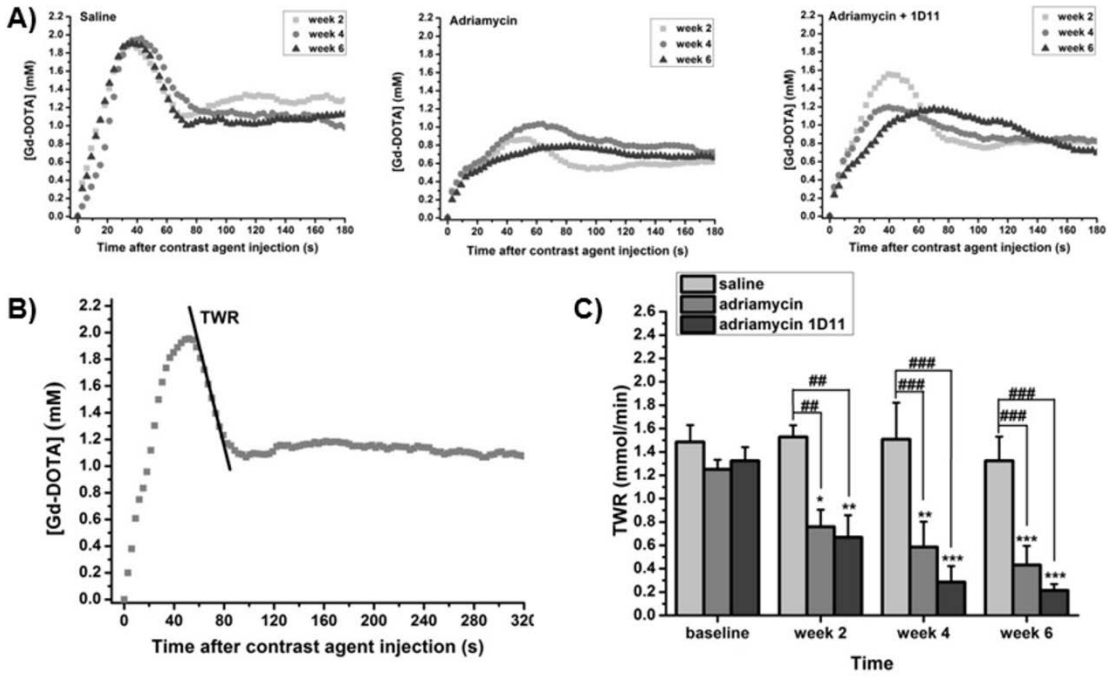

Figure 50: Analyses of DCE MRI experiments. A) Time profiles of Gd-DOTA concentration ([Gd-DOTA]) in the outer stripe of the outer medulla for three rats (one challenged with saline, the other challenged with adriamycin, and the third challenged with adriamycin and treated with 1D11). The profiles correspond to DCE MRI measurements at 2, 4 and 6 weeks after administration of saline or adriamycin. B) Time profile of Gd-DOTA concentration in the outer stripe of the outer medulla at baseline. The tracer washout rate (TWR) was calculated from the clearance of the contrast agent in the analyzed ROI. C) TWR in the outer stripe of the outer medulla (means±sem) for saline and adriamycin-treated rats. The levels of significance reflect comparisons using Anova with random effects (those levels indicated above the bars correspond to comparisons with the baseline values, in the same group).

Perfusion MRI

Figure 51 summarizes the perfusion indices assessed at different time points after saline or adriamycin injection, for the different groups of animals. The data reveal that, for adriamycin-treated rats, kidney perfusion was reduced during the course of the experiment.

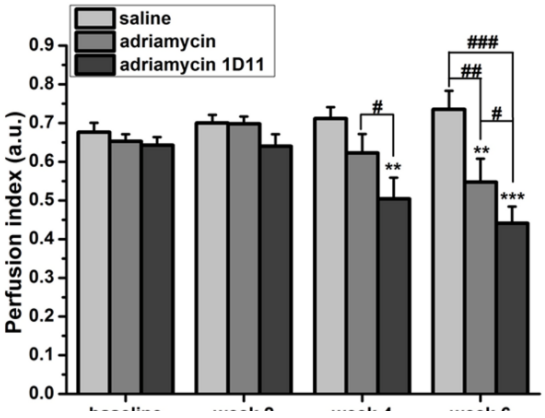

Figure 51: Perfusion index (means±sem) derived using a bolus tracking method, with injection of a SPIO contrast agent (Endorem). The levels of significance reflect comparisons using Anova with random effects (the levels indicated above the bars correspond to comparisons with the baseline values, in the same group).

Anatomical MRI

Starting week 4 after adriamycin challenge, signal attenuation was observed in the kidney cortex/outer medulla in anatomical images acquired 24 h after Endorem injection (Figure 52 and 53A). For saline-challenged rats, signal intensity remained unchanged during the experimental period.

Histology - Macrophage infiltration

Analysis of Prussian blue-stained histological sections revealed moreover that iron was present only in macrophages (Figure 53B). At the interstitial level, histology revealed an infiltration of the renal parenchyma with mononuclear cells among which the majority was macrophages expressing ED1 (Figure 53C-D). At week 6 after adriamycin injection, highly significant negative correlations were found between the relative MRI signal intensity in the kidney in anatomical images acquired 24 h following SPIO administration, and the histological quantification of iron ($R=-0.74$, $p=2.6\times10^{-4}$) and ED1 ($R=-0.76$, $p=7.0\times10^{-5}$) (Figure 53 E-F).

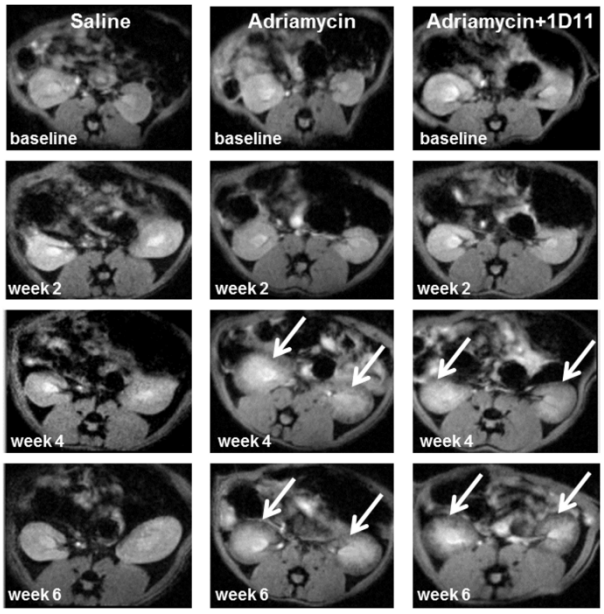

Figure 52: Assessment of macrophage infiltration by MRI. MR images acquired from three rats at baseline and 2, 4, and 6 weeks after injection of saline or adriamycin. Animals that had received adriamycin were treated with either vehicle or 1D11. At each time point, acquisitions took place 24 h after Endorem administration. Starting at week 4, prominent signal decrease in the cortex/outer medulla can be noted for adriamycin-challenged rats (arrows).

Nephropathy

The main features of nephropathy induced by adriamycin at 6 weeks after administration of the antibiotic were:

(a) at the glomeruli level: mainly deposits of PAS positive material, enlargement of capillary lumen, thickening of the basal membrane with rare mesangial expansion. These abnormal

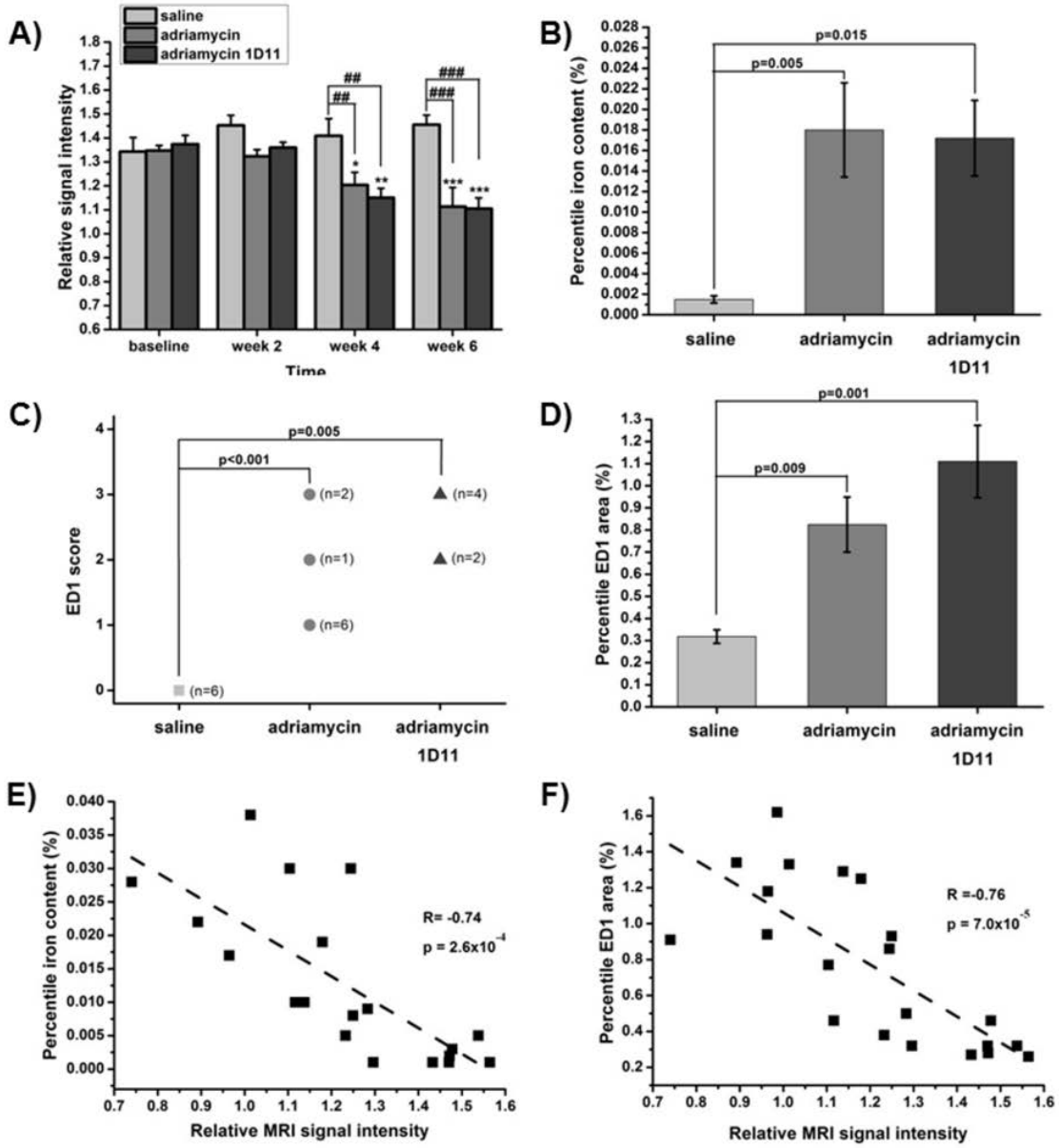

Figure 53: Assessment of macrophage infiltration by MRI and histology. A) Signal intensity in the cortex/outer medulla normalized to that in the muscle (means±sem). The levels of significance reflect comparisons using Anova with random effects (the levels indicated above the bars correspond to comparisons with the baseline values, in the same group). B) Percentile iron content in the histological sections (means±sem). The levels of significance reflect Anova comparisons. C) ED1 score on histological slices from the left kidneys at week 6. The significance levels p refer to Kruskal-Wallis comparisons between the groups. The numbers in parenthesis indicate how many animals received a given score. D) Percentile ED1 area (means±sem). The levels of significance correspond to Anova comparisons between the groups. E) Correlation between iron content and the relative MRI signal intensity in the kidney cortex/outer medulla. F) Correlation between ED1 staining and the relative MRI signal intensity in the kidney cortex/outer medulla. R stands for the Pearson's correlation factor.

characteristics were named glomerulopathy. The histological observations are summarized in Figure 54A; (b) at the tubular level: mainly sclerotic tubules with atrophy of the epithelial cells, distended tubules, hyaline casts and rare tubulitis (tubules infiltrated with inflammatory cells).

Figure 54 B summarizes the histological observations of kidney sections concerning tubuli. The total nephropathy scores, comprising the sum of the glomerular and tubular scores, are presented in Figure 54C.

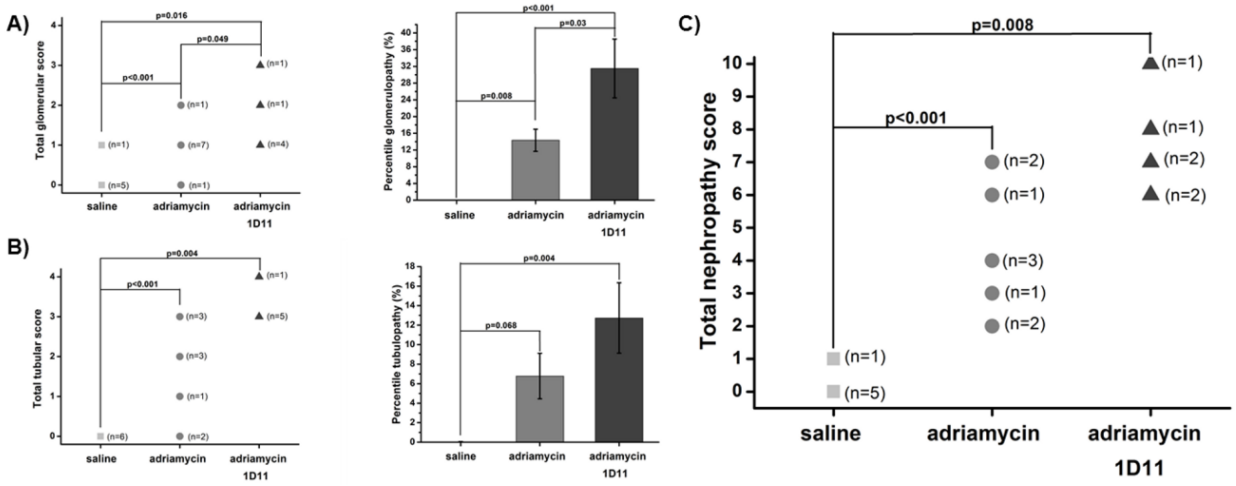

Figure 54: Histology of glomeruli, tubuli and nephropathy at week 6. A) Left: Total glomerular score. The significance levels p refer to Kruskal-Wallis comparisons between the groups. The numbers in parenthesis indicate how many animals received a given score. Right: Percentile glomerulopathy (means±sem). The levels of significance correspond to Anova comparisons between the groups. B) Left: Total tubular score. The significance levels p refer to Kruskal-Wallis comparisons between the groups. The numbers in parenthesis indicate how many animals received a given score. Right: Percentile tubulopathy (means±sem). The levels of significance correspond to Anova comparisons between the groups. C) Nephropathy scores calculated by adding the glomerulopathy scores, the scores for mononuclear infiltration into the interstitium, and the tubular scores. The significance levels p refer to Kruskal-Wallis comparisons between the groups. The numbers in parenthesis indicate how many animals received a given score.

Fibrosis

The overall quantification of picrosirius demonstrated a doubling in collagen content in the kidneys of rats that received adriamycin. Treatment with 1D11 had no influence on collagen (Figure 55A).

Hydroxyproline assessments

A modest increase in hydroxyproline was found in the kidneys of adriamycin-challenged rats, consistent with the formation of fibrosis in the model (Figure 55B).

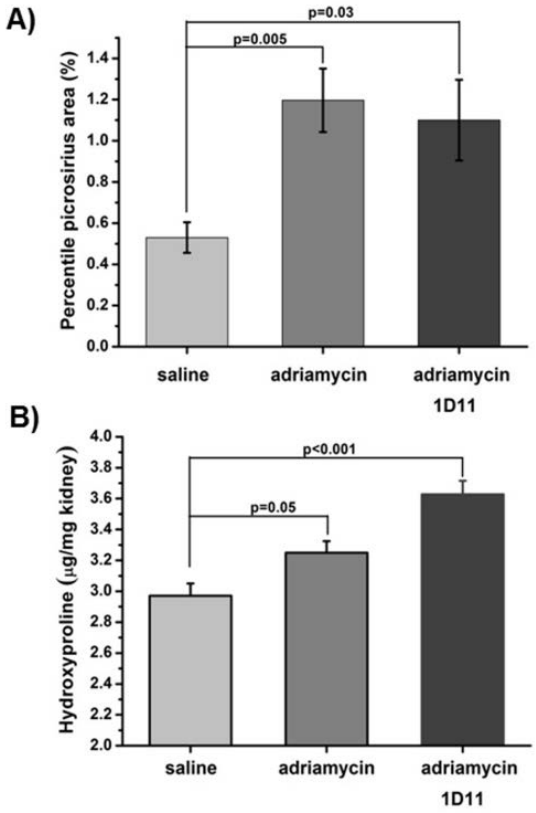

Figure 55:. Fibrosis assessment at week 6 by histological and hydroxyproline analyses. A) Percentile picrosirius area on histological slices from left kidneys. Values are presented as means±sem. The levels of significance correspond to Anova comparisons between the groups. B) Hydroxyproline values (means±sem) in the right kidneys. The levels of significance reflect Anova comparisons.

Discussion

Histological analysis is a cornerstone for studying mechanisms of renal disease. However, analysis in human disease is limited by a relative paucity of tissue availability. Renal biopsies are only pursued if a presumptive diagnosis cannot be established on clinical grounds. Similarly to the situation of human studies, biopsies in animals are usually limited to one time point, because of their invasive nature. Tissue sampling is thus typically restricted to the time of disease presentation and is rarely performed in follow-up, providing a mere snapshot of disease course. In view of the limitations of invasive methods to study renal disease, we aimed at verifying here the suitability of MRI to longitudinally follow the course of adriamycin-induced kidney nephropathy in rats. Both anatomical and functional readouts were characterized.

A single intravenous injection of adriamycin leads to proteinuria and progressive renal disease, with the onset of proteinuria occurring within 5–7 days of exposure [156-158]. This is accompanied by a progressive reduction in glomerular filtration rate, as measured by increased serum creatinine and/or blood urea nitrogen [156,159-161]. In the present work, proteinuria was present throughout the study (Figure 49B). Compared to baseline values within the same group of animals, serum creatinine levels increased after adriamycin injection

(data not shown). However, differences in serum creatinine levels at baseline hampered a clear differentiation between the experimental groups: only at week 6 was the serum creatinine level significantly higher in adriamycin-treated animals compared to saline-challenged rats. GFR determined through biochemical analyses of urine and blood (Figure 49A) was tendentially reduced in the adriamycin groups. In contrast, through the clearance studies of Gd-DOTA, DCE MRI clearly revealed an impaired kidney function as the tracer washout rate (TWR) was significantly reduced at all time points after adriamycin (Figure 50C). These results indicate that MRI is significantly more sensitive than the biochemical analyses of urine and blood to reveal the impairment of kidney function elicited by adriamycin.

Histological analysis performed at the end of the study revealed glomerulopathy (Figure 54A), sclerotic tubules with atrophy of the epithelial cells and distended tubules (Figure 54B), fibrosis (Figure 55A), and macrophage infiltration into the renal parenchyma (Figure 53 B-D) in kidneys of adriamycin-challenged rats. The nephropathy scores, corresponding to the sum of glomerulopathy, mononuclear infiltration, and tubular scores, were significantly increased in adriamycin-treated kidneys (Figure 54C). The increase in hydroxyproline (Figure 55B) found in the kidneys of adriamycin-challenged rats was consistent with the formation of fibrosis in the model. Overall, these changes reflect features of the adriamycin model in rats [46,47,156].

The decrease of kidney perfusion detected by MRI in adriamycin-challenged rats (Figure 51) was consistent with progressive renal diseases being associated with both a progressive loss of vascular structures [162-165] and an excess of vasoconstrictor substances such as angiotensin-II and endothelin-1 [166,167], both of which may decrease oxygen supply to the renal parenchyma. Moreover, adriamycin has been shown to decrease nitric oxide (NO) formation and thus lead to endothelial dysfunction [168,169]. It has been further shown that, in adriamycin-induced nephrotic syndrome, vascular adriamycin exposure and nephrosis affect vascular function [170]**.** Adriamycin exposure reduces endothelium-dependent vasodilation, most likely due to impaired stimulated NO release without further impairment by nephrosis. Nephrosis, on the other hand, is associated with a reduced basal NO release—without an additional effect of vascular adriamycin exposure—leading to impairment of the normal vascular modulation of vasoconstrictor stimuli. This modulation is an important vascular defense mechanism [170] and its impairment might well be involved in the high cardiovascular morbidity in proteinuric patients.

The anatomical MRI data generated 24 h after SPIO administration (Figures 52 and 53A) suggested macrophage infiltration into the kidneys of adriamycin-challenged rats. The signal changes detected *in vivo* correlated well with histological analyses of macrophage infiltration (Figure 53E-F). These results are consistent with data from the literature demonstrating that adriamycin induces monocyte/macrophage infiltration in glomeruli and in the interstitium [171,172]. Also using SPIO administration, we've shown before that detection of macrophage infiltration by MRI can serve as an earlier marker of chronic rejection in models of kidney transplantation [152,153].

It has been demonstrated earlier that 1D11, in particular in combination with angiotensin II blockade, had antifibrotic effects in models of glomerulonephritis [42,145,146]. In those studies, the antibody was administered preventatively, before onset on injury. In the present work, the fact that 1D11 was given therapeutically, i.e. antibody treatment started after injury onset, may have been one of the reasons for its lack of efficacy. Benigni et al. [173] showed in a rat model of nephropathy that beneficial effects of TGF-β antagonism depend on when treatment is started. Early treatment with 1D11 was effective; however, a combined treatment with an angiotensin-converting enzyme inhibitor was necessary to tackle renal damage in the phase of advanced disease. Some of our data suggesting that therapeutic treatment with 1D11 even worsened the renal injury induced by adriamycin are in agreement with observations in the literature showing that blockade of TGF-β using 1D11 significantly impaired the protective effect of regulatory T cells (Treg) in adriamycin-induced kidney injury in mice [174]. Infiltration of macrophages, an important component of innate immunity, is one of the most striking and constant features of chronic renal injury, and the degree of mononuclear cell infiltrate is predictive of subsequent disease progression [175]. Macrophages can contribute extensively to tissue damage and progressive renal failure via a number of mechanisms, including their production of proinflammatory cytokines and via their T cell–stimulatory capacity [176,177]. It has been shown that $CD4^+CD25^+$ Treg can downregulate the effector phenotype of macrophages and inhibit their production of cytokines in a TGF-β-dependent manner, thereby hampering the innate effector function of these cells [174,178-180]. Thus, TGF-β, which is accepted as a key mediator of renal fibrosis, can protect against renal injury via Treg [45,174]. Our data are also consistent with a study by Mesnard et al. [181] showing that 1D11-treated wildtype mice demonstrated higher

proteinuria and more pronounced tubular injury in comparison to animals receiving an irrelevant matched isotype antibody, as well as with the fact that anti-TGF-β therapy could not reverse the degree of glomerular injury in male rats with preexisting renal injury [182]. Moreover, modulation of NO can exacerbate tubulointerstitial inflammation in proteinuric rats [183].

In summary, the data presented here demonstrate the usefulness of MRI in providing longitudinal functional and cellular information in a rat model of nephropathy. The DCE MRI data were shown to be significantly more sensitive than conventional assessment of GFR based on the biochemical analyses of blood and urine to reveal abnormalities in kidney function induced by the antibiotic. Anatomical imaging 24 h following SPIO administration detected contrast changes that were significantly and inversely correlated with the infiltration of macrophages. Both functional and cellular data can support *in vivo* pharmacological testing in the model [184-186]. Moreover, the MRI techniques have translational potential for compound testing in humans as the contrast agents adopted are approved for clinical use. Of course, care needs to be taken as safety concerns for Gd-based contrast agents have been raised, in particular in the context of nephrogenic systemic fibrosis [187,188], a highly debilitating scleroderma-like disease occurring in patients with severe or end-stage renal failure. The use of macrocyclic Gd-chelates (such as Gd-DOTA) as contrast agent for DCE-MRI examinations, since they are safer and more stable when compared to linear open-chain agents [189,190], and the restriction to examining patients with GFR values > 30 ml/min/1.73 m^2 [191,192], would for instance be precautions when trying to adopt this approach to pharmacological tests in the clinics.

7) Overall Discussion and Conclusions

7.1) Discussion

The studies performed in this thesis focused on three pillars of preclinical pharmaceutical research in the context of lung and kidney fibrosis: the availability of appropriate animal models, the availability of readouts or parameters that quantitatively reflect disease evolution in those models, and the availability of reference compounds, known to interfere with the disease development. To date no pharmacological treatment is available for lung fibrosis, a lethal disease characterized by tissue deposition and reduced organ function, or renal fibrosis, characterized by glomerulosclerosis, sclerotic tubuli, and tubulointerstitial inflammation. Thus, strengthening of the three mentioned pillars will support the preclinical research on therapeutics against the two crippling diseases.

Contribution to the availability of appropriate animal models for pulmonary and renal fibrosis

Oropharyngeal aspiration of bleomycin led to a strong improvement of the in vivo *model*

Single [33-35] or multiple [36] IT or IN instillation of bleomycin is commonly used to induce experimental pulmonary fibrosis in small rodents. In Chapter 4.1 (“Administration of Bleomycin via the Oropharyngeal Aspiration Route Leads to Sustained Lung Fibrosis in Mice and Rats as Quantified by UTE-MRI and Histology”) it was shown that OA of bleomycin in mice, compared to IN administration, led to a stronger fibrotic response and to pulmonary fibrosis that was localized also in the lung periphery and not only around the main airways. These data resulted in an improvement of the animal model. The dose of bleomycin could be strongly reduced by a factor of 2.5 compared to the IN route of administration, leading to a significantly lower bodyweight loss of bleomycin treated animals. Of importance, a refinement of the model in the sense of the 3R concept was thus achieved. The shift of the fibrotic foci from the main airways more to the periphery makes the model more comparable to the human disease, which is an important point for preclinical compound studies and validation of methods and readouts that might be applied to humans in a later phase.

Adriamycin induced nephropathy as a model for kidney fibrosis

In Chapter 6.1 ("Adriamycin-Induced Nephropathy in Rats: Functional and Cellular Effects Characterized by MRI") it was shown that i.v. administered adriamycin in rats lead to renal fibrosis including pathological changes as glomerulopathy, sclerotic tubules with atrophy of the epithelial cells and distended tubules, macrophage infiltration into the renal parenchyma, and hydroxyproline deposition, as well as functional changes as reduced glomerular filtration rate, perfusion, and renal clearance. Although adriamycin was already known to induce nephropathy in small rodents, the presented data, especially the *in vivo* MRI readouts, delivered further relevant information about the model. The availability of an appropriate and well understood animal model for renal fibrosis is of importance for pharmaceutical research, since there is still a lack of therapeutic drugs against the disease leading to organ failure that often requires its replacement. The adriamycin model in rats may certainly support the preclinical research on anti-fibrotic drugs.

Contribution to the availability of readouts or parameters that quantitatively reflect disease evolution

UTE-MRI reduced acquisition time for imaging the lungs of bleomycin-challenged mice and rats

It has been shown in our laboratories that MRI can non-invasively follow the course of lung injury induced by administration of bleomycin to mice [70] and rats [27]. The data of these earlier studies were produced applying a GE sequence, which required an acquisition time over twenty minutes for imaging the whole lung of a mouse or a rat. For the studies discussed in this thesis, except for gated acquisitions, UTE sequences have been used to investigate lung volume and bleomycin-induced lung lesions. Due to a reduction of the echo time and a decrease in the number of averages, the acquisition times could be significantly shortened as compared to previous work [70,72]. Only four minutes were needed to generate images covering the whole lung of a mouse. The acquisition time for rat lung imaging could be reduced to about seven minutes using 2D UTE and eleven minutes using 3D UTE. This reduction of acquisition time means an improvement for pharmaceutical research. With only 4 min acquisition time per animal, high-throughput imaging becomes feasible, which is of relevance since *in vivo* studies often include up to 50 animals.

A reduced acquisition time means also a shorter anesthesia time. Although MRI is a noninvasive tool, anesthesia imposes some stress on the animals. Thus, a reduction of time in narcosis certainly supports the 3R concept in the sense of refinement.

Modulation of MRI signals by hyaluronidase

Although MRI has been shown to detect bleomycin-induced lung injuries in the lung fibrosis model, with significant correlations to *post-mortem* collagen analyses (histology of picrosirius staining and hydroxyproline), additional effort was made to investigate the nature of the detected signals. The work in Chapter 4.2 ("MRI-detected, bleomycin-induced lung injuries in mice and rats: What is causing the observed changes in MRI signal?") focused on the origin of these MRI signals and investigated the role of hyaluronic acid (HA) in ongoing fibrotic processes. The fact that bleomycin-induced MRI-signals could be modulated by hyaluronidase (HYAL) support the hypothesis that proteoglycans as HA, through their ability to attract water, contributed to the detected MRI-signals. Since HA has been shown to be involved in fibrotic processes [109,110] and co-localizes with parts of the extracellular matrix (ECM) [101], the data strengthen the detection of BLM-induced injuries by MRI as a noninvasive *in vivo* readout for PF.

Total Lung Volume as a new readout for lung fibrosis?

During the past, the amount of lung collagen and related parts of the ECM, as hydroxyproline, were in the focus for the *post-mortem* detection of pulmonary fibrosis. Another way of monitoring the course of the disease *in vivo*, was the assessment of lung function and mechanics: Tissue resistance and elastance, as well as decreased compliance have been shown in humans [2,15] and in small rodent pulmonary fibrosis models [23-25,28-31]. Moreover, changes in tidal volume and breathing cycle times have been shown in a mouse fibrosis model [113]. In this thesis MRI-detected lung volume was shown to be a non-invasive readout for tissue deposition in the rat bleomycin model for pulmonary fibrosis. Tissue deposition (of e.g. collagen, elastin and proteoglycans) induced by bleomycin in the lung leads to an increase in lung resistance [23,24,26,111,112] and thus to a decrease in lung compliance. Therefore, MRI-detected alterations in lung volume might also be considered as reflecting changes of lung function in the model. As therapies aim primarily at improving the lung

function, incorporation of this readout into pharmacological testing in the bleomycin model is of interest.

Visualization of renal perfusion, clearance, and macrophage infiltration in the rat adriamycin model

In Chapter 6.1 ("Adriamycin-Induced Nephropathy in Rats: Functional and Cellular Effects Characterized by MRI"), MRI was shown to detect nephropathy in the rat adriamycin model. Renal clearance was visualized by the i.v. administration of Gd-DOTA and the detection of signal changes by GE-MRI, based on the fact that Gd-DOTA decreases the T1 of protons and is excreted through the kidneys [147-149]. Tracer washout rate was determined from the Gd-DOTA concentrations, that were obtained in a time-resolved manner from the induced signal changes, and found to be significantly reduced at all time points after adriamycin injection.

Kidney perfusion was investigated using an i.v. injection of SPIO particles that induced, by a change of the local magnetic field (T2* effect), a decrease of MRI signal and was found to be reduced six weeks after adriamycin-challenge. Twenty-four hours after SPIO injection, anatomical images have been acquired. MRI signal was decreased in adriamycin-treated rats four and six weeks after challenge, with a high correlation to the presence of iron loaded macrophages in the kidney, thus suggesting that MRI was able to visualize macrophage infiltration in the rat adriamycin model.

The three *in vivo* MRI readouts, visualization of macrophage infiltration, renal clearance, and kidney perfusion, are shown in this thesis to be valuable tools to monitor nephropathy *in vivo*. The DCE MRI data were shown to be significantly more sensitive than conventional assessment of GFR based on the biochemical analyses of blood and urine to reveal abnormalities in kidney function induced by the antibiotic. In combination with the adriamycin model, these MRI techniques may have a high impact on the development of compounds against renal fibrosis. Moreover, the MRI techniques have translational potential for compound testing in humans as the contrast agents adopted are approved for clinical use.

1D11 showed no therapeutic on adriamycin-induced nephropathy

The TGF-β antibody, 1D11, in particular in combination with angiotensin II blockade, showed antifibrotic effects in models of glomerulonephritis [42,145,146]. In those studies, the antibody was administered preventatively, before onset of injury, while in this thesis the therapeutic effect of the antibody was investigated. As described in Chapter 6.1 ("Adriamycin-Induced Nephropathy in Rats: Functional and Cellular Effects Characterized by MRI"), 1D11 was administered after the induction of nephropathy by injection of adriamycin. None of the assessed readouts showed a therapeutic effect of 1D11 on adriamycin-induced nephropathy. Of note, some of the readouts suggested that therapeutic treatment with 1D11 even worsened the renal injury induced by adriamycin, which is in agreement with data in the literature showing that blockade of TGF-β using 1D11 significantly impaired the protective effect of regulatory T cells (Treg) in adriamycin-induced kidney injury in mice [174]. The MRI-detected influence of 1D11 on kidney perfusion and TWR were consistent with the histologically observed increase of glomerulopathy. Thus, when administered therapeutically, 1D11 may not serve as a reference compound for the preclinical research on renal fibrosis, but in the discussed study it confirmed MRI as an *in vivo* readout for adriamycin induced nephropathy.

PT100 showed an anti-fibro-proliferative effect in the mouse bleomycin model

As discussed in Chapter 5.1 ("Therapeutic Effects of the Fibroblast Activation Protein Inhibitor, PT100, in a Murine Model of Pulmonary Fibrosis"), effects of talabostat (PT100) in the lungs of bleomycin-challenged C57BL/6 mice were assessed longitudinally with proton MRI and compared to *post-mortem* analyses. The lesions induced by bleomycin and detected by UTE-MRI in the lungs of vehicle-treated mice progressed over time. In contrast, the responses elicited by BLM did not progress in animals receiving PT100. Histology at the end of the study demonstrated significant less fibrosis in PT100- than in vehicle-treated, BLM-challenged mice. These observations suggest that the compound administered therapeutically had an anti-fibro-proliferative effect. Of note, treatment with PT100 was started one day after the last bleomycin administration, a time point when substantial fibrosis was already present.

Although PT100 showed an anti-fibro-proliferative effect and stopped lesion progression, the MRI data showed that the compound was not able to reduce lung injuries that were induced during the first six day of bleomycin-challenge. Further studies should be performed by shifting the beginning of treatment to a later time point after last bleomycin administration.

Pasireotide reduced bleomycin-induced lung injuries in rats

Pasireotide (SOM230), a somatostatin analogue, binds to four out of five sst receptors (sst1, sst2A, sst3, and sst5) which have been reported to be upregulated in human fibrotic lungs [135] and in the mouse bleoymycin model [136]. As described in Chapter 5.2 ("Therapeutic Effects of Pasireotide on Bleomycin-Induced Lung Injuries in Rats - Detection by MRI and post-mortem analysis"), the long acting release (LAR) form of SOM230 was tested in a rat model of pulmonary fibrosis adopting a therapeutic experimental setting. SOM230 reduced bleomycin-induced lung lesions, which could be detected by 3D-UTE MRI. Twelve days after treatment begin no difference in MRI signal volume, total lung volume, and lung wet and dry weight could be observed between values for SOM230-treated, bleomycin-challenged rats and those for saline-challenged animals. The hydroxyproline content was slightly reduced for SOM230- compared to vehicle-treated, bleomycin-challenged rats. Based on the work exposed in Chapter 4.3 ("MRI-detected lung volume as a noninvasive readout for tissue deposition in the rat bleomycin model of pulmonary fibrosis"), the fact that total lung volumes as well as wet, and dry lung weights were comparable for saline-challenged animals and for SOM230-treated, bleomycin-challenged rats indicated an effect of SOM230 on lung function, since tissue deposition is related to lung elastance and compliance. All these data suggested that SOM230 had a therapeutic effect on bleomycin-induced pulmonary fibrosis. Although further results, as histology, RT-PCR, and blood sample analyses have to confirm these observations, the presented work strongly recommends SOM230 as a reference compound for MRI studies on pulmonary fibrosis. To our knowledge this is the first report that bleomycin-induced, MRI-detected lung injuries can be reduced by a compound in a model of established fibrosis.

7.2) Conclusion

The introduction of oropharyngeal aspiration of bleomycin for the induction of pulmonary fibrosis in small rodents and the confirmation of adriamycin-induced nephropathy as a model

of renal fibrosis strengthened the two models for pulmonary and renal fibrosis as tools for preclinical research.

Further improvements, regarding MRI as a non-invasive *in vivo* readout for pulmonary and renal fibrosis, were reached *(i)* by adopting UTE MRI for lung imaging, i.e., in the detection and quantification of lesions elicited by bleomycin in the lungs of mice and rats and in the evaluation of total lung volume as a readout for tissue deposition in the rat bleomycin model and *(ii)* by validating MRI techniques for the detection and quantification of renal function and macrophage infiltration in the adriamycin model of kidney injury in rats.

Additionally, two reference compounds, PT100 and SOM230, were found. This is of particular importance considering the fact that no appropriate reference compounds exist for experimental research in lung fibrosis. Therefore, PT100 and SOM230 may become very useful when testing further therapies for pulmonary fibrosis in small rodents.

Concluding, it can be said that the studies discussed in this thesis deliver contributions to all three pillars of preclinical pharmaceutical research: the availability of appropriate animal models, the availability of readouts or parameters that quantitatively reflect disease evolution in those models, and the availability of reference compounds, known to interfere with the disease development. Therefore, we hope that the studies summarized here will have an impact on preclinical research concerning pulmonary and kidney fibrosis in small rodents.

8) References

1. Gross TJ, Hunninghake GW (2001) Idiopathic pulmonary fibrosis. N Engl J Med 345: 517-525.
2. Katzenstein AL, Myers JL (1998) Idiopathic pulmonary fibrosis: clinical relevance of pathologic classification. Am J Respir Crit Care Med 157: 1301-1315.
3. Lazenby AJ, Crouch EC, McDonald JA, Kuhn C, 3rd (1990) Remodeling of the lung in bleomycin-induced pulmonary fibrosis in the rat. An immunohistochemical study of laminin, type IV collagen, and fibronectin. Am Rev Respir Dis 142: 206-214.
4. Liu Y (2006) Renal fibrosis: new insights into the pathogenesis and therapeutics. Kidney Int 69: 213-217.
5. Efstratiadis G, Divani M, Katsioulis E, Vergoulas G (2009) Renal fibrosis. Hippokratia 13: 224-229.
6. Raghu G, Collard HR, Egan JJ, Martinez FJ, Behr J, et al. (2011) An official ATS/ERS/JRS/ALAT statement: idiopathic pulmonary fibrosis: evidence-based guidelines for diagnosis and management. Am J Respir Crit Care Med 183: 788-824.
7. Kaarteenaho R (2013) The current position of surgical lung biopsy in the diagnosis of idiopathic pulmonary fibrosis. Respir Res 14: 43.
8. (2000) American Thoracic Society. Idiopathic pulmonary fibrosis: diagnosis and treatment. International consensus statement. American Thoracic Society (ATS), and the European Respiratory Society (ERS). Am J Respir Crit Care Med 161: 646-664.
9. (2002) American Thoracic Society/European Respiratory Society International Multidisciplinary Consensus Classification of the Idiopathic Interstitial Pneumonias. This joint statement of the American Thoracic Society (ATS), and the European Respiratory Society (ERS) was adopted by the ATS board of directors, June 2001 and by the ERS Executive Committee, June 2001. Am J Respir Crit Care Med 165: 277-304.
10. Gribbin J, Hubbard RB, Le Jeune I, Smith CJ, West J, et al. (2006) Incidence and mortality of idiopathic pulmonary fibrosis and sarcoidosis in the UK. Thorax 61: 980-985.
11. Scott J, Johnston I, Britton J (1990) What causes cryptogenic fibrosing alveolitis? A case-control study of environmental exposure to dust. BMJ 301: 1015-1017.
12. Raghu G, Weycker D, Edelsberg J, Bradford WZ, Oster G (2006) Incidence and prevalence of idiopathic pulmonary fibrosis. Am J Respir Crit Care Med 174: 810-816.
13. Iwai K, Mori T, Yamada N, Yamaguchi M, Hosoda Y (1994) Idiopathic pulmonary fibrosis. Epidemiologic approaches to occupational exposure. Am J Respir Crit Care Med 150: 670-675.
14. Coultas DB, Zumwalt RE, Black WC, Sobonya RE (1994) The epidemiology of interstitial lung diseases. Am J Respir Crit Care Med 150: 967-972.
15. von Plessen C, Grinde O, Gulsvik A (2003) Incidence and prevalence of cryptogenic fibrosing alveolitis in a Norwegian community. Respir Med 97: 428-435.
16. Karakatsani A, Papakosta D, Rapti A, Antoniou KM, Dimadi M, et al. (2009) Epidemiology of interstitial lung diseases in Greece. Respir Med 103: 1122-1129.
17. Brewster CE, Howarth PH, Djukanovic R, Wilson J, Holgate ST, et al. (1990) Myofibroblasts and subepithelial fibrosis in bronchial asthma. Am J Respir Cell Mol Biol 3: 507-511.
18. Roche WR, Beasley R, Williams JH, Holgate ST (1989) Subepithelial fibrosis in the bronchi of asthmatics. Lancet 1: 520-524.
19. Holgate ST, Davies DE, Lackie PM, Wilson SJ, Puddicombe SM, et al. (2000) Epithelial-mesenchymal interactions in the pathogenesis of asthma. J Allergy Clin Immunol 105: 193-204.
20. Jeffery PK (2001) Remodeling in asthma and chronic obstructive lung disease. Am J Respir Crit Care Med 164: S28-38.
21. Gong LK, Li XH, Wang H, Zhang L, Chen FP, et al. (2005) Effect of Feitai on bleomycin-induced pulmonary fibrosis in rats. J Ethnopharmacol 96: 537-544.

22. Izbicki G, Segel MJ, Christensen TG, Conner MW, Breuer R (2002) Time course of bleomycin-induced lung fibrosis. Int J Exp Pathol 83: 111-119.
23. Ebihara T, Venkatesan N, Tanaka R, Ludwig MS (2000) Changes in extracellular matrix and tissue viscoelasticity in bleomycin-induced lung fibrosis. Temporal aspects. Am J Respir Crit Care Med 162: 1569-1576.
24. Manali ED, Moschos C, Triantafillidou C, Kotanidou A, Psallidas I, et al. (2011) Static and dynamic mechanics of the murine lung after intratracheal bleomycin. BMC Pulm Med 11: 33.
25. Verbeken EK, Cauberghs M, Lauweryns JM, Van de Woestijne KP (1994) Structure and function in fibrosing alveolitis. J Appl Physiol 76: 731-742.
26. Dolhnikoff M, Mauad T, Ludwig MS (1999) Extracellular matrix and oscillatory mechanics of rat lung parenchyma in bleomycin-induced fibrosis. Am J Respir Crit Care Med 160: 1750-1757.
27. Babin AL, Cannet C, Gerard C, Wyss D, Page CP, et al. (2011) Noninvasive assessment of bleomycin-induced lung injury and the effects of short-term glucocorticosteroid treatment in rats using MRI. J Magn Reson Imaging 33: 603-614.
28. Thrall RS, Swendsen CL, Shannon TH, Kennedy CA, Frederick DS, et al. (1987) Correlation of changes in pulmonary surfactant phospholipids with compliance in bleomycin-induced pulmonary fibrosis in the rat. Am Rev Respir Dis 136: 113-118.
29. Dackor RT, Cheng J, Voltz JW, Card JW, Ferguson CD, et al. (2011) Prostaglandin E(2) protects murine lungs from bleomycin-induced pulmonary fibrosis and lung dysfunction. Am J Physiol Lung Cell Mol Physiol 301: L645-655.
30. Card JW, Voltz JW, Carey MA, Bradbury JA, Degraff LM, et al. (2007) Cyclooxygenase-2 deficiency exacerbates bleomycin-induced lung dysfunction but not fibrosis. Am J Respir Cell Mol Biol 37: 300-308.
31. Voltz JW, Card JW, Carey MA, Degraff LM, Ferguson CD, et al. (2008) Male sex hormones exacerbate lung function impairment after bleomycin-induced pulmonary fibrosis. Am J Respir Cell Mol Biol 39: 45-52.
32. Ueda Y, Saito A, Fukuoka Y, Yamashiro Y, Ikeda Y, et al. (1983) Interactions of beta-lactam antibiotics and antineoplastic agents. Antimicrob Agents Chemother 23: 374-378.
33. Hay J, Shahzeidi S, Laurent G (1991) Mechanisms of bleomycin-induced lung damage. Arch Toxicol 65: 81-94.
34. Snider GL, Hayes JA, Korthy AL (1978) Chronic interstitial pulmonary fibrosis produced in hamsters by endotracheal bleomycin: pathology and stereology. Am Rev Respir Dis 117: 1099-1108.
35. Thrall RS, McCormick JR, Jack RM, McReynolds RA, Ward PA (1979) Bleomycin-induced pulmonary fibrosis in the rat: inhibition by indomethacin. Am J Pathol 95: 117-130.
36. Degryse AL, Tanjore H, Xu XC, Polosukhin VV, Jones BR, et al. (2010) Repetitive intratracheal bleomycin models several features of idiopathic pulmonary fibrosis. Am J Physiol Lung Cell Mol Physiol 299: L442-452.
37. Adachi K, Mizoguchi K, Kawarada S, Miyoshi A, Suzuki M, et al. (2010) Effects of erlotinib on lung injury induced by intratracheal administration of bleomycin (BLM) in rats. J Toxicol Sci 35: 503-514.
38. Gong LK, Li XH, Wang H, Zhang L, Cai Y, et al. (2004) Feitai attenuates bleomycin-induced pulmonary fibrosis in rats. Biol Pharm Bull 27: 634-640.
39. Moore BB, Hogaboam CM (2008) Murine models of pulmonary fibrosis. Am J Physiol Lung Cell Mol Physiol 294: L152-160.
40. Matsuo K, Maeda Y, Naiki Y, Matsuoka T, Tamai Y, et al. (2005) Possible effects of hepatocyte growth factor for the prevention of peritoneal fibrosis. Nephron Exp Nephrol 99: e87-94.
41. Matsuoka T, Maeda Y, Matsuo K, Naiki Y, Tamai Y, et al. (2008) Hepatocyte growth factor prevents peritoneal fibrosis in an animal model of encapsulating peritoneal sclerosis. J Nephrol 21: 64-73.
42. Yu L, Border WA, Anderson I, McCourt M, Huang Y, et al. (2004) Combining TGF-beta inhibition and angiotensin II blockade results in enhanced antifibrotic effect. Kidney Int 66: 1774-1784.

43. Yu MA, Shin KS, Kim JH, Kim YI, Chung SS, et al. (2009) HGF and BMP-7 ameliorate high glucose-induced epithelial-to-mesenchymal transition of peritoneal mesothelium. J Am Soc Nephrol 20: 567-581.
44. Zeisberg M, Bottiglio C, Kumar N, Maeshima Y, Strutz F, et al. (2003) Bone morphogenic protein-7 inhibits progression of chronic renal fibrosis associated with two genetic mouse models. Am J Physiol Renal Physiol 285: F1060-1067.
45. Cao Q, Wang Y, Zheng D, Sun Y, Lee VW, et al. (2010) IL-10/TGF-beta-modified macrophages induce regulatory T cells and protect against adriamycin nephrosis. J Am Soc Nephrol 21: 933-942.
46. Jeansson M, Bjorck K, Tenstad O, Haraldsson B (2009) Adriamycin alters glomerular endothelium to induce proteinuria. J Am Soc Nephrol 20: 114-122.
47. Lee VW, Harris DC (2011) Adriamycin nephropathy: a model of focal segmental glomerulosclerosis. Nephrology (Carlton) 16: 30-38.
48. Kramer AB, van Timmeren MM, Schuurs TA, Vaidya VS, Bonventre JV, et al. (2009) Reduction of proteinuria in adriamycin-induced nephropathy is associated with reduction of renal kidney injury molecule (Kim-1) over time. Am J Physiol Renal Physiol 296: F1136-1145.
49. Zhou TB, Qin YH, Lei FY, Su LN, Zhao YJ, et al. (2011) apoE expression in glomerulus and correlation with glomerulosclerosis induced by adriamycin in rats. Ren Fail 33: 348-354.
50. Kveder M, Zupancic I, Lahajnar G, Blinc R, Suput D, et al. (1988) Water proton NMR relaxation mechanisms in lung tissue. Magn Reson Med 7: 432-441.
51. Bergin CJ, Pauly JM, Macovski A (1991) Lung parenchyma: projection reconstruction MR imaging. Radiology 179: 777-781.
52. Gewalt SL, Glover GH, Hedlund LW, Cofer GP, MacFall JR, et al. (1993) MR microscopy of the rat lung using projection reconstruction. Magn Reson Med 29: 99-106.
53. Glover GH, Noll DC (1993) Consistent projection reconstruction (CPR) techniques for MRI. Magn Reson Med 29: 345-351.
54. Glover GH, Pauly JM (1992) Projection reconstruction techniques for reduction of motion effects in MRI. Magn Reson Med 28: 275-289.
55. Tornell J, Snaith M (2002) Transgenic systems in drug discovery: from target identification to humanized mice. Drug Discov Today 7: 461-470.
56. Zambrowicz BP, Sands AT (2003) Knockouts model the 100 best-selling drugs--will they model the next 100? Nat Rev Drug Discov 2: 38-51.
57. Beckmann N (2006) In Vivo MR Techniques in Drug Discovery and Development; Beckmann N, editor: Taylor & Francis, New York.
58. Beckmann N, Kneuer R, Gremlich HU, Karmouty-Quintana H, Ble FX, et al. (2007) In vivo mouse imaging and spectroscopy in drug discovery. NMR Biomed 20: 154-185.
59. Reid DG (2006) "MRI in Pharmaceutical Safety Assessment" In: In Vivo MR Techniques in Drug Discovery and Development; Beckmann N, editor: Taylor & Francis, New York.
60. Russell WMS, Burch R.L. (1959) The Principles of Humane Experimental Technique: Methuen, London.
61. Rudin M, Weissleder R (2003) Molecular imaging in drug discovery and development. Nat Rev Drug Discov 2: 123-131.
62. Frank R, Hargreaves R (2003) Clinical biomarkers in drug discovery and development. Nat Rev Drug Discov 2: 566-580.
63. Pien HH, Fischman AJ, Thrall JH, Sorensen AG (2005) Using imaging biomarkers to accelerate drug development and clinical trials. Drug Discov Today 10: 259-266.
64. Southam DS, Dolovich M, O'Byrne PM, Inman MD (2002) Distribution of intranasal instillations in mice: effects of volume, time, body position, and anesthesia. Am J Physiol Lung Cell Mol Physiol 282: L833-839.
65. Foster WM, Walters DM, Longphre M, Macri K, Miller LM (2001) Methodology for the measurement of mucociliary function in the mouse by scintigraphy. J Appl Physiol 90: 1111-1117.

66. Rao GV, Tinkle S, Weissman DN, Antonini JM, Kashon ML, et al. (2003) Efficacy of a technique for exposing the mouse lung to particles aspirated from the pharynx. J Toxicol Environ Health A 66: 1441-1452.
67. Lakatos HF, Burgess HA, Thatcher TH, Redonnet MR, Hernady E, et al. (2006) Oropharyngeal aspiration of a silica suspension produces a superior model of silicosis in the mouse when compared to intratracheal instillation. Exp Lung Res 32: 181-199.
68. De Vooght V, Vanoirbeek JA, Haenen S, Verbeken E, Nemery B, et al. (2009) Oropharyngeal aspiration: an alternative route for challenging in a mouse model of chemical-induced asthma. Toxicology 259: 84-89.
69. Morgan DL, Flake GP, Kirby PJ, Palmer SM (2008) Respiratory toxicity of diacetyl in C57BL/6 mice. Toxicol Sci 103: 169-180.
70. Babin AL, Cannet C, Gerard C, Saint-Mezard P, Page CP, et al. (2012) Bleomycin-induced lung injury in mice investigated by MRI: model assessment for target analysis. Magn Reson Med 67: 499-509.
71. Bosanquet AG (1986) Stability of solutions of antineoplastic agents during preparation and storage for in vitro assays. II. Assay methods, adriamycin and the other antitumour antibiotics. Cancer Chemother Pharmacol 17: 1-10.
72. Ble FX, Cannet C, Zurbruegg S, Karmouty-Quintana H, Bergmann R, et al. (2008) Allergen-induced lung inflammation in actively sensitized mice assessed with MR imaging. Radiology 248: 834-843.
73. Takahashi M, Togao O, Obara M, van Cauteren M, Ohno Y, et al. (2010) Ultra-short echo time (UTE) MR imaging of the lung: comparison between normal and emphysematous lungs in mutant mice. J Magn Reson Imaging 32: 326-333.
74. van Echteld CJ, Beckmann N (2011) A view on imaging in drug research and development for respiratory diseases. J Pharmacol Exp Ther 337: 335-349.
75. Zurek M, Boyer L, Caramelle P, Boczkowski J, Cremillieux Y (2011) Longitudinal and noninvasive assessment of emphysema evolution in a murine model using proton MRI. Magn Reson Med.
76. Andrade GB, Riet-Correa F, Montes GS, Battlehner CN, Saldiva PH (1997) Dating of fibrotic lesions by the Picrosirius-polarization method. An application using the lesions of Lechiguana (bovine focal proliferative fibrogranulomatous panniculitis). Eur J Histochem 41: 203-209.
77. Bradshaw AD, Baicu CF, Rentz TJ, Van Laer AO, Boggs J, et al. (2009) Pressure overload-induced alterations in fibrillar collagen content and myocardial diastolic function: role of secreted protein acidic and rich in cysteine (SPARC) in post-synthetic procollagen processing. Circulation 119: 269-280.
78. Bradshaw AD, Baicu CF, Rentz TJ, Van Laer AO, Bonnema DD, et al. (2010) Age-dependent alterations in fibrillar collagen content and myocardial diastolic function: role of SPARC in post-synthetic procollagen processing. Am J Physiol Heart Circ Physiol 298: H614-622.
79. Montes GS, Junqueira LC (1991) The use of the Picrosirius-polarization method for the study of the biopathology of collagen. Mem Inst Oswaldo Cruz 86 Suppl 3: 1-11.
80. Pickering JG, Boughner DR (1991) Quantitative assessment of the age of fibrotic lesions using polarized light microscopy and digital image analysis. Am J Pathol 138: 1225-1231.
81. Whittaker P, Kloner RA, Boughner DR, Pickering JG (1994) Quantitative assessment of myocardial collagen with picrosirius red staining and circularly polarized light. Basic Res Cardiol 89: 397-410.
82. Zhang H, Sun L, Wang W, Ma X (2006) Quantitative analysis of fibrosis formation on the microcapsule surface with the use of picro-sirius red staining, polarized light microscopy, and digital image analysis. J Biomed Mater Res A 76: 120-125.
83. Diaz Encarnacion MM, Griffin MD, Slezak JM, Bergstralh EJ, Stegall MD, et al. (2004) Correlation of quantitative digital image analysis with the glomerular filtration rate in chronic allograft nephropathy. Am J Transplant 4: 248-256.

84. Farris AB, Adams CD, Brousaides N, Della Pelle PA, Collins AB, et al. (2011) Morphometric and visual evaluation of fibrosis in renal biopsies. J Am Soc Nephrol 22: 176-186.
85. Galli GG, Honnens de Lichtenberg K, Carrara M, Hans W, Wuelling M, et al. (2012) Prdm5 regulates collagen gene transcription by association with RNA polymerase II in developing bone. PLoS Genet 8: e1002711.
86. Gold LI, Rahman M, Blechman KM, Greives MR, Churgin S, et al. (2006) Overview of the role for calreticulin in the enhancement of wound healing through multiple biological effects. J Investig Dermatol Symp Proc 11: 57-65.
87. Moon JC, Reed E, Sheppard MN, Elkington AG, Ho SY, et al. (2004) The histologic basis of late gadolinium enhancement cardiovascular magnetic resonance in hypertrophic cardiomyopathy. J Am Coll Cardiol 43: 2260-2264.
88. Nart P, Williams A, Thompson H, Innocent GT (2004) Morphometry of bovine dilated cardiomyopathy. J Comp Pathol 130: 235-245.
89. Ophof R, Maltha JC, Von den Hoff JW, Kuijpers-Jagtman AM (2004) Histologic evaluation of skin-derived and collagen-based substrates implanted in palatal wounds. Wound Repair Regen 12: 528-538.
90. Rossi GA, Szapiel S, Ferrans VJ, Crystal RG (1987) Susceptibility to experimental interstitial lung disease is modified by immune- and non-immune-related genes. Am Rev Respir Dis 135: 448-455.
91. Schrier DJ, Kunkel RG, Phan SH (1983) The role of strain variation in murine bleomycin-induced pulmonary fibrosis. Am Rev Respir Dis 127: 63-66.
92. Shapiro SD, Griffin GL, Gilbert DJ, Jenkins NA, Copeland NG, et al. (1992) Molecular cloning, chromosomal localization, and bacterial expression of a murine macrophage metalloelastase. J Biol Chem 267: 4664-4671.
93. Shapiro SD, Kobayashi DK, Ley TJ (1993) Cloning and characterization of a unique elastolytic metalloproteinase produced by human alveolar macrophages. J Biol Chem 268: 23824-23829.
94. Morris L, Graham CF, Gordon S (1991) Macrophages in haemopoietic and other tissues of the developing mouse detected by the monoclonal antibody F4/80. Development 112: 517-526.
95. Austyn JM, Gordon S (1981) F4/80, a monoclonal antibody directed specifically against the mouse macrophage. Eur J Immunol 11: 805-815.
96. England KA, Price AP, Tram KV, Shapiro SD, Blazar BR, et al. (2011) Evidence for early fibrosis and increased airway resistance in bone marrow transplant recipient mice deficient in MMP12. Am J Physiol Lung Cell Mol Physiol 301: L519-526.
97. Chua F, Gauldie J, Laurent GJ (2005) Pulmonary fibrosis: searching for model answers. Am J Respir Cell Mol Biol 33: 9-13.
98. Corbel M, Caulet-Maugendre S, Germain N, Molet S, Lagente V, et al. (2001) Inhibition of bleomycin-induced pulmonary fibrosis in mice by the matrix metalloproteinase inhibitor batimastat. J Pathol 193: 538-545.
99. Takemasa A, Ishii Y, Fukuda T (2012) A neutrophil elastase inhibitor prevents bleomycin-induced pulmonary fibrosis in mice. Eur Respir J.
100. Iwasawa T, Ogura T, Sakai F, Kanauchi T, Komagata T, et al. (2012) CT analysis of the effect of pirfenidone in patients with idiopathic pulmonary fibrosis. Eur J Radiol.
101. Cheng G, Swaidani S, Sharma M, Lauer ME, Hascall VC, et al. (2011) Hyaluronan deposition and correlation with inflammation in a murine ovalbumin model of asthma. Matrix Biol 30: 126-134.
102. Wang F, Garza LA, Kang S, Varani J, Orringer JS, et al. (2007) In vivo stimulation of de novo collagen production caused by cross-linked hyaluronic acid dermal filler injections in photodamaged human skin. Arch Dermatol 143: 155-163.
103. Turlier V, Delalleau A, Casas C, Rouquier A, Bianchi P, et al. (2013) Association between collagen production and mechanical stretching in dermal extracellular matrix: in vivo effect of cross-

linked hyaluronic acid filler. A randomised, placebo-controlled study. J Dermatol Sci 69: 187-194.
104. Josse G, Haftek M, Gensanne D, Turlier V, Mas A, et al. (2010) Follow up study of dermal hyaluronic acid injection by high frequency ultrasound and magnetic resonance imaging. J Dermatol Sci 57: 214-216.
105. Juliano RL, Haskill S (1993) Signal transduction from the extracellular matrix. J Cell Biol 120: 577-585.
106. Shapiro SD, Kobayashi DK, Pentland AP, Welgus HG (1993) Induction of macrophage metalloproteinases by extracellular matrix. Evidence for enzyme- and substrate-specific responses involving prostaglandin-dependent mechanisms. J Biol Chem 268: 8170-8175.
107. McKee CM, Penno MB, Cowman M, Burdick MD, Strieter RM, et al. (1996) Hyaluronan (HA) fragments induce chemokine gene expression in alveolar macrophages. The role of HA size and CD44. J Clin Invest 98: 2403-2413.
108. Horton MR, Shapiro S, Bao C, Lowenstein CJ, Noble PW (1999) Induction and regulation of macrophage metalloelastase by hyaluronan fragments in mouse macrophages. J Immunol 162: 4171-4176.
109. Bjermer L, Lundgren R, Hallgren R (1989) Hyaluronan and type III procollagen peptide concentrations in bronchoalveolar lavage fluid in idiopathic pulmonary fibrosis. Thorax 44: 126-131.
110. Venkatesan N, Ouzzine M, Kolb M, Netter P, Ludwig MS (2011) Increased deposition of chondroitin/dermatan sulfate glycosaminoglycan and upregulation of beta1,3-glucuronosyltransferase I in pulmonary fibrosis. Am J Physiol Lung Cell Mol Physiol 300: L191-203.
111. Westergren-Thorsson G, Hernnas J, Sarnstrand B, Oldberg A, Heinegard D, et al. (1993) Altered expression of small proteoglycans, collagen, and transforming growth factor-beta 1 in developing bleomycin-induced pulmonary fibrosis in rats. J Clin Invest 92: 632-637.
112. Nettelbladt O, Scheynius A, Bergh J, Tengblad A, Hallgren R (1991) Alveolar accumulation of hyaluronan and alveolar cellular response in bleomycin-induced alveolitis. Eur Respir J 4: 407-414.
113. Milton PL, Dickinson H, Jenkin G, Lim R (2012) Assessment of respiratory physiology of C57BL/6 mice following bleomycin administration using barometric plethysmography. Respiration 83: 253-266.
114. Blum RH, Carter SK, Agre K (1973) A clinical review of bleomycin--a new antineoplastic agent. Cancer 31: 903-914.
115. Lazo JS, Sebti SM, Schellens JH (1996) Bleomycin. Cancer Chemother Biol Response Modif 16: 39-47.
116. Ngeow J, Tan IB, Kanesvaran R, Tan HC, Tao M, et al. (2011) Prognostic impact of bleomycin-induced pneumonitis on the outcome of Hodgkin's lymphoma. Ann Hematol 90: 67-72.
117. Sleijfer S (2001) Bleomycin-induced pneumonitis. Chest 120: 617-624.
118. Mouratis MA, Aidinis V (2011) Modeling pulmonary fibrosis with bleomycin. Curr Opin Pulm Med 17: 355-361.
119. Scotton CJ, Chambers RC (2010) Bleomycin revisited: towards a more representative model of IPF? Am J Physiol Lung Cell Mol Physiol 299: L439-441.
120. Egger C, Cannet C, Gerard C, Jarman E, Jarai G, et al. (2013) Administration of Bleomycin via the Oropharyngeal Aspiration Route Leads to Sustained Lung Fibrosis in Mice and Rats as Quantified by UTE-MRI and Histology. PLoS One 8: e63432.
121. Karmouty-Quintana H, Cannet C, Zurbruegg S, Ble FX, Fozard JR, et al. (2007) Bleomycin-induced lung injury assessed noninvasively and in spontaneously breathing rats by proton MRI. J Magn Reson Imaging 26: 941-949.

122. Beckmann N, Tigani B, Ekatodramis D, Borer R, Mazzoni L, et al. (2001) Pulmonary edema induced by allergen challenge in the rat: noninvasive assessment by magnetic resonance imaging. Magn Reson Med 45: 88-95.
123. Mirfazaelian A, Fisher JW (2007) Organ growth functions in maturing male Sprague-Dawley rats based on a collective database. J Toxicol Environ Health A 70: 1052-1063.
124. Jacob RE, Amidan BG, Soelberg J, Minard KR (2010) In vivo MRI of altered proton signal intensity and T2 relaxation in a bleomycin model of pulmonary inflammation and fibrosis. J Magn Reson Imaging 31: 1091-1099.
125. Quintana HK, Cannet C, Zurbruegg S, Ble FX, Fozard JR, et al. (2006) Proton MRI as a noninvasive tool to assess elastase-induced lung damage in spontaneously breathing rats. Magn Reson Med 56: 1242-1250.
126. Lasky JA, Ortiz LA (2001) Antifibrotic therapy for the treatment of pulmonary fibrosis. Am J Med Sci 322: 213-221.
127. Cunningham CC (2007) Talabostat. Expert Opin Investig Drugs 16: 1459-1465.
128. Sood BG, Dawe EJ, Maddipati KR, Malian M, Chen X, et al. (2008) Toxicity of prolonged high dose inhaled PGE1 in ventilated neonatal pigs. Pulm Pharmacol Ther 21: 565-572.
129. Beckmann N, Tigani B, Mazzoni L, Fozard JR (2001) MRI of lung parenchyma in rats and mice using a gradient-echo sequence. NMR Biomed 14: 297-306.
130. Madala SK, Pesce JT, Ramalingam TR, Wilson MS, Minnicozzi S, et al. (2010) Matrix metalloproteinase 12-deficiency augments extracellular matrix degrading metalloproteinases and attenuates IL-13-dependent fibrosis. J Immunol 184: 3955-3963.
131. Swiderski RE, Dencoff JE, Floerchinger CS, Shapiro SD, Hunninghake GW (1998) Differential expression of extracellular matrix remodeling genes in a murine model of bleomycin-induced pulmonary fibrosis. Am J Pathol 152: 821-828.
132. Wu L, Fan J, Matsumoto S, Watanabe T (2000) Induction and regulation of matrix metalloproteinase-12 by cytokines and CD40 signaling in monocyte/macrophages. Biochem Biophys Res Commun 269: 808-815.
133. Moeller A, Ask K, Warburton D, Gauldie J, Kolb M (2008) The bleomycin animal model: a useful tool to investigate treatment options for idiopathic pulmonary fibrosis? Int J Biochem Cell Biol 40: 362-382.
134. Ask K, Labiris R, Farkas L, Moeller A, Froese A, et al. (2008) Comparison between conventional and "clinical" assessment of experimental lung fibrosis. J Transl Med 6: 16.
135. Lebtahi R, Moreau S, Marchand-Adam S, Debray MP, Brauner M, et al. (2006) Increased uptake of 111In-octreotide in idiopathic pulmonary fibrosis. J Nucl Med 47: 1281-1287.
136. Borie R, Fabre A, Prost F, Marchal-Somme J, Lebtahi R, et al. (2008) Activation of somatostatin receptors attenuates pulmonary fibrosis. Thorax 63: 251-258.
137. Lahlou H, Saint-Laurent N, Esteve JP, Eychene A, Pradayrol L, et al. (2003) sst2 Somatostatin receptor inhibits cell proliferation through Ras-, Rap1-, and B-Raf-dependent ERK2 activation. J Biol Chem 278: 39356-39371.
138. Pippin JW, Brinkkoetter PT, Cormack-Aboud FC, Durvasula RV, Hauser PV, et al. (2009) Inducible rodent models of acquired podocyte diseases. Am J Physiol Renal Physiol 296: F213-229.
139. Baumann D, Rudin M (2000) Quantitative assessment of rat kidney function by measuring the clearance of the contrast agent Gd(DOTA) using dynamic MRI. Magn Reson Imaging 18: 587-595.
140. Laurent D, Poirier K, Wasvary J, Rudin M (2002) Effect of essential hypertension on kidney function as measured in rat by dynamic MRI. Magn Reson Med 47: 127-134.
141. Raynal I, Prigent P, Peyramaure S, Najid A, Rebuzzi C, et al. (2004) Macrophage endocytosis of superparamagnetic iron oxide nanoparticles: mechanisms and comparison of ferumoxides and ferumoxtran-10. Invest Radiol 39: 56-63.
142. von Zur Muhlen C, von Elverfeldt D, Bassler N, Neudorfer I, Steitz B, et al. (2007) Superparamagnetic iron oxide binding and uptake as imaged by magnetic resonance is

mediated by the integrin receptor Mac-1 (CD11b/CD18): implications on imaging of atherosclerotic plaques. Atherosclerosis 193: 102-111.
143. Beckmann N, Cannet C, Babin AL, Ble FX, Zurbruegg S, et al. (2009) In vivo visualization of macrophage infiltration and activity in inflammation using magnetic resonance imaging. Wiley Interdiscip Rev Nanomed Nanobiotechnol 1: 272-298.
144. Stoll G, Bendszus M (2010) New approaches to neuroimaging of central nervous system inflammation. Curr Opin Neurol 23: 282-286.
145. El Chaar M, Chen J, Seshan SV, Jha S, Richardson I, et al. (2007) Effect of combination therapy with enalapril and the TGF-beta antagonist 1D11 in unilateral ureteral obstruction. Am J Physiol Renal Physiol 292: F1291-1301.
146. Wu CF, Chiang WC, Lai CF, Chang FC, Chen YT, et al. (2013) Transforming growth factor beta-1 stimulates profibrotic epithelial signaling to activate pericyte-myofibroblast transition in obstructive kidney fibrosis. Am J Pathol 182: 118-131.
147. Allard M, Doucet D, Kien P, Bonnemain B, Caille JM (1988) Experimental study of DOTA-gadolinium. Pharmacokinetics and pharmacologic properties. Invest Radiol 23 Suppl 1: S271-274.
148. Katzberg RW, Sahler LG, Duda SW, Morris TW, McKenna BA, et al. (1990) Renal handling and physiologic effects of the paramagnetic contrast medium Gd-DOTA. Invest Radiol 25: 714-719.
149. Rohrschneider WK, Haufe S, Clorius JH, Troger J (2003) MR to assess renal function in children. Eur Radiol 13: 1033-1045.
150. Sari-Sarraf F, Pomposiello S, Laurent D (2008) Acute impairment of rat renal function by L -NAME as measured using dynamic MRI. MAGMA 21: 291-297.
151. Rosen BR, Belliveau JW, Vevea JM, Brady TJ (1990) Perfusion imaging with NMR contrast agents. Magn Reson Med 14: 249-265.
152. Beckmann N, Cannet C, Fringeli-Tanner M, Baumann D, Pally C, et al. (2003) Macrophage labeling by SPIO as an early marker of allograft chronic rejection in a rat model of kidney transplantation. Magn Reson Med 49: 459-467.
153. Beckmann N, Cannet C, Zurbruegg S, Haberthur R, Li J, et al. (2006) Macrophage infiltration detected at MR imaging in rat kidney allografts: early marker of chronic rejection? Radiology 240: 717-724.
154. Smit-van Oosten A, Navis G, Stegeman CA, Joles JA, Klok PA, et al. (2001) Chronic blockade of angiotensin II action prevents glomerulosclerosis, but induces graft vasculopathy in experimental kidney transplantation. J Pathol 194: 122-129.
155. Racusen LC, Solez K, Colvin RB, Bonsib SM, Castro MC, et al. (1999) The Banff 97 working classification of renal allograft pathology. Kidney Int 55: 713-723.
156. Bertani T, Poggi A, Pozzoni R, Delaini F, Sacchi G, et al. (1982) Adriamycin-induced nephrotic syndrome in rats: sequence of pathologic events. Lab Invest 46: 16-23.
157. Sakemi T, Ohtsuka N, Tomiyoshi Y, Morito F (1996) Sex difference in progression of adriamycin-induced nephropathy in rats. Am J Nephrol 16: 540-547.
158. Nakatsue T, Koike H, Han GD, Suzuki K, Miyauchi N, et al. (2005) Nephrin and podocin dissociate at the onset of proteinuria in experimental membranous nephropathy. Kidney Int 67: 2239-2253.
159. Javaid B, Olson JL, Meyer TW (2001) Glomerular injury and tubular loss in adriamycin nephrosis. J Am Soc Nephrol 12: 1391-1400.
160. Boonsanit D, Kanchanapangka S, Buranakarl C (2006) L-carnitine ameliorates doxorubicin-induced nephrotic syndrome in rats. Nephrology (Carlton) 11: 313-320.
161. Ochodnicky P, Henning RH, Buikema H, Kluppel AC, van Wattum M, et al. (2009) Renal endothelial function and blood flow predict the individual susceptibility to adriamycin-induced renal damage. Nephrol Dial Transplant 24: 413-420.
162. Bohle A, Wehrmann M, Mackensen-Haen S, Gise H, Mickeler E, et al. (1994) Pathogenesis of chronic renal failure in primary glomerulopathies. Nephrol Dial Transplant 9 Suppl 3: 4-12.

163. Kim YG, Suga SI, Kang DH, Jefferson JA, Mazzali M, et al. (2000) Vascular endothelial growth factor accelerates renal recovery in experimental thrombotic microangiopathy. Kidney Int 58: 2390-2399.
164. Kang DH, Joly AH, Oh SW, Hugo C, Kerjaschki D, et al. (2001) Impaired angiogenesis in the remnant kidney model: I. Potential role of vascular endothelial growth factor and thrombospondin-1. J Am Soc Nephrol 12: 1434-1447.
165. Kairaitis LK, Wang Y, Gassmann M, Tay YC, Harris DC (2005) HIF-1alpha expression follows microvascular loss in advanced murine adriamycin nephrosis. Am J Physiol Renal Physiol 288: F198-206.
166. Ong AC, Fine LG (1994) Tubular-derived growth factors and cytokines in the pathogenesis of tubulointerstitial fibrosis: implications for human renal disease progression. Am J Kidney Dis 23: 205-209.
167. Zoja C, Morigi M, Figliuzzi M, Bruzzi I, Oldroyd S, et al. (1995) Proximal tubular cell synthesis and secretion of endothelin-1 on challenge with albumin and other proteins. Am J Kidney Dis 26: 934-941.
168. Vasquez-Vivar J, Martasek P, Hogg N, Masters BS, Pritchard KA, Jr., et al. (1997) Endothelial nitric oxide synthase-dependent superoxide generation from adriamycin. Biochemistry 36: 11293-11297.
169. Murata T, Yamawaki H, Yoshimoto R, Hori M, Sato K, et al. (2001) Chronic effect of doxorubicin on vascular endothelium assessed by organ culture study. Life Sci 69: 2685-2695.
170. Luscher TF (1993) 1993 Mack Forster Award Lecture. Review. The endothelium as a target and mediator of cardiovascular disease. Eur J Clin Invest 23: 670-685.
171. Wang Y, Wang YP, Zheng G, Lee VW, Ouyang L, et al. (2007) Ex vivo programmed macrophages ameliorate experimental chronic inflammatory renal disease. Kidney Int 72: 290-299.
172. Munoz M, Rincon J, Pedreanez A, Viera N, Hernandez-Fonseca JP, et al. (2011) Proinflammatory role of angiotensin II in a rat nephrosis model induced by adriamycin. J Renin Angiotensin Aldosterone Syst 12: 404-412.
173. Benigni A, Zoja C, Campana M, Corna D, Sangalli F, et al. (2006) Beneficial effect of TGFbeta antagonism in treating diabetic nephropathy depends on when treatment is started. Nephron Exp Nephrol 104: e158-168.
174. Mahajan D, Wang Y, Qin X, Zheng G, Wang YM, et al. (2006) CD4+CD25+ regulatory T cells protect against injury in an innate murine model of chronic kidney disease. J Am Soc Nephrol 17: 2731-2741.
175. Nikolic-Paterson DJ, Lan HY, Hill PA, Atkins RC (1994) Macrophages in renal injury. Kidney Int Suppl 45: S79-82.
176. Pawluczyk IZ, Harris KP (1997) Macrophages promote prosclerotic responses in cultured rat mesangial cells: a mechanism for the initiation of glomerulosclerosis. J Am Soc Nephrol 8: 1525-1536.
177. Xu H, Kurihara H, Ito T, Kikuchi H, Yoshida K, et al. (2005) The keratan sulfate disaccharide Gal(6S03) beta1,4-GlcNAc(6S03) modulates interleukin 12 production by macrophages in murine Thy-1 type autoimmune disease. J Biol Chem 280: 20879-20886.
178. Nakamura K, Kitani A, Strober W (2001) Cell contact-dependent immunosuppression by CD4(+)CD25(+) regulatory T cells is mediated by cell surface-bound transforming growth factor beta. J Exp Med 194: 629-644.
179. Samon JB, Champhekar A, Minter LM, Telfer JC, Miele L, et al. (2008) Notch1 and TGFbeta1 cooperatively regulate Foxp3 expression and the maintenance of peripheral regulatory T cells. Blood 112: 1813-1821.
180. Hue S, Kared H, Mehwish Y, Mouhamad S, Balbo M, et al. (2012) Notch activation on effector T cells increases their sensitivity to Treg cell-mediated suppression through upregulation of TGF-betaRII expression. Eur J Immunol 42: 1796-1803.

181. Mesnard L, Keller AC, Michel ML, Vandermeersch S, Rafat C, et al. (2009) Invariant natural killer T cells and TGF-beta attenuate anti-GBM glomerulonephritis. J Am Soc Nephrol 20: 1282-1292.
182. Murphy SR, Dahly-Vernon AJ, Dunn KM, Chen CC, Ledbetter SR, et al. (2012) Renoprotective effects of anti-TGF-beta antibody and antihypertensive therapies in Dahl S rats. Am J Physiol Regul Integr Comp Physiol 303: R57-69.
183. Rangan GK, Wang Y, Harris DC (2001) Pharmacologic modulators of nitric oxide exacerbate tubulointerstitial inflammation in proteinuric rats. J Am Soc Nephrol 12: 1696-1705.
184. Abo-Salem OM (2012) The protective effect of aminoguanidine on doxorubicin-induced nephropathy in rats. J Biochem Mol Toxicol 26: 1-9.
185. Bi BT, Yang YB, Ma AD, Lin T, Lin HB, et al. (2012) The effect of candesartan on the pharmacokinetics of enalaprilat in nephrotic rats. Eur Rev Med Pharmacol Sci 16: 2162-2170.
186. Schwalm S, Pfeilschifter J, Huwiler A (2013) Sphingosine-1-phosphate: A Janus-faced mediator of fibrotic diseases. Biochim Biophys Acta 1831: 239-250.
187. Idee JM, Port M, Medina C, Lancelot E, Fayoux E, et al. (2008) Possible involvement of gadolinium chelates in the pathophysiology of nephrogenic systemic fibrosis: a critical review. Toxicology 248: 77-88.
188. Rees O, Agarwal SK (2010) Nephrogenic systemic fibrosis: UK survey of the use of gadolinium-based contrast media. Clin Radiol 65: 636-641.
189. Idee JM, Port M, Robic C, Medina C, Sabatou M, et al. (2009) Role of thermodynamic and kinetic parameters in gadolinium chelate stability. J Magn Reson Imaging 30: 1249-1258.
190. Vivier PH, Blondiaux E, Dolores M, Marouteau-Pasquier N, Brasseur M, et al. (2009) [Functional MR urography in children]. J Radiol 90: 11-19.
191. Stacul F, van der Molen AJ, Reimer P, Webb JA, Thomsen HS, et al. (2011) Contrast induced nephropathy: updated ESUR Contrast Media Safety Committee guidelines. Eur Radiol 21: 2527-2541.
192. Thomsen HS, Morcos SK, Almen T, Bellin MF, Bertolotto M, et al. (2013) Nephrogenic systemic fibrosis and gadolinium-based contrast media: updated ESUR Contrast Medium Safety Committee guidelines. Eur Radiol 23: 307-318.

9) List of Publications

Published:

- Egger C, Cannet C, Gérard C, Jarman E, Jarai G, Feige A, Suply T, Dunbar A, Tigani B, Beckmann N (2013) Administration of Bleomycin via the Oropharyngeal Aspiration Route Leads to Sustained Pulmonary Fibrosis in Mice and Rats. PLOS One.

- Egger C, Cannet C, Gérard C, Debon C, Stohler N, Dunbar A, Tigani B, Li J, Beckmann N (2014); Adriamycin-Induced Nephropathy in Rats: Functional and Cellular Effects Characterized by MRI.

- Egger C, Cannet C, Gérard C, Dunbar A, Tigani B, Beckmann N (2014); Hyaluronidase modulates bleomycin-induced lung injury detected noninvasively in small rodents by radial proton MRI.

- Egger C, Gérard C, Vidotto N, Accart N, Cannet C, Dunbar A, Tigani B, Piaia A, Jarai G, Jarman E, Schmid HA, Beckmann N (2014); Lung volume quantified by MRI reflects extracellular-matrix deposition and altered pulmonary function in bleomycin models of fibrosis: effects of SOM230.

Drafts:

- Egger C, Cannet C, Gérard C, Ksiazek I, Feige A, Suply T, Dunbar A, Tigani B, Beckmann N (2013); “Therapeutic Effects of the Fibroblast Activation Protein Inhibitor, PT100, in a Murine Model of Pulmonary Fibrosis”

10) Acknowledgement

I got the possibility to perform the practical work for my thesis between 2010 and 2013 in the laboratories of my supervisor Dr. Nicolau Beckmann in Novartis institute of biomedical research. Sincere thanks are given to him and Stefan Zurbrügg, who introduced me to the world of industrial pharmaceutical research, teached me in practical work and scientific thinking, answered all my questions with patience, and gave a lot of input to my thesis.

Further thanks go to faculty representative Prof. Dr. Joachim Seelig and his group for supporting me during my PhD studies, to the co-referee Prof. Dr. Markus von Kienlin for reading and evaluating this thesis, and to Prof Dr. Anna Seelig-Löffler and her group.

Regarding practical work, thank goes to Catherine Cannet and Christelle Gerard for the support with histological analysis, to Bruno Tigani and Andrew Dunbar (hydroxyproline assay), to Bobby Gremlich and Alexandra Suter (NIRF), to Herbert Schmid and Ramona Rebmann (SOM230), Elizabeth Jarman and Gabor Jarai (oropharyngeal aspiration of bleomycin), as well as to the laboratories of Thomas Supply and Angelika Meyer for teaching me in RT-PCR.

In the end my sincere thank goes to my sister Barbara, my mother Renate, my father Fredi, and dear friends for their love and support during the time of my PhD studies.